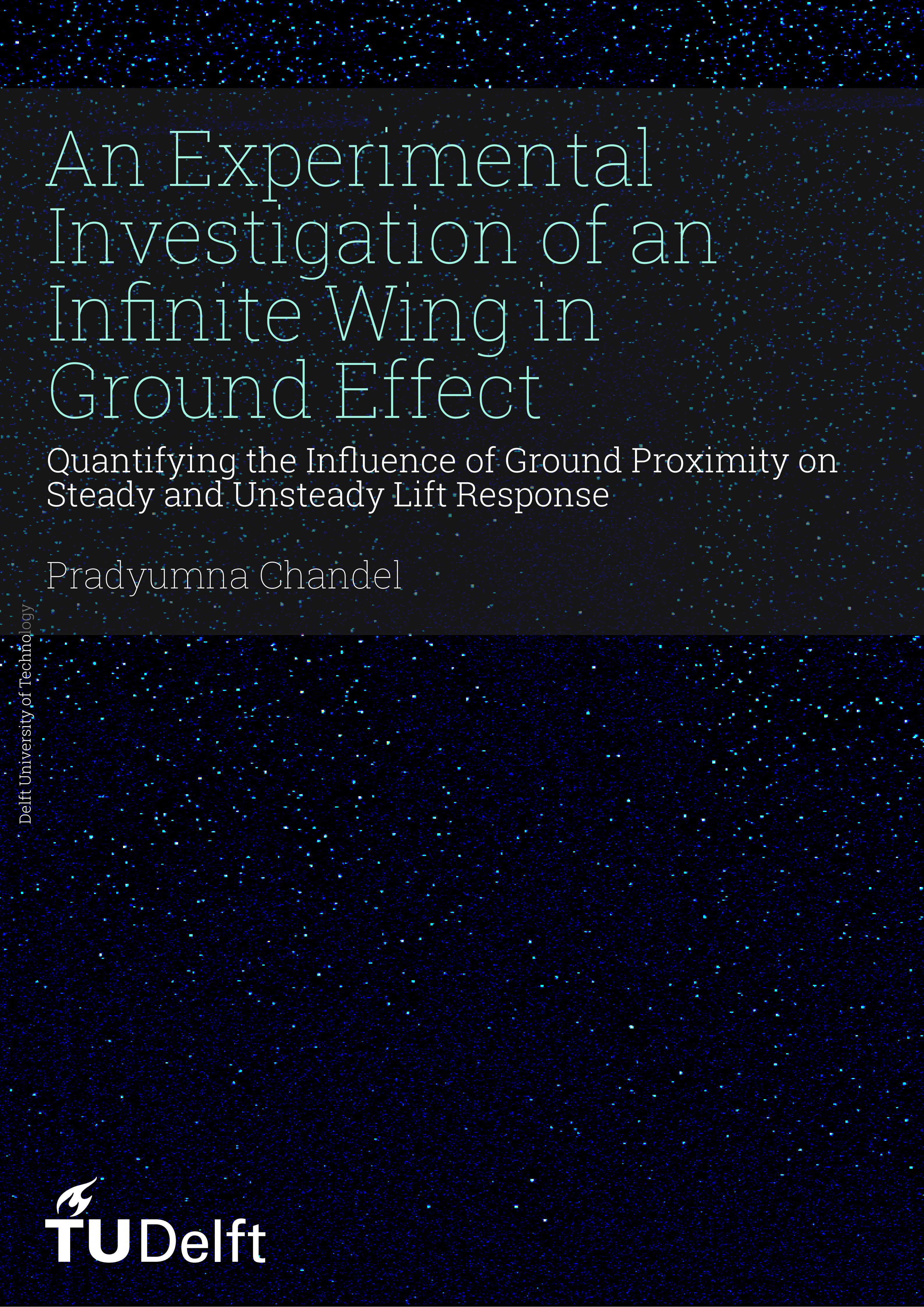

An Experimental Investigation of an Infinite Wing in Ground Effect

Quantifying the Influence of Ground Proximity on Steady and Unsteady Lift Response

Pradyumna Chandel

Delft University of Technology

An Experimental Investigation of an Infinite Wing in Ground Effect

Quantifying the Influence of Ground Proximity on Steady and Unsteady Lift Response

by

Pradyumna Chandel

Student Name	Student Number
Pradyumna Chandel	5780446

Supervisors:	Dr. A. Daliri & Dr. F. Scarano
Project Duration:	March, 2025 - April, 2026
Faculty:	Faculty of Aerospace Engineering, Delft

Cover: Wing in ground with Helium-filled soap bubbles by Pradyumna Chandel
Style: TU Delft Report Style

आचार्यात् पादं आदत्ते पादं शिष्यः स्वमेधया ।
पादं सब्रह्मचारिभिः पादं कालक्रमेण च ॥

--- चाणक्यः, चतुर्थी शताब्दी पूर्वकालीन

A student receives a quarter of knowledge from the teacher,
a quarter from their own intellect,
a quarter from fellow students,
and a quarter through experience over time.

— Chanakya, 4th century BCE

Preface

My fascination with flight began long before this project; some of my earliest memories involve driving past the airport, wondering how such massive machines worked. By the age of five, I was already experimenting with the limits of paper planes, instinctively cutting and folding flaps to see which would stay in the air the longest. This early intuition eventually evolved into a conviction that I was more interested in enabling the act of flying than merely executing it.

The specific spark for this research, however, was ignited on Sunday afternoons watching Formula 1 with my father. What began as a child's plea to change the channel transformed into a deep fascination with the sport's technical complexity. I became enamoured by the myriad of intricate surfaces used to manipulate flow, realizing that every minuscule adjustment to a wing or diffuser contributed to the overall pursuit of lap time. This project bridges those two worlds: the intricate aerodynamics of motor racing and the critical safety boundaries of aviation.

Inspired by the ground-effect phenomena seen in racing, the flutter observed during aircraft take-off and landing, and the renewed global interest in ekranoplans, I set out to quantify how dynamic pitching motions respond in the presence of a rigid boundary.

Over the past nine months, I have been fortunate to receive guidance and encouragement from many individuals. I am deeply grateful to my supervisors, Dr. Abbas Daliri and Prof. Dr. Fulvio Scarano. Prof. Scarano's pioneering work in Particle Image Velocimetry was a primary reason I chose to pursue my studies at TU Delft, and it has been an honour to contribute to the Delft Aerospace Aerodynamics Laboratory under his supervision. Similarly, Dr. Daliri's constant support and technical insights were indispensable in navigating the challenges encountered throughout this project.

I would also like to thank the PhD candidates who supported me during the experimental and processing phase: Vinicius Santos Costa, Luuk Hendriksen, Adrian Grille Guerra, and Ambar Garofano Soldado. My research would not have been possible without the expertise of the lab technicians, Frits Donker Duyvis, Henk-Jan Siemer, Dennis Bruikman and Gert-Jan Benrends who assisted in the manufacturing of the model and provided invaluable advice during the construction of the ground plane and all of my IT troubles.

Above all, I am profoundly grateful to my family for their unflagging moral support, their patience, and the many hours of encouragement they provided throughout this journey. I must also mention my dog, Cherry, who was a constant source of joy and a reliable comfort whenever my spirits needed lifting. Finally, my heartfelt thanks go to my friends in the ”AWE support group” for their camaraderie and for making the more challenging phases of this degree so much more enjoyable.

Pradyumna Chandel
Delft, April 2026

Abstract

The aerodynamic interaction between a lifting surface and a ground plane presents a highly non-linear landscape that is critical to the performance and safety of racing vehicles, wing-in-ground (WIG) craft, and aircraft during take-off and landing. While steady-state wing-ground interaction is well-documented, the coupling of unsteady kinematics with ground proximity remains a frontier in aerodynamics, particularly regarding the evolution of the dynamic stall vortex (DSV). This thesis presents a comprehensive experimental investigation into the steady and unsteady aerodynamics of an infinite NACA0015 airfoil operating in ground effect at a Reynolds number of $Re \approx 2 \times 10^5$. By combining high-frequency surface pressure measurements with phase-resolved $3D$ Particle Tracking Velocimetry ($3D{-}PTV$) using the Shake-the-Box algorithm, the study resolves both surface-level load transients and off-body wake and vorticity dynamics.

The investigation initially establishes a steady-state baseline, revealing that ground influence is non-monotonic. At large clearances ($H > 0.8$), the flow is largely unaffected by the presence of the ground. At moderate clearances ($0.4 < H \leq 0.8$), lift enhancement is driven by the Venturi effect, where geometric confinement accelerates the underbody flow. In extreme ground effect ($H \leq 0.4$), a viscous-confinement domain is observed. In this state, the interaction between the airfoil and ground-plane boundary layers induces a pressure-side blockage that caps circulation growth, a phenomenon that contradicts classical inviscid predictions.

In the unsteady domain, the airfoil was subjected to sinusoidal pitching across a matrix of reduced frequencies ($k = 0.05$ to 0.20) and ground clearances ($H = 0.1$ to ∞). In attached-flow conditions, ground proximity modulates the convective time lag of the wake. At intermediate heights, the accelerated gap flow reduces the time required for circulation to equilibrate, effectively compressing the lift hysteresis loops. At $H = 0.2$, physical blockage and air-column stiffening significantly widen the hysteresis loops, indicating a substantial increase in phase lag relative to freestream conditions.

The most significant findings emerge in the dynamic stall domain. The presence of the ground plane serves as a powerful stabilising mechanism. By imposing a vertical geometric constraint, the wall suppresses the coherent roll-up and subsequent shedding of the Leading-Edge Vortex (LEV). This suppression of discrete vortex shedding replaces abrupt load collapses characteristic of classical dynamic stall with geometrically constrained separation. This transition results in a marked increase in aerodynamic damping, suggesting that ground proximity inherently mitigates the energy extraction mechanisms that typically trigger instabilities.

This work demonstrates that the non-dimensional height must be considered as a primary kinematic parameter, and reduced frequency alone is insufficient to characterise unsteady stall in ground effect. These insights provide a quantitative foundation for the development of active aerodynamic control systems and offer a physical explanation for the suppression of porpoising in high-downforce racing applications and low-flying vehicles.

Contents

List of Figures

List of Tables

Nomenclature

Abbreviations

Abbreviation	Definition
$2D$	Two Dimensional
$3D$	Three Dimensional
AC	Aerodynamic Centre
AR	Aspect Ratio
AoA	Angle of Attack
BL	Boundary Layer
CFD	Computational Fluid Dynamics
DAQ	Data Acquisition system
DES	Detached Eddy Simulation
DNS	Direct Numerical Simulation
DSV	Dynamic Stall Vortex
$HFSB$	Helium Filled Soap Bubbles
IGE	In Ground Effect
LE	Leading Edge
LED	Light Emitting Diode
LEV	Leading-Edge Vortex
LDA	Laser Doppler Anemometry
OGE	Out of Ground Effect
OJF	Open Jet Facility
PIV	Particle Image Velocimetry
$PTV/3D-PTV$	3D Particle Tracking Velocimetry
SST	Shear Stress Transport
TAT	Thin Airfoil Theory
TE	Trailing Edge
$URANS$	Unsteady Reynolds-Averaged Navier-Stokes

Symbols

Symbol	Definition	Dimensions
b	Semi-chord ($c/2$)	[m]
c	Chord Length	[m]
C_a	Coefficient of Axial Force	[$-$]
C_d	Coefficient of Drag	[$-$]
C_{d_i}	Coefficient of Induced Drag	[$-$]
C_ℓ	Coefficient of Lift	[$-$]
$C_{\ell,max}$	Maximum Coefficient of Lift	[$-$]
C_{ℓ_∞}	Coefficient of Lift (OGE)	[$-$]
$\bar{C_\ell}$	C_ℓ (IGE) normalised with C_{ℓ_∞} (OGE)	[$-$]
C_L	Coefficient of Lift ($3D$)	[$-$]
C_n	Coefficient of Normal Force	[$-$]
C_P	Coefficient of Pressure	[$-$]
h	Height of quarter-chord from the ground	[m]
H	Height to chord ratio	[$-$]
h_{TE}	Height of TE to chord ratio	[$-$]
k	Reduced Frequency	[$-$]
L	Lift Force	[$kgms^{-2}$]
M	Mach Number	[$-$]

Symbol	Definition	Dimensions
P_0	Total Pressure	$[kgm^{-1}s^{-2}]$
P_∞	Freestream Static Pressure	$[kgm^{-1}s^{-2}]$
Q_∞	Freestream Dynamic Pressure	$[kgm^{-1}s^{-2}]$
Re	Reynolds Number	$[-]$
St	Strouhal Number	$[-]$
t	Time from start of oscillation	$[s]$
T	Time Period	$[s]$
U_∞	Freestream Velocity	$[ms^{-1}]$
V	Velocity	$[ms^{-1}]$
x	x-position of the airfoil	$[m]$
y	y-position of the airfoil	$[m]$
$\Delta\alpha$	Amplitude	$[rad]$
α	Angle of Attack	$[rad]$
α_o	Mean Angle of Attack	$[rad]$
Γ	Circulation	$[m^2s^{-1}]$
ρ	Density	$[kgm^{-3}]$
ρ_∞	Density (Freestream)	$[kgm^{-3}]$
μ	Dynamic Viscosity	$[kgm^{-1}s^{-1}]$
ω	Rotational Frequency	$[s^{-1}]$
ϕ	Velocity Potential	$[m^2s^{-1}]$
Φ	Phase-lag between the heave and pitch motions	$[rad]$
$\Omega\|\omega_i$	Vorticity	$[s^{-1}]$

1

Introduction

Wings operating close to the ground have long been of interest in aerodynamics due to the substantial modifications induced in the surrounding flow field. When a lifting surface approaches the ground, the boundary alters the streamline curvature, suppresses vertical velocity components, and modifies the pressure distribution, often resulting in an enhanced aerodynamic normal force (manifesting as either lift or downforce, depending on the orientation) and reduced induced drag. This phenomenon, broadly referred to as *ground effect*, has been observed across a wide range of natural and engineered systems and deliberately exploited in applications ranging from biological flight to engineered vehicles. In nature, many birds deliberately exploit ground effect to reduce energetic cost. Large seabirds such as pelicans, as shown in Figure 1.1, frequently fly close to the sea surface, benefiting from increased lift-to-drag ratio and reduced induced losses during long-distance flight.

From an engineering perspective, the deliberate exploitation of ground effect has underpinned the development of diverse systems, from large-scale wing-in-ground (WIG) craft, such as the ekranoplans shown in Figure 1.2a, to modern unmanned aerial vehicles (UAVs) and rotorcraft [2, 3], as shown in Figure 1.2b. In these applications, proximity to a boundary—whether a solid runway or a fluid free-surface—is used to achieve lift-to-drag ratios and thrust efficiencies unattainable in freestream flight. However, while classical analysis often treats these operations as quasi-static, many practical scenarios involve intrinsic unsteady motions.

In many practical applications, airfoils do not operate at a fixed angle of attack (α) or constant ground clearance (h); unsteady motion is intrinsic rather than exceptional. Whether through the flapping kinematics of biological flyers near boundaries [6], the cyclic pitching of a rotor blade [7], or the oscillatory plunging of a marine foil [8], these systems experience rapid fluctuations in the effective angle of attack. This motion in ground effect introduces significant aerodynamic complexity, modulating the bound circulation and transient separation characteristics in a manner that differs fundamentally from quasi-steady behaviour. Such conditions give rise to pronounced hysteresis in aerodynamic loads, phase lag in force response, and a strong coupling between the wing kinematics and the resulting wake dynamics [9, 10, 11]. Understanding these unsteady effects is therefore essential for accurately predicting the loads, stability, and performance of any system operating near a boundary.

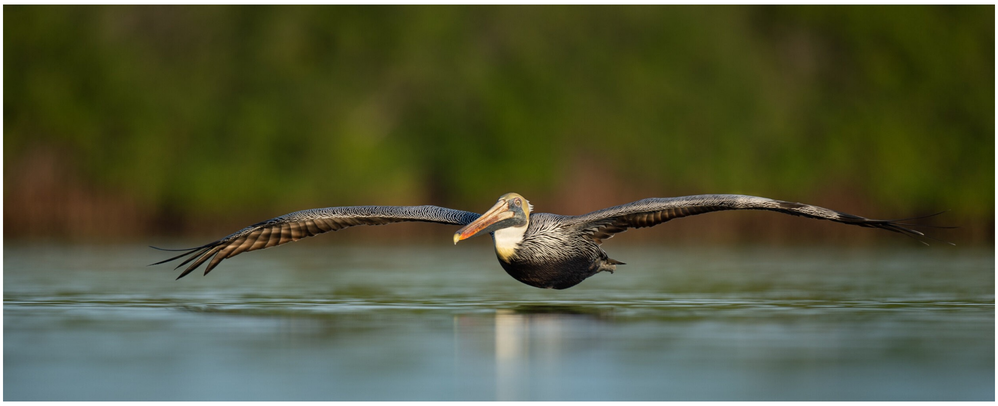

Figure 1.1: A pelican flying close to the surface of water [1].

(a)

(b)

Figure 1.2: Examples of vehicles operating in ground effect: (a) a modern ekranoplan exploiting lift augmentation [4]; (b) a helicopter experiencing modified induced flow during hover [5].

A prominent contemporary example of unsteady aerodynamics in ground effect is found in Formula 1 racing. The reintroduction of ground-effect regulations in 2022, following a four-decade absence since 1982 [12, 13], shifted aerodynamic performance back towards underbody-driven downforce. Formula 1 cars from this era of regulations relied on underfloor Venturi tunnels and diffusers to accelerate the flow beneath the floor, reducing static pressure and generating large suction forces that enhance tyre grip while limiting drag penalties associated with complex external wings. Operating extremely close to the track renders such systems highly sensitive to ride height and pitch. Small vertical excursions can lead to large variations in aerodynamic load, sometimes giving rise to a self-excited oscillatory instability known as *porpoising*, illustrated in Figure 1.3. In this phenomenon, the coupling between unsteady aerodynamic forces and vehicle motion produces large-amplitude oscillations in ride height and pitch. The physics underpinning porpoising is closely related to unsteady ground-effect aerodynamics.

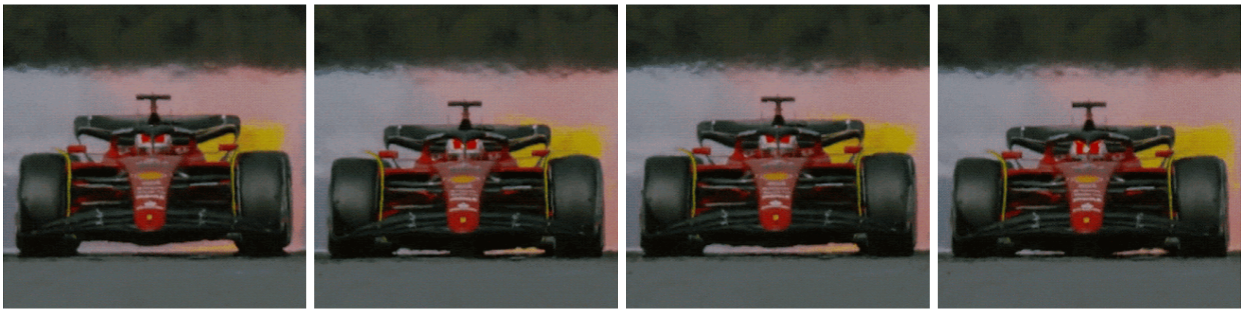

(a) $T = 0s$

(b) $T = 0.167s$

(c) $T = 0.333s$

(d) $T = 0.500s$

Figure 1.3: Frames depicting porpoising on an early 2022 Ferrari Formula 1 car during pre-season testing (Frames obtained from [14]).

Unsteady near-ground aerodynamics also arise in racing conditions due to both external disturbances and vehicle dynamics. If the front wing operates within the wake of a preceding car, it is subject to rapid variations in inflow velocity, turbulence intensity, and effective angle of attack. Bumps and kerbs on the track, which cause a transient change in ride height and pitch, introduce additional excitations. Together, these effects impose rapid fluctuations in ground clearance and effective angle of attack, leading to time-dependent aerodynamic responses analogous to those encountered by a pitching wing operating in ground effect.

The latest regulations further reinforce the prominence of unsteady effects. The 2026 Formula 1 Technical Regulations formalise the use of movable aerodynamic devices through two-state front and rear wings, with the front wing operating in proximity to the ground [15]. Activation of such devices inherently introduces time-dependent aerodynamic behaviour, closely aligning with the physics of pitching wings in ground effect, where dynamic lift response, hysteresis, and wing-ground interactions dominate the flow behaviour. Figure 1.4 shows pre-season testing of the 2026 front wing concept, highlighting the continued emphasis on near-ground aerodynamic performance.

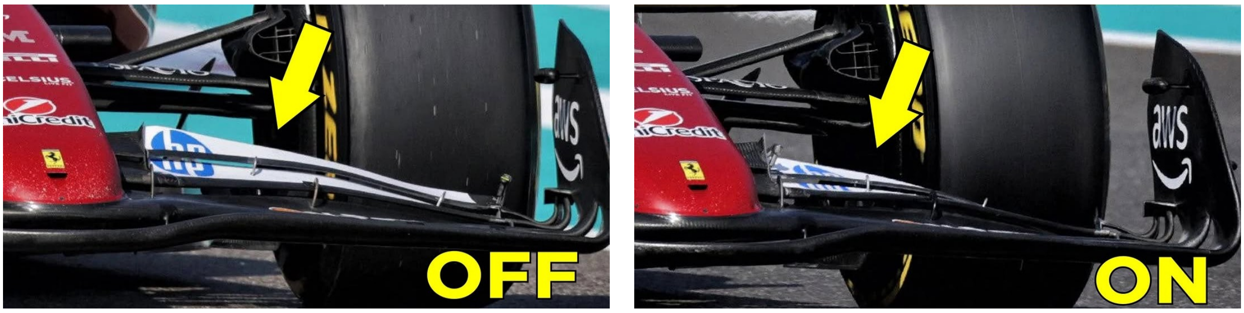

Figure 1.4: Pre-season testing of the 2026 front wing configuration in Abu Dhabi (Adapted from [14]).

Against this backdrop, this thesis builds on the fundamental aerodynamics of a wing operating in ground effect, with particular emphasis on both steady and unsteady pitching motions. Rather than addressing a specific vehicle configuration, the work aims to isolate and characterise the underlying flow physics governing lift generation, hysteresis, and force modulation near a ground plane. By doing so, it provides a framework that is applicable across a wide range of systems, from biological flyers and marine propulsion to ground-effect vehicles and high-performance racing aerodynamics. The following chapter reviews the existing literature and theoretical foundations relevant to wings in ground effect, establishing the context for the experimental and numerical investigations that follow.

2

Background

To establish a rigorous foundation for the current investigation, this chapter reviews the fundamental theoretical and experimental principles relevant to airfoils in both out-of-ground-effect (OGE) and in-ground-effect (IGE) conditions. Steady potential flow and boundary layer theory provide the baseline against which we compare ground-induced modifications to the flow field. The discussion then extends to unsteady aerodynamics, where the concepts of reduced frequency and phase lag are introduced. Finally, a comprehensive review of the existing literature identifies the current understanding of unsteady wing–ground interactions, highlighting gaps in the understanding of Reynolds-number effects and diagnostic resolution that the present work aims to address.

2.1. Steady Aerodynamics in Free Air

Steady aerodynamics in unbounded flow builds upon the idealised potential-flow concepts—namely, inviscid and irrotational flow. In potential flow, the pressure field is governed solely by the velocity potential (ϕ), and the net aerodynamic force is determined by integrating the surface pressure. Although potential flow neglects viscous stresses, the superposition of elementary solutions (sources, vortices, doublets) provides tractable models of attached-flow behaviour. It yields the classical relation between circulation and lift established by the *Kutta–Joukowski theorem* ($L = \rho_\infty U_\infty \Gamma$). *Thin–airfoil theory* (TAT) follows from this framework by representing the airfoil as a vortex sheet of unknown strength and enforcing the *Kutta condition*— enforcing the rear stagnation point at the trailing edge. The underlying vortex-sheet formulation connects circulation directly to the pressure distribution via the Bernoulli equation, establishing a consistent inviscid model of $2D$ lift generation [16, 17]. Equation 2.1 captures the linear C_ℓ–α behaviour observed in Figure 2.1.

$$C_\ell = C_{\ell_0} + 2\pi\,\alpha \tag{2.1}$$

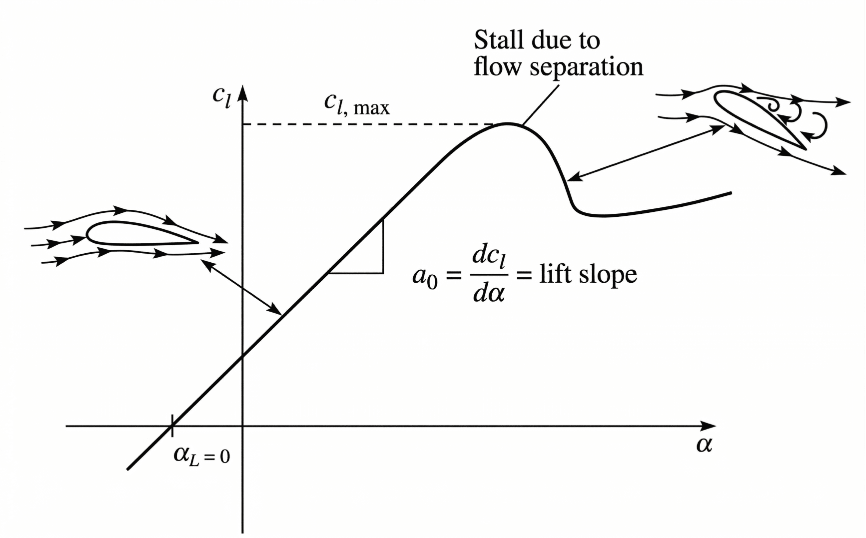

Figure 2.1: Schematic of lift-coefficient variation with angle of attack (α) of the airfoil [16].

While the theoretical inviscid lift slope is 2π per radian, real fluid effects such as viscosity play a crucial role, particularly as the angle of attack increases. In true free-air conditions, the lift curve typically exhibits a linear region followed by a maximum lift coefficient ($C_{\ell,max}$), after which the lift falls off into a plateau or drops sharply due to stall. The thickening of the boundary layer and eventual flow separation lead to a departure from the inviscid model. This separation usually occurs at the trailing edge that moves forward rapidly as the angle of attack increases, eventually leading to a loss of suction surface loading. Furthermore, at low Reynolds numbers, the boundary layer may undergo transition via a laminar separation bubble, which significantly influences the linearity of the lift curve [16, 17].

The pressure distribution in free air typically features a suction peak near the leading edge on the suction surface, followed by a pressure recovery towards the trailing edge. The pressure on the pressure surface remains fairly constant and positive, while the suction surface bears the majority of the lift generation load. However, the specific distribution is highly sensitive to geometry; for example, adding Gurney flaps or altering camber can shift the zero-lift angle (α_L) and increase circulation (Γ), thereby altering the C_ℓ and C_d profiles.

2.2. Steady Aerodynamics in Ground Effect

The introduction of a rigid plane imposes a non–normal flow condition that can be modelled in inviscid theory by an image system below the wall, as illustrated in Figure 2.2. For lifting bodies, the image reduces downwash and alters the induced velocity field, thereby modifying both lift slope and induced drag. In lifting–line form, the presence of the image effectively increases apparent aspect ratio and reduces C_{d_i} at fixed C_ℓ; conversely, for the downforce orientation, the same mechanism amplifies downforce and sensitivity to ride height [17, 18, 19].

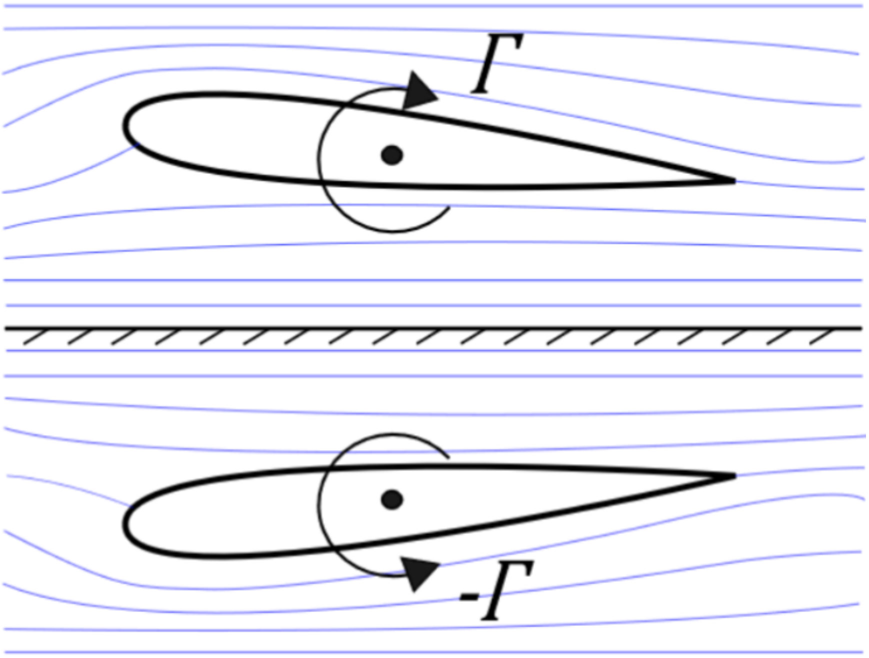

Figure 2.2: Visualisation of the mirrored ground effect using the method of images [20].

Within this framework, Katz and Plotkin [17, 18] derived closed–form expressions for the circulation and lift coefficient of a $2D$ airfoil operating near a ground plane by enforcing the Kutta condition. The resulting expressions demonstrate how the ground clearance enters as a perturbation parameter, modifying both the effective angle of attack and the pressure distribution around the airfoil. The circulation and lift coefficient are given by

$$\Gamma = \pi U_\infty c \cdot \sin\alpha \left(\frac{1 - (1/2H)\sin\alpha + 1/16H^2}{1 - (1/4H)\sin\alpha} \right), \tag{2.2}$$

$$C_\ell = 2\pi \sin\alpha \left[1 - \frac{1}{2H}\sin\alpha + \frac{1}{16H^2}(1 + \sin^2\alpha) + O\left(\frac{1}{H^3}\right) \right], \tag{2.3}$$

where, the ground clearance h is measured from the quarter–chord location and non–dimensionalised by the chord c as $H = h/c$. At large clearances, the higher–order terms vanish and the classical thin–airfoil result is recovered. As H decreases, the perturbation terms grow rapidly, illustrating the strong non-linearity introduced by proximity to the ground.

As the flow between the airfoil and the ground is progressively constrained, it forms an effective converging-diverging passage analogous to a Venturi tunnel. The accelerated underbody flow reduces static pressure beneath the airfoil, enhancing lift (or downforce in the inverted configuration). Simple control–volume arguments link the increase in underbody mass flux to the reduction in available flow area, yielding additional pressure deficit compared to OGE that scales inversely with H and depends on camber and attitude [8, 17]. This mechanism explains the rapid growth of $|C_\ell|$ as the ground is brought closer. It underpins the high aerodynamic efficiency of wing–in–ground–effect systems, and its effect is illustrated in Figure 2.3.

The second term in Equation 2.3 indicates a competing effect at higher angles of attack. As α increases, the effective blockage intensifies and the pressure recovery near the trailing edge becomes increasingly adverse. This blockage reduces suction on the upper surface and, in some cases, results in a net decrease in lift for upright airfoils operating close to the ground. Experimental and numerical studies on cambered airfoils confirm that, at moderate to high angles of attack, the loss of upper–surface suction can offset the pressure gain beneath the airfoil, resulting in a non–monotonic variation of C_ℓ with decreasing H [21, 22].

For finite wings, additional $3D$ effects arise. The suppression of downwash reduces induced drag and alters the spanwise lift distribution, typically increasing central loading while weakening tip vortices. At sufficiently small clearances, the flow becomes chord–dominated rather than span–dominated, and the classical lifting–line assumptions begin to break down [2, 23].

Viscous effects play a central role in determining the practical limits of ground–effect performance. The accelerated underbody flow must decelerate through a diffuser–like region downstream, producing strong adverse pressure gradients. Boundary–layer separation on the suction surface or within the diffuser leads to abrupt losses of downforce, commonly referred to as choking. Zerihan et al. [19] demonstrated experimentally that this phenomenon is responsible for the collapse of downforce at critical ride heights, accompanied by thickened wakes and increased unsteadiness. Numerical investigations of single and multi–element wings in ground proximity have shown similar behaviour [24, 25].

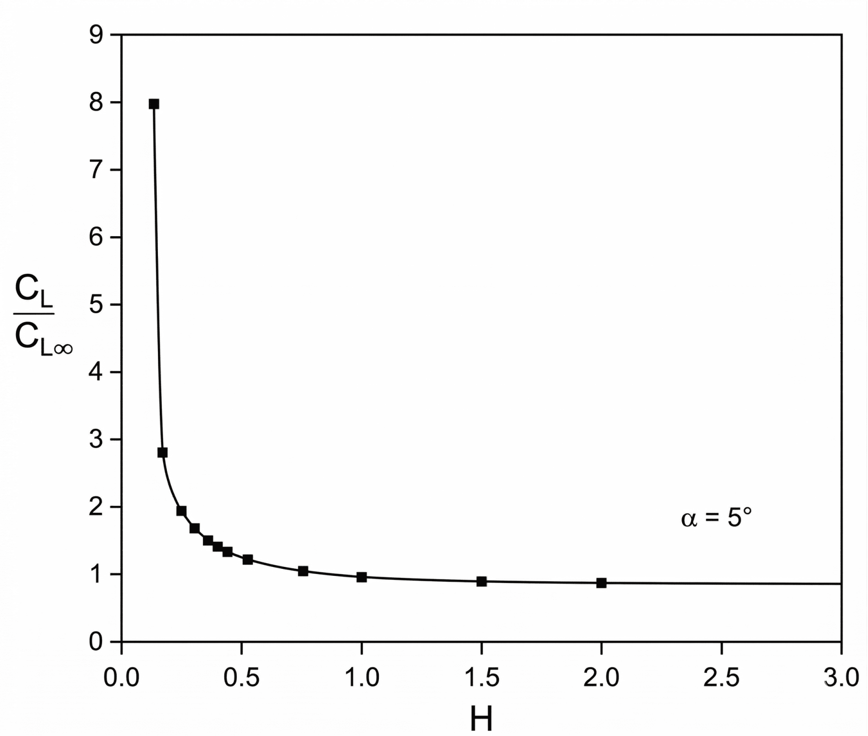

Figure 2.3: Effect of ground proximity (with no viscous effects) on the lift of an airfoil [18].

The inviscid trends illustrated in Figure 2.3 therefore represent an upper bound on achievable performance. In real applications, the interactions among ground proximity, viscous separation, and wake development govern the usable operating envelope.

2.3. Unsteady Aerodynamics

If the profile's motion changes over time, so do the acting aerodynamic coefficients. When the changes in motion are sufficiently rapid, the body's aerodynamic response no longer follows its kinematics instantaneously. Instead, it exhibits a phase lag with respect to the imposed motion. Physically, the finite time required for vorticity to be generated at the airfoil, convected into the wake, and for the surrounding flow field to adjust is the reason for this lag. As the characteristic time scale ($1/f$) of the motion becomes comparable to, or smaller than, the convective time scale (c/U_∞), the inertia of the displaced fluid contributes significantly to the total aerodynamic loading through so-called apparent (or added) mass effects. If the apparent mass contribution is negligible, the response may be treated as quasi-unsteady, in which the instantaneous aerodynamic loads depend only on the instantaneous kinematic state of the airfoil [26].

Classical linearised unsteady aerodynamic theories, notably those developed by Theodorsen [27] and Wagner [28], provide a rigorous framework for describing this behaviour for thin airfoils undergoing small-amplitude harmonic motions in attached flow. These theories introduce the reduced frequency ($k = \frac{\omega c}{2U_\infty}$) as the primary non-dimensional parameter governing unsteady effects and employ complex transfer functions to relate the harmonic motion of the airfoil to the resulting unsteady lift. Where ω is the frequency of oscillation, c is the chord of the airfoil, and U_∞ is the freestream velocity.

Theodorsen decomposes the unsteady lift into circulatory contributions, associated with bound circulation and wake vorticity, and non-circulatory contributions, associated with the acceleration of the surrounding fluid. The latter manifests as an added-mass term and dominates at high frequencies or during rapid accelerations.

For small oscillation amplitudes and moderate reduced frequencies, the unsteady lift may be expressed as a linear superposition of these circulatory and non-circulatory components. In this domain, the assumption is that the wake remains thin and planar, and the flow remains fully attached to the airfoil surface. For modest angles of attack, these assumptions provide a fair agreement with experimental data for attached-flow conditions [29, 30]. However, as either the oscillation amplitude or the reduced frequency increases, the flow response becomes strongly non-linear. Phenomena such as dynamic stall, large-scale vortex shedding, and hysteresis in the lift and moment coefficients emerge, invalidating the linear superposition principle. In these domains, the instantaneous aerodynamic loads depend not only on the current kinematic state, but also on the prior motion history and the evolution of flow structures in the near wake [31].

At low to moderate Reynolds numbers, non-linear effects play a particularly pronounced role, as laminar separation bubbles and their unsteady evolution dominate the flow. Periodic motion can significantly alter the formation, growth, and bursting of such bubbles even when the static airfoil operates below stall [32]. Experimental and numerical studies show that a complex interaction between boundary-layer transition, shear-layer instability, and vortex roll-up governs the phase lag between motion and aerodynamic response, rather than reduced frequency alone.

For a prescribed harmonic motion consisting of pitch $\alpha(t) = \alpha_o \cdot e^{i\omega t}$ and heave $h(t) = h_0 \cdot e^{i\omega t + \Phi}$, the time-varying lift coefficient may be approximated, following Daliri et al. [33], as

$$C_\ell(t) = 2\pi C(k_1)\left[\alpha + \frac{c\dot{\alpha}}{2U_\infty}\right] - 2\pi C(k_2)\frac{\dot{h}}{U_\infty} + \frac{\pi c}{2}\left[\frac{\dot{\alpha}}{U_\infty} - \frac{\ddot{h}}{U_\infty^2} + \frac{c\ddot{\alpha}}{4U_\infty^2}\right] \tag{2.4}$$

Since this study considers a pitching motion, Equation 2.4 reduces to

$$C_\ell(t) = 2\pi C(k)\left[\alpha + \frac{c\dot{\alpha}}{2U_\infty}\right] + \frac{\pi c}{2}\left[\frac{\dot{\alpha}}{U_\infty} + \frac{c\ddot{\alpha}}{4U_\infty^2}\right] \tag{2.5}$$

where $C(k)$ denotes a Theodorsen transfer function and overdots indicate time derivatives, and Φ is the phase-lag between the heaving and pitching motions. The first two terms represent the circulatory lift associated with pitching and heaving motions, respectively, while the final term corresponds to the non-circulatory (added-mass) contribution.

Although expressions such as Equation 2.4 retain a firm theoretical basis within linear unsteady aerodynamics, their applicability is inherently limited to attached-flow conditions. Strong separation, dynamic stall, or proximity-induced effects such as ground effect require additional modifications. Experimental investigations of oscillating airfoils near solid boundaries demonstrate significant amplification of hysteresis and alterations in phase lag compared to freestream conditions, attributed to modified pressure recovery, wake confinement, and altered vorticity dynamics, discussed in more detail in subsection 2.5.2. These findings highlight the need for careful interpretation of linear unsteady models when extending them to complex, non-linear flow domains relevant to wing–ground interaction problems.

2.4. Unsteady Aerodynamics in Ground Effect

As discussed in section 2.2, the ground influence extends beyond the steady pressure field to the unsteady evolution of circulation and the subsequent wake. In unsteady formulations, this constraint is satisfied through the method of images, whereby a mirror system of bound and wake vortices is introduced below the ground plane, as illustrated in Figure 2.4. Katz and Plotkin [17] describe this treatment of solid boundaries in unsteady potential flow, emphasising that image systems remain valid for time-dependent vortex shedding provided the wake evolution is treated consistently.

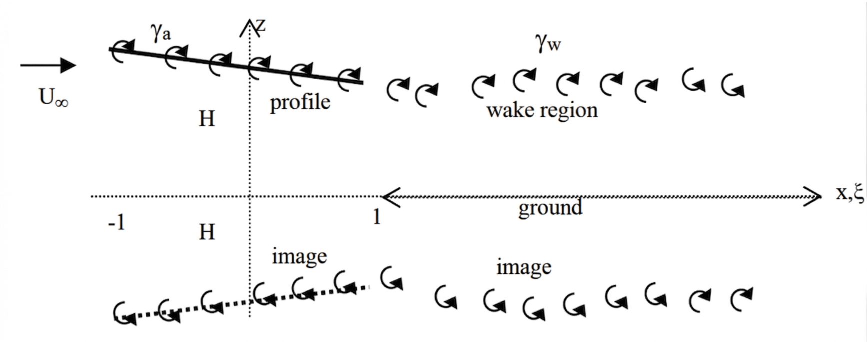

Figure 2.4: Bound and Image Vortices and their wake [26].

The consequence of this mirrored vortex system is a dynamic coupling between the physical airfoil and its image, such that changes in bound circulation on the airfoil instantaneously influence the induced velocities acting on both the airfoil and its wake. In contrast to freestream unsteady aerodynamics, where wake-induced effects decay downstream, the presence of the ground maintains strong interaction between the wake and the lifting surface over a larger portion of the oscillation cycle [9]. This leads to modified phase relationships between motion, circulation, and aerodynamic loading, particularly at low ground clearances. Rozhdestvensky [8] notes that non-circulatory (added-mass) forces amplify significantly as $H \to 0$; as the ground traps the fluid in an increasingly rigid ”container” between the airfoil and the ground, the inertia of the displaced fluid begins to dominate the total unsteady response.

In the framework of linear unsteady potential flow theory, the governing integral formulation accounts for both the bound vortex sheet on the airfoil and the shed wake vortices, together with their image counterparts [26]. At closer proximity to the ground, viscous effects become increasingly important, even when the outer flow remains predominantly inviscid. Numerical simulations and experiments have shown that the interaction between the oscillatory motion and the ground can promote earlier flow separation on the suction surface, enhance hysteresis in the lift response, and modify the timing of dynamic stall relative to freestream cases.

In addition to lift modulation, unsteady ground effect significantly influences wake structure. Studies of flapping and pitching foils operating near the ground reveal transitions between classical von Kármán, reverse von Kármán, and chaotic wake patterns depending on the oscillation frequency, amplitude, and ground clearance. The interaction between the lower-surface vortices and the ground plane can produce jet-like flows that contribute to thrust generation, a mechanism that bio-inspired propulsion and morphing-wing concepts have exploited [11, 34]. Recent work on periodically morphing airfoils in ground effect has further shown that wake coherence and force oscillation amplitude are strongly governed by the interplay between unsteady circulation and ground-induced confinement [35].

Overall, one cannot interpret unsteady aerodynamics in ground effect as a simple modification of freestream unsteady theory. Instead, the presence of the ground fundamentally alters wake dynamics, phase relationships, and the mechanisms of force generation. While linear potential-flow models with image vortices provide valuable physical insight and remain effective at moderate ground clearances, accurate prediction of unsteady loads at very low heights requires accounting for viscous effects, separation, and non-linear wake–ground interactions. These complexities underline the importance of unsteady ground-effect aerodynamics.

2.5. Literature Review

The aerodynamic interaction between a lifting surface and a ground plane has been the subject of extensive research due to its applications in take-off and landing performance, wing-in-ground (WIG) effect vehicles, and automotive aerodynamics. While steady-state ground effect is well documented, the coupling of unsteady kinematics, specifically pitching motions near the ground, remains a developing field. This section reviews the pertinent experimental and numerical studies, categorising them into steady ground effect and unsteady ground effect, further subdividing the latter into propulsion-focused and stability-focused research.

2.5.1. Steady Aerodynamics in Ground Effect

The fundamental understanding of chord-dominated ground effect relies heavily on early experimental campaigns for accurate predictions, particularly where the flow is essentially two-dimensional. The consensus indicates that ground proximity alters the pressure distribution, enhancing lift via blockage and ram effects while simultaneously modifying boundary-layer development.

Jones [36] established a rigorous *theoretical* foundation for chord-dominated ground effect by employing *matched asymptotic expansions* to investigate the boundary conditions at the trailing edge. His work demonstrated that ground proximity essentially ”stiffens” the trailing edge Kutta condition; as the boundary physically constrains the flow between the airfoil and the ground, the fluid is less able to navigate the trailing edge to equalise pressure. This constraint prevents large pressure differentials from developing at the rear of the profile, forcing a rapid, near-instantaneous upstream adjustment of the entire pressure field and bound circulation.

Valenzuela et al. [37] recently compared *inviscid panel methods (Vortex Lattice)* against a *k-ω SST model* for finite NACA 0012 wings in ground effect. They confirmed that potential flow methods can predict general lift trends but fail to capture the stall onset and separation characteristics that are critical at low ground clearances, further validating the need for experimental data in viscous-dominated domains.

Ahmed et al. [38] provided an experimental dataset for symmetric airfoils. They tested a NACA0015 airfoil in a *low-turbulence wind tunnel* at a Reynolds number of $Re \approx 2.4 \times 10^5$. Through *surface pressure measurements*, they identified two distinct aerodynamic domains dictated by the angle of attack (α). At low angles of attack ($\alpha \leq 5°$), a Venturi-effect accelerates the flow in the gap between the airfoil and the ground, reducing lift. However, at higher angles ($\alpha > 6°$), the passage becomes primarily convergent, constraining the flow and inducing a ram-pressure effect. This creates high static pressure on the lower surface, which significantly enhances lift.

Ahmed et al. [21] also examined a NACA 4412 profile at $Re \approx 3.0 \times 10^5$. Their setup utilised a *moving belt system* to eliminate the boundary layer at the floor, combined with a *six-component balance* and *hot-wire anemometry*. They reported that while lift increased near the ground, drag also increased significantly for this cambered profile due to changes in the lower-surface pressure distribution. This finding contrasts with the induced-drag reduction observed in finite wings.

Shirsath et al. [23] conducted *wind tunnel experiments* on a finite rectangular wing (NACA 0012, $AR = 6.4$) at a Reynolds number of $Re \approx 8.8 \times 10^4$ using a *6-axis force balance* and *k$-\omega$ SST* turbulence model. They found that while the lift curve slope generally increased with ground proximity, the stall angle was significantly influenced by the ground, with $C_{L,max}$ increasing by nearly 50% at the lowest clearance tested ($H = 0.4$) compared to free-flight.

Zerihan et al. [19, 39] performed a series of experiments on a single-element inverted Tyrrell 026 wing with a moving ground plane. Using *force balances*, *surface pressure taps*, *LDA*, and *2D PIV* at $Re \approx 4.6 \times 10^5$, they identified a downforce reduction as the wing approached the ground ($H \leq 0.1$). The immense suction peak caused the boundary layer to separate due to the severe adverse pressure gradient, leading to a loss of downforce.

In essence, whilst inviscid asymptotic frameworks provide an elegant description of the circulation ”stiffening” and ”ram-pressure” effects inherent in ground proximity, the experimental record reveals a far more nuanced reality dominated by complex viscous-inviscid interactions. The transition from a beneficial pressure-cushioning effect to the detrimental onset of flow separation marks a critical operational boundary that remains difficult to predict numerically. These steady-state limitations underscore the need to investigate how dynamic kinematics might further manipulate these sensitive flow structures, providing the impetus for the following review of unsteady aerodynamics in ground effect.

2.5.2. Unsteady Aerodynamics

The literature on unsteady wings in ground effect falls into two distinct domains based on research objectives: bio-inspired propulsion (which extensively utilises pitching and heaving kinematics to study thrust generation and efficiency), and stability and dynamic loading (which analyses the hysteresis and flutter of airfoils subjected to pitching and heaving disturbances).

Propulsion Focused Studies

Jones et al. [6] conducted both numerical and experimental investigations on flapping-wing propulsion. Numerically, they employed a $2D$ *unsteady inviscid panel code* with a deforming wake model alongside a $2D$ *unsteady compressible Navier-Stokes* solver. Their experiments utilised a heaving NACA0014 bi-plane in a wind tunnel, with the lower element virtually serving as the mirrored airfoil, as shown in Figure 2.2 and Figure 2.4. They employed a *smoke-wire* for qualitative flow visualisation, *Laser Doppler Anemometry* (LDA) for unsteady wake velocity measurements, and a laser range-finder for direct thrust measurement by suspending a model on strings, allowing it to move freely. They found that ground effect could enhance propulsive efficiency, but the benefits were highly sensitive to the Reynolds number, with inviscid panel codes failing to accurately predict performance at lower Reynolds numbers ($Re \approx 10^4$)

Moryossef et al. [9] conducted *Navier-Stokes simulations* of a heaving Tyrrell 026 wing at a Reynolds Number of $Re = 4.6 \times 10^5$ to identify the limits of inviscid models. They established a critical height threshold at approximately $H \approx 0.5$. Above this clearance, potential-flow image methods provided reasonable load predictions; however, below this threshold, viscous-confinement effects began to dominate, leading to a breakdown in quasi-steady assumptions and a significant divergence from classical potential-flow trends.

Mivehchi et al. [40] investigated a flapping (coupled pitch-plunge oscillation), high AR NACA0012 wing in a towing tank at a Reynolds number of $Re \approx 2.1 \times 10^4$. Using a *6-axis dynamometer*, they demonstrated that the presence of the wall enhances thrust generation for almost all tested kinematics. However, they emphasised that mean force measurements alone are insufficient to capture the wall's influence, necessitating time-resolved analysis.

Zhang et al. [41] numerically investigated a generic airfoil (semicircle leading edge, wedge trailing edge) undergoing large-amplitude flapping (coupled pitch-plunge oscillation) at $Re = 1 \times 10^3$ using a *laminar Navier-Stokes immersed boundary method*. They identified a sudden force dip during the upstroke at low clearances ($H \leq 0.3$) due to ground-induced blockage, noting that the resulting periodic asymmetry may compromise propulsive stability despite overall thrust enhancement.

Li et al. [42] utilised an *overlapping grid framework* to analyse both $2D$ and $3D$ flapping (coupled pitch-plunge oscillation) NACA0012 wings across varying Strouhal numbers and Reynolds numbers ($1 \times 10^2 \leq Re \leq 1 \times 10^6$). Depending on the flow domain, they employed a *laminar solver* for lower Reynolds numbers ($Re \leq 1 \times 10^3$) and a $URANS$ approach with the *Spalart-Allmaras* turbulence model for higher Reynolds numbers ($Re \geq 1 \times 10^4$). They confirmed that the ground restricts vertical wake development and deflects the vortex street at an oblique angle. They demonstrated that this ground-induced wake compression significantly enhances both thrust and propulsive efficiency at optimal frequencies.

Clements et al. [11] extended this to morphing geometries, simulating a NACA6409 with a periodically morphing trailing edge in ground effect at a Reynolds Number of $Re = 3 \times 10^5$. Using *Detached Eddy Simulations* (DES) with the *k*$-\omega$ *SST* turbulence model, they found that morphing induced a hysteresis loop in lift and drag that varies clockwise (energy extraction), and that specific morphing frequencies could generate forward thrust by manipulating the interaction between the lower-surface vortex and the ground plane.

Stability and Dynamic Stall Studies

Kang et al. [30] investigated the dynamic response of a pitching and heaving SD 7003 airfoil in OGE using $2D$ *PIV* and a *URANS* framework coupled with the *Menter k–*ω *SST turbulence model*. Their study highlighted a significant qualitative shift in flow structure across a Reynolds number range from 1×10^4 to 6×10^4. At the lower limit of this range, the unsteady motion triggered a massive flow separation that failed to reattach within the oscillation cycle. Conversely, at $Re = 6 \times 10^4$, the boundary layer possessed sufficient energy to reattach downstream of the primary Leading-Edge Vortex (LEV). These findings are particularly pertinent to the study of dynamic stall, as they demonstrate that even under strong kinematic forcing, the Reynolds number dictates the timing and coherence of vortex shedding and reattachment—mechanisms that fundamentally underpin the development of aerodynamic hysteresis.

Molina et al. [43] conducted a numerical investigation of the profile of a main element of a multi-element racing wing undergoing purely heaving motion in ground effect at Reynolds number of $Re = 3.9 \times 10^5$ using a $URANS$ framework with the *Spalart–Allmaras* turbulence model. By analysing the phase lag of the aerodynamic coefficients with respect to the vertical motion, they categorised the unsteady response into three distinct physical domains. At low frequencies, the flow is quasi-steady and predominantly governed by ground-induced pressure modulation. In the intermediate frequency range, the response becomes incidence-dominated, where the effective angle of attack drives the aerodynamic loads. Finally, at high frequencies, the non-circulatory added-mass effect becomes the primary driver of the aerodynamic forces, independent of ground proximity.

Building upon this, Molina et. al. [44] analysed the dynamic stability and wake structure of a heaving airfoil using a $URANS$ framework with the *Spalart–Allmaras* turbulence model. They developed a k–H contour map demonstrating that ground proximity can trigger stall flutter at low frequencies and low ride heights. In this domain, the airfoil enters the force-reduction region, causing the lift hysteresis loops to align anticlockwise. Consequently, the airfoil extracts energy from the fluid (negative aerodynamic damping), leading to potentially unstable, self-excited oscillations. Conversely, at higher frequencies, inviscid added-mass effects stabilise the motion. Furthermore, they observed that forced trailing-edge vortex shedding occurs at high frequencies, where ground proximity deflects the wake, leading to a complex three-way interaction between the shed vortices and the ground plane that can enhance thrust generation.

Molina et. al. [10] subsequently extended this framework to investigate purely pitching and combined pitching-heaving motions using a $URANS$ framework with the *Spalart–Allmaras* turbulence model. For purely pitching airfoils, they found that ground proximity exacerbates suction-side separation, causing the airfoil to stall at incidences well below its freestream static stall angle. For combined pitching and heaving motions, the aerodynamic response was heavily dictated by the phase shift between the two modes, with pitching governing the flow at low frequencies and heaving prevailing at high frequencies. Crucially, they demonstrated that a counter-phase motion (where maximum incidence occurs at the highest ground clearance) delayed stall, mitigated hysteresis, and increased overall downforce. Conversely, in-phase motion negatively interacted with the ground boundary, triggering premature, abrupt stall.

Lee et al. [34] provided a work most synonymous with the current work, an experimental investigation into the impact of ground proximity on a pitching NACA0012 airfoil at $Re \approx 9.8 \times 10^4$. Their experiments used an airfoil in sinusoidal pitching motion at a reduced frequency of $k = 0.05$. Using a stationary flat plate with a sharp leading edge, they derived aerodynamic loads from integrating *surface pressure taps* and performed flow visualisation using *oil-coated Nichrome smoke wires*. They observed that ground proximity substantially altered the dynamic lift loops. Specifically, for deep-stall motions, ground proximity significantly reduced the dynamic lift hysteresis as the airfoil approached the ground ($H < 0.3$). They attributed this to the blockage effect on the lower surface, which stabilised the flow and weakened the Dynamic Stall Vortex (DSV), causing it to break down earlier than in the freestream case. This resulted in a larger nose-down pitching moment and increased drag during the downstroke.

Doolabi et al. [45] further expanded on this using a higher Reynolds number. They tested a NACA0012 airfoil at $Re \approx 3 \times 10^5$ with a reduced frequency of $k = 0.026$ using pressure rake, surface pressure, and a *Transition SST* turbulence model. They modified the stationary ground plate by angling it slightly and adding a wedge piece to minimise the effects of the boundary layer. They utilised high-frequency response pressure sensors to capture transient loads. Their static results confirmed the transition from Venturi-dominated suction at low angles to blockage effect-dominated lift at high angles. In dynamic pitching cases, they observed that ground effect amplified the mean lift coefficient and also shifted the phase of the peak forces.

Chung et al. [35] provided a perspective on wake stabilisation by investigating the self-excited flow behind a heaving NACA0012 airfoil at a Reynolds number ($Re = 1 \times 10^3$) using *laminar viscous model*. By mapping the dynamics of forced synchronisation, they demonstrated that ground proximity serves as a powerful mechanism for suppressing chaos. In unbounded flow, forcing the airfoil at specific frequencies triggers the *Ruelle-Takens-Newhouse* route to chaos, breaking down a quasiperiodic torus attractor into low-dimensional deterministic chaos. However, as the airfoil approaches the ground, the physical boundary enhances the circulation of shed vortices and inhibits their dissipation. Dynamically, this regularises the shedding process, suppressing the chaotic domain and forcing a direct transition from two-frequency quasiperiodicity straight into a stable, 1:1 phase-locked periodic state.

In summary, the literature reveals that introducing unsteady kinematics into the ground-effect problem creates a highly non-linear aerodynamic landscape in which the ground acts as both a physical constraint and a flow-structure catalyst. Propulsive studies demonstrate that ground proximity can enhance efficiency through wake narrowing and 'ram' effects, and stability research highlights a domain in which the ground-plane boundary condition fundamentally alters the life cycle of the Leading-Edge Vortex (LEV)/Dynamic Stall Vortex (DSV). The emerging consensus suggests that the ground suppresses otherwise chaotic wake structures. Yet, the sensitivity of this interaction to the Reynolds number and reduced frequency remains a point of significant academic debate. Ultimately, the transition from quasi-steady pressure modulation to a domain dominated by viscous-confinement and added-mass effects delineates the current frontier of the field. This frontier demands higher-fidelity quantitative diagnostics to navigate.

Table 2.1: Summary of Select Investigations Reviewed

Steady Aerodynamics

Author	Investigation	Geometry	Ground	Re	Other Parameters
Jones [36]	Theoretical	Thin Airfoil	Moving	N/A	$H \to 0$
Valenzuela et al. [37]	Vortex Lattice, k-ω SST	NACA0012 Wing	Moving	$3.0e6$	$\alpha = 0^\circ$ to 12° $H = 0.4$ to 6
Ahmed et al. [21] (2007)	Surface Pressure, $2D\ PIV$	NACA4412	Moving	$3.0e5$	$\alpha = 0^\circ$ to 10° $H = 0.1$ to 1.0
Shirsath et al. [23]	Force, k-ω SST	NACA0012 Wing	Stationary	$8.8e4$	$\alpha = -8^\circ$ to 18° $H = 0.4$ to 1.5
Zerihan et al. [19] (2003)	Surface Pressure LDA, $2D\ PIV$	Tyrrell 026 Wing	Moving	$4.6e5$	$\alpha = 0^\circ$ $H \approx 0.1$ to 0.5

Unsteady Aerodynamics

Author	Investigation (Motion Type)	Geometry	Ground	Re	Other Parameters
Jones et al. [6]	Force, Smoke-wire, LDA, Vortex Panel (Flapping)	NACA 0014 Bi-plane	Symmetry Plane	$1e4$ to $1e6$	$k = 0$ to $2.0, \alpha = 0^\circ$ $H = 0.7, \Delta H = 0.4$
Moryossef et al. [9]	Second order NS - Goldberg (Heaving)	Tyrrell 026	Moving	$4.6e5$	$k = 0.06$ to 1.3, $\alpha = -3^\circ$ $H = 0.4$ to 0.8, $\Delta H = 0.1$
Mivehchi et al. [40]	Force (Flapping)	NACA0012	Moving	$2.1e4$	$St = 0.2$ to 0.5, $\alpha = 15^\circ$ to 45° $H = 1.33$ to 6
Zhang et al. [41]	Laminar (Flapping)	Semicircle LE + Wedge TE	Stationary	$1e3$	$k = 0.25$ to 1.5, $\alpha = 15^\circ$ to 30° $H = 0.25$ to 3, $\Delta H = 0.125$
Clements et al. [11]	DES, k-ω SST (Morphing TE)	NACA6409	Stationary	$3.2e5$	$St = 0.45$ to 4, $\alpha_o = 4^\circ$ $H = 0.1$, $\delta_{TE} = 0.1c$ to $0.3c$
Kang et al. [30]	$2D\ PIV$, k-ω SST (Flapping)	SD 7003	N/A	$1e4$ to $6e4$	$k = 0.25, St = 0.08$ $\alpha = 8^\circ$ to 13.6°
Molina et al. [43, 44]	$URANS - SA$ (Heaving/Pitching)	Custom Racing Wing	Moving	$3.9e5$	$k = 0$ to $4.37, \alpha_o\left[\Delta\alpha\right] = 5^\circ\left[5^\circ\right]$ $H = 0.16, 0.25, 0.43, \infty$
Lee et al. [34]	Surface Pressure, Smoke-wire (Pitching)	NACA0012 Wing	Stationary	$9.8e4$	$k = 0.05$, $\alpha_o\left[\Delta\alpha\right] = 5^\circ\left[5^\circ\right]$, $8^\circ\left[6^\circ\right], 11^\circ\left[6^\circ\right]$ $H = 0.1$ to 0.6
Doolabi et al. [45]	Surface Pressure, Pressure Rake, Transition SST (Pitching)	NACA0012	Stationary	$3e5$	$k = 0.026$, $\alpha_o\left[\Delta\alpha\right] = 0^\circ\left[1^\circ\right]$ $H = 0.1$ to 1
Chung et al. [35]	Laminar (Heaving)	NACA0012	Moving	$1e3$	$St = 0.79$ to 0.87, $\alpha = 10^\circ$ $H = 0.1$ to 0.8

2.5.3. Contribution of this work

While previous works establish a baseline, this thesis addresses specific gaps in diagnostic fidelity and parameter space:

1. **Reynolds Number Domain:** While Lee et al. conducted their comprehensive dynamic study at $Re \approx 9.8 \times 10^4$ [34], the current work is performed at $Re \approx 2 \times 10^5$. Although both values fall below the fully turbulent domain of motorsport/general aviation applications ($Re > 10^6$), prior research indicates that the flow physics in the range of $10^4 < Re < 10^5$ are highly non-linear, rendering the assumption of linearised lift characteristics invalid [23, 30, 45]. By doubling the Reynolds number relative to Lee et al., this study investigates a flow domain in which the boundary layer possesses sufficient energy to potentially alter the DSV breakdown and reattachment mechanisms, testing the validity of low-Re hysteresis findings in a more energetic transitional flow.
2. **Diagnostic Fidelity:** Previous experimental studies have largely relied on surface pressure taps [38, 21, 19, 34, 45], smoke-wire visualisation [6, 34], Laser Doppler Anemometry [6, 19] and $2D\ PIV$ [21, 19, 30]. While pressure taps provide load data, they cannot resolve the off-body vorticity field. This thesis employs high-fidelity, phase-resolved Particle Tracking Velocimetry (PTV). This measurement technique allows quantitative resolution of the velocity and vorticity field, enabling direct correlation of the Dynamic Stall Vortex (DSV) trajectory and circulation strength with the measured surface loads.
3. **Kinematic Parameter Space:** Existing literature often treats reduced frequency (k) and ground height (H) as separate variables and mainly focuses on positive angle of attack, especially for unsteady cases. This study hypothesises and demonstrates that k alone is insufficient to characterise unsteady stall in ground effect and adds to the discussion of an unsteady airfoil with a negative angle of attack. By systematically mapping the unsteady response across a matrix of reduced frequencies and ground clearances, this work provides a coupled understanding of how ground proximity modulates the time-scales of flow separation and reattachment, offering new insights into the suppression of aerodynamic hysteresis.

3

Methodology

This chapter outlines the experimental methodologies employed to characterise the aerodynamic behaviour of the investigated flow, discussing the underlying physical principles, measurement assumptions, and practical limitations of each technique to establish the reliability and resolution of the acquired data.

3.1. Pressure

A pressure tap consists of a small orifice flush with the model's surface, connected via tubing to a pressure transducer. When properly aligned with the local surface, the tap measures the static pressure of the flow at that location, which represents the pressure due to the fluid's random molecular motion. The hole must be sufficiently small and perfectly flush with the surface to avoid imperfections that would disturb the boundary layer and artificially alter the local pressure readings. By distributing pressure taps along the airfoil surface, one can obtain the spatial variation of static pressure. Integrating this pressure distribution over the body surface yields the resultant aerodynamic forces (such as lift and pressure drag) and moments acting on the model [16].

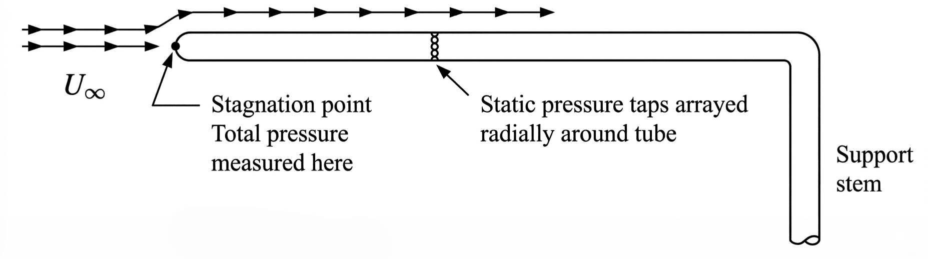

Figure 3.1: Pitot-static Probe [16].

$$\underbrace{q_\infty}_{\text{dynamic pressure}} = \underbrace{P_0}_{\text{total pressure}} - \underbrace{P_\infty}_{\text{static pressure}} = \frac{1}{2}\rho U_\infty^2 \tag{3.1}$$

A Pitot–static probe, illustrated in Figure 3.1, combines two pressure measurements within a single device. The forward-facing opening measures the total (stagnation) pressure by bringing the fluid elements to rest isentropically at the stagnation point. Meanwhile, circumferential side ports measure the static pressure of the undisturbed flow. For an incompressible flow, the difference between these two quantities exactly yields the dynamic pressure, as given in Equation 3.1, from which one can determine the freestream velocity. This relationship follows directly from Bernoulli's equation for incompressible, low-Mach-number flow and forms the basis for normalising surface pressures using the pressure coefficient (C_P) [16].

3.1.1. Coefficient of Pressure

$$C_P = \frac{P - P_\infty}{q_\infty} \tag{3.2}$$

Using Equation 3.1, one can show that the coefficient of pressure at the stagnation point—the point where the fluid comes to rest isentropically—is exactly 1, which is the highest allowable value of C_P anywhere in an incompressible flow field. Elsewhere, $C_P \leq 1$. In regions where the local velocity (V) accelerates and exceeds the freestream velocity U_∞, the local static pressure drops below P_∞, yielding a negative C_P [16].

3.2. Particle Image Velocimetry

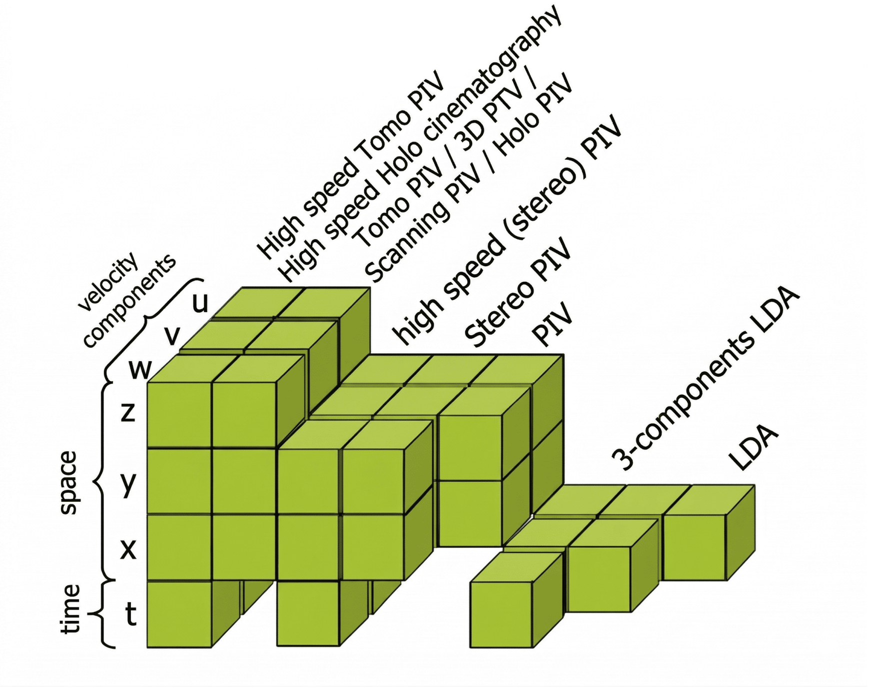

Figure 3.2: Measurement domain and measured components of velocimetry techniques [46].

Optical flow velocimetry techniques, such as Particle Image Velocimetry (PIV) and $3D$ Particle Tracking Velocimetry ($PTV/3D-PTV$), are non-intrusive, whole-field diagnostic tools used to capture instantaneous velocity fields. The fundamental theory behind these techniques relies on an indirect measurement principle: one infers the fluid velocity by calculating the displacement of small tracer particles over a known, short time interval. This relies on the critical assumption that the tracer particles faithfully follow the fluid's motion without disturbing the flow [47, 48].

The primary distinction between PIV and PTV lies in the particle image density required and the subsequent evaluation methods used to extract the velocity data [48]:

- **Particle Image Velocimetry:** operates at medium to high particle densities, where matching individual particles between sequential frames is visually ambiguous. Instead, the recorded images are divided into smaller sub-areas called interrogation windows, and statistical cross-correlation methods determine the mean displacement of the particle ensemble within each window. This yields a field of velocity vectors on a regular, *Eulerian* grid.
- **3D Particle Tracking Velocimetry:** operates at lower particle densities, allowing individual tracer particles to be identified and tracked from exposure to exposure using a *Lagrangian* approach. This provides highly localised velocity vectors on an irregular grid and avoids the spatial averaging bias inherent to the interrogation windows used in PIV.

Because fluid velocity is inherently a three-dimensional quantity, understanding complex flow structures and evaluating complete velocity gradient tensors requires expanding these basic measurement principles into multiple dimensions. Mapping the various components to the specific techniques is shown in Figure 3.2. Regardless of the technique or the dimensional space being investigated, the fundamental instrumentation of modern PIV systems comprises three core components: seeding, illumination, and recording/camera systems.

3.2.1. Seeding

Accurate velocity measurements in PIV/PTV rely on tracer particles that follow the flow without influencing it, acting as flow markers whose motion one records to infer the fluid velocity field [47, 48]. The tracers must be sufficiently small and neutrally buoyant so that their inertia does not cause a measurable lag relative to the fluid motion. The particle's response time, defined as the time required for a particle to adapt to changes in the local flow velocity, governs the degree to which it follows the flow. For accurate flow tracing, the particle response time must be significantly shorter than the characteristic time scales of the flow, resulting in a Stokes number below 10^{-1} [49]. When this condition is satisfied, the particle velocity closely approximates that of the surrounding fluid.

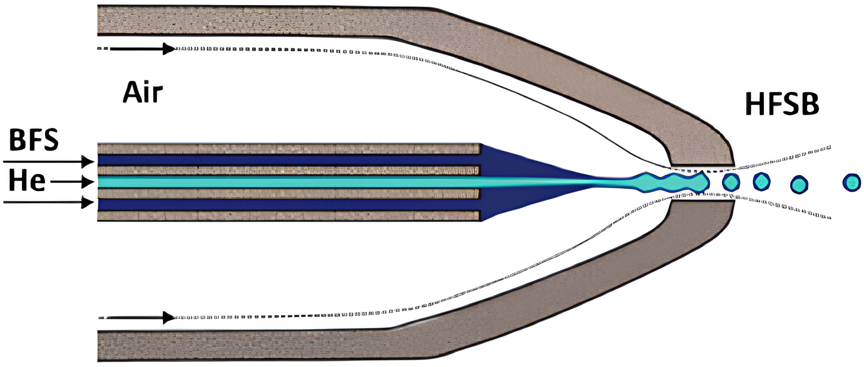

Figure 3.3: Schematic principle of helium-filled soap bubbles formation from a miniature generator [50].

Particle size represents a compromise between mechanical and optical requirements. Smaller particles ($\sim\ 10\,\mu m$) follow gas flows more accurately because of their low inertia, but they scatter significantly less light. In water flows, matching the fluid density is easier, allowing for larger particles ($\sim\ 100\ \mu m$) that provide stronger scattering and higher image contrast without deviating from the fluid motion. For large-scale aerodynamic investigations, researchers increasingly utilise neutrally buoyant Helium-Filled Soap Bubbles ($HFSB$) at the sub-millimetre scale due to their excellent tracing fidelity and large light-scattering cross-section. Figure 3.3 illustrates the seeder for the $HFSB$.

3.2.2. Illumination

Illumination of the tracer particles is a key element, as the accuracy of velocity measurements depends on the sharpness and uniformity of the recorded particle images. While traditional PIV relies on a thin light sheet, volumetric techniques require expanding the laser beam into a much thicker measurement volume. Expanding the beam significantly reduces the light energy density, which is widely regarded as the primary limiting factor when scaling up tomographic experiments [46, 48].

Pulsed laser systems, such as dual-cavity Nd:YAG or Nd:YLF lasers, are typically used because they generate short, intense, monochromatic light bursts that 'freeze' particle motion, preventing image streaking. To compensate for the loss of illumination intensity in a volume, double-pass or multi-pass light amplification systems are frequently employed. By arranging highly reflective mirrors around the measurement domain, the laser beam is reflected multiple times through the volume, thereby amplifying the scattered light intensity by a factor of 5 to 7. Additionally, knife-edge filters are often positioned along the optical path to sharply cut the light intensity beyond the nominal thickness of the measurement volume; any light recorded from outside the reconstructed volume will project back into the reconstruction and severely increase noise [46, 48, 51].

For lower-intensity or large-scale applications where laser safety or cost is a concern, high-power Light-Emitting Diodes (LEDs) provide a viable alternative. Pulsed LEDs produce broad-spectrum light that can successfully illuminate large volumes, particularly when paired with highly reflective tracers like $HFSB$ in air or coated glass spheres in water [48].

3.2.3. High-Speed Cameras

The recording system captures the light scattered by the tracer particles at discrete time intervals to evaluate their displacement. Beyond the basic hardware capabilities of modern high-speed sensors, the accuracy of the measurement relies heavily on the physics governing the time separation between successive snapshots, Δt. This time interval dictates the dynamic velocity range and the overall measurement uncertainty. A sufficiently long Δt is necessary to maximise the particle displacement relative to the imaging resolution, thereby minimising the relative random error in the velocity measurement. Conversely, if Δt is too large, it exacerbates truncation errors when resolving highly curved trajectories. It increases the likelihood that particles will travel beyond the boundaries of their respective interrogation windows or advect entirely out of the illuminated measurement volume before the camera records the second frame. This creates a situation in which many particles captured in the first exposure cannot be matched to corresponding images in the second exposure. Having too many unpaired particles degrades the cross-correlation signal, contributes to background noise, and consequently increases the overall uncertainty of the velocity estimation. To capture these precisely timed snapshots and mitigate these displacement errors, researchers arrange multiple synchronised cameras to observe the measurement volume from different angles, enabling accurate three-dimensional reconstruction [48].

3.3. Shake the Box

Shake-The-Box (STB) is a volumetric Lagrangian particle tracking methodology developed to extend the applicability of three-dimensional particle tracking to flows with significantly higher particle image densities. While classical triangulation-based $3D - PTV$ is typically limited to low seeding concentrations ($\simeq 0.005$ particles per pixel) to avoid tracking ambiguities [48, 51], STB extends tracking capability to significantly higher particle image densities.

The central concept of the approach is the explicit use of temporal information to guide particle reconstruction and tracking across successive time steps. Rather than reconstructing particle positions independently at each instant, previously identified trajectories are extrapolated forward in time, typically utilising a Wiener filter predictor. These predicted positions are then iteratively corrected through image-based optimisation, a process commonly referred to as ”shaking”. This strategy substantially reduces reconstruction ambiguity and suppresses the formation of ghost particles. Any new particles entering the measurement volume are subsequently identified on the largely empty residual images using an Iterative Particle Reconstruction step [48].

While standard STB relies on long, continuous time-resolved sequences to establish these extended trajectories, many high-speed aerodynamic applications face hardware limitations that prevent continuous recording. To investigate periodic phenomena under these constraints, the acquisition strategy must shift to phase-resolved measurements [46, 48]. Here, tracking relies on short image bursts—typically double-frame or four-pulse recordings acquired in a phase-locked manner. This method utilises an iterative strategy that alternates between Iterative Particle Reconstruction and predictive particle tracking to progressively increase the number of successfully retrieved short particle tracks from the brief image sequences [48].

Because the flow is periodic, measurements are repeated many times at the same phase of the motion. By aggregating these repeated measurements, one collects a massive ensemble of instantaneous, highly localised Lagrangian tracks for each phase. Rather than analysing temporal derivatives along a single long trajectory, these sparse, phase-locked tracks are ensemble-averaged and assimilated onto a regular Eulerian Cartesian grid. This phase-averaging process suppresses random measurement noise, significantly increases the signal-to-noise ratio, and provides highly accurate, sub-pixel-resolved statistical flow quantities—such as the mean velocity field, and Reynolds stresses—for each distinct phase of the cycle [48].

4

Experimental Setup

This chapter describes the experimental facility, model design, and measurement systems employed in the investigation. The chapter first introduces the layout of the wind tunnel and supporting structure, followed by a detailed description of the airfoil, ground plate, pitching mechanism, and instrumentation. It then discusses the geometric limitations associated with ground proximity and the resulting constraints on angle of attack. Finally, it presents the diagnostic techniques used to acquire pressure and velocity field data, along with the test matrix definition, to provide a complete overview of the experimental methodology.

4.1. Experimental Facility and Setup Design

A substantial part of this study was devoted to the design and integration of an experimental setup to investigate unsteady airfoil aerodynamics in proximity to the ground. The configuration had to accommodate controlled pitching motion, high-fidelity pressure measurements, and time-resolved optical flow diagnostics, while remaining compatible with optical constraints. The design placed particular emphasis on achieving mechanical rigidity, accurate kinematic control, and quasi-two-dimensional flow conditions to ensure the reliability and repeatability of the measurements.

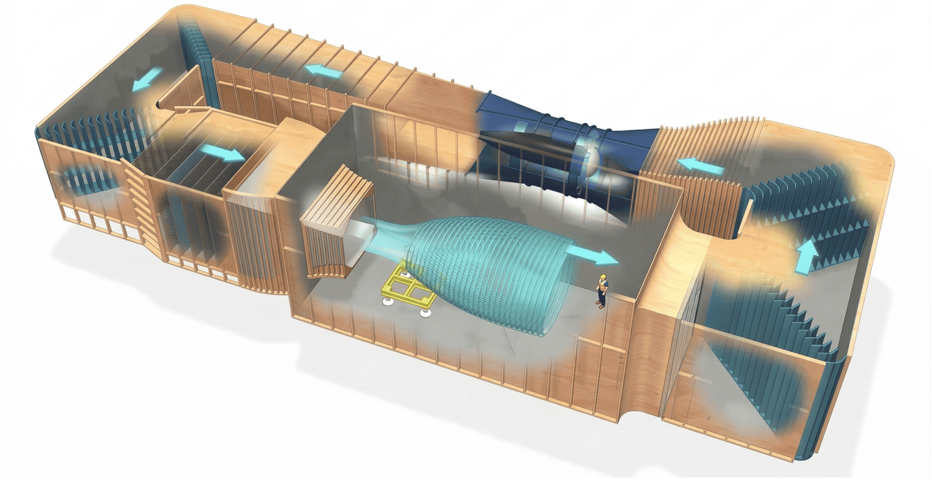

Figure 4.1: Schematic of Open Jet Facility at TU Delft [52].

The experimental setup was designed to operate within the Open Jet Facility (OJF) of TU Delft's Aerospace Engineering High-Speed Laboratory. The OJF is a closed-loop wind tunnel with an open-jet test section, featuring a hexagonal outlet of $2.85\,m \times 2.85\,m$ discharging into a $13\,m$ long and $8\,m$ high test hall [52]. Figure 4.1 shows a schematic of the facility layout. The tunnel operates over a free-stream velocity range of $3\,m/s$ to $35\,m/s$ and exhibits a low turbulence intensity of approximately 0.5%, measured about one metre downstream of the jet exit [53]. A Pitot tube located near the nozzle exit monitors the wind speed, and a high-capacity lifting platform within the test hall is available for mounting experimental hardware.

The model and auxiliary systems shown in Figure 4.2 and Figure 4.3 were supported by a rigid structural frame assembled from X-95 aluminium profiles. This frame accommodated the ground plate assembly and the water-cooled LED arrays used for particle tracking velocimetry. The airfoil was mounted vertically to simplify integration with the pitching mechanism and to enable the installation of large end-plates on either side of the model, thereby promoting quasi-two-dimensional flow by reducing tip-induced effects. The airfoil base plate, ground plate, and support frame were rigidly anchored to the tunnel floor to minimise structural compliance and vibration. A top endplate attached to the airfoil tip provided additional stiffness, ensuring accurate vertical alignment and suppressing unwanted dynamic responses, such as flutter, during operation.

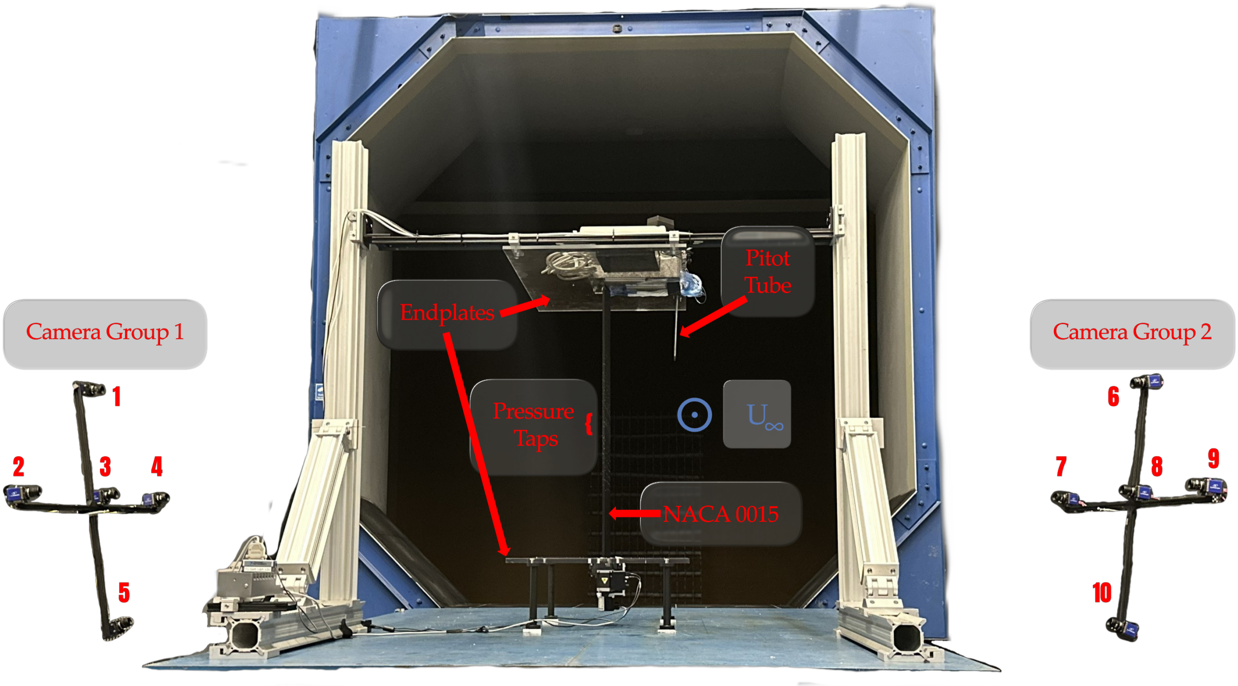

Figure 4.2: A photograph of the Experimental Setup. (Cameras to scale)

The initial constraints of the setup were:

- Maximum reduced frequency (k) of 0.2
- Flow Velocity of $15\,m/s$
- Optimum optical access for the PTV camera antennas.
- $2D$ flow (no wing-tip vortices) such that PTV and pressure tap measurements are comparable

4.1.1. Wind Tunnel

The Open Jet Facility (OJF) at TU Delft's Faculty of Aerospace Engineering is a large, low-speed open-jet wind tunnel designed for testing large-scale aerodynamic models. The tunnel features an open jet with a circular exit of approximately $2.85\,m$ in diameter, allowing for experiments with models that produce significant flow blockage. Driven by a $500\,kW$ electric motor powering a large fan with a diameter of $3.5\,m$, the OJF can achieve test-section velocities of up to $120\,km/h (\approx 33\,m/s)$. Airflow is guided through a long diffuser and two rows of corner vanes, then passes through a short diffuser and enters a settling chamber equipped with five fine-mesh screens that minimise turbulence and velocity deviations. The air is then accelerated by a contraction to form a uniform jet entering the test section. At the downstream end, the flow is cooled by a large radiator before being recirculated to the fan.

4.1.2. NACA0015 Airfoil

The NACA0015 airfoil with a chord of $200\,mm$ was selected for this study primarily because it has been extensively characterised in previous investigations conducted without ground effect, providing a reliable baseline for comparison. Moreover, the NACA four-digit series has been widely studied in both steady and unsteady aerodynamic contexts, facilitating meaningful benchmarking against existing literature. An additional advantage of the NACA0015 profile is its relatively large thickness, which provides enhanced structural rigidity and resistance to deformation under high aerodynamic and torsional loads. This geometric feature also allows for greater flexibility in mounting configurations and experimental setups. The airfoil was $3D$ printed in the faculty workshop and integrated with pressure taps at 59 locations depicted in Figure 4.4.

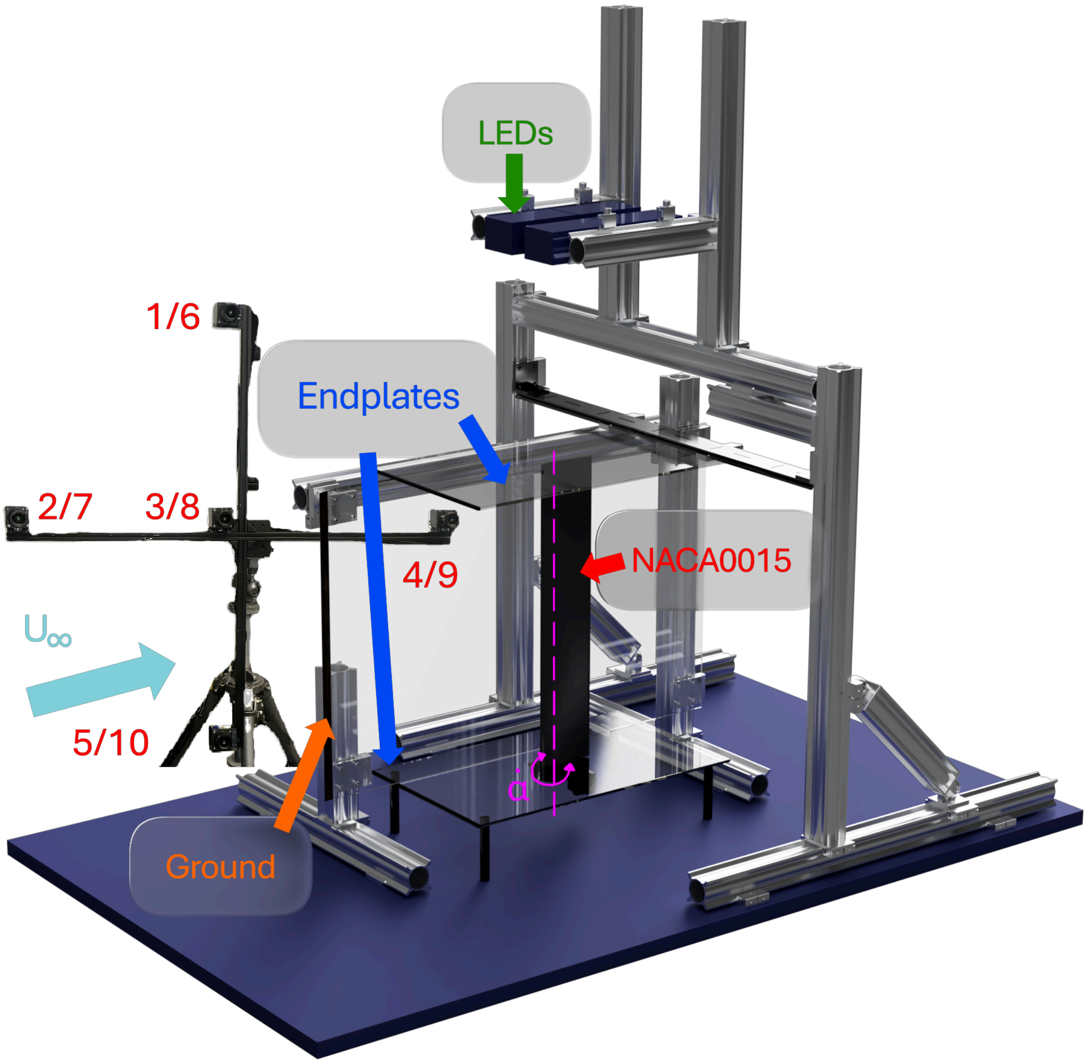

Figure 4.3: CAD render of the isometric view of the Experimental Setup. (Camera not to scale)

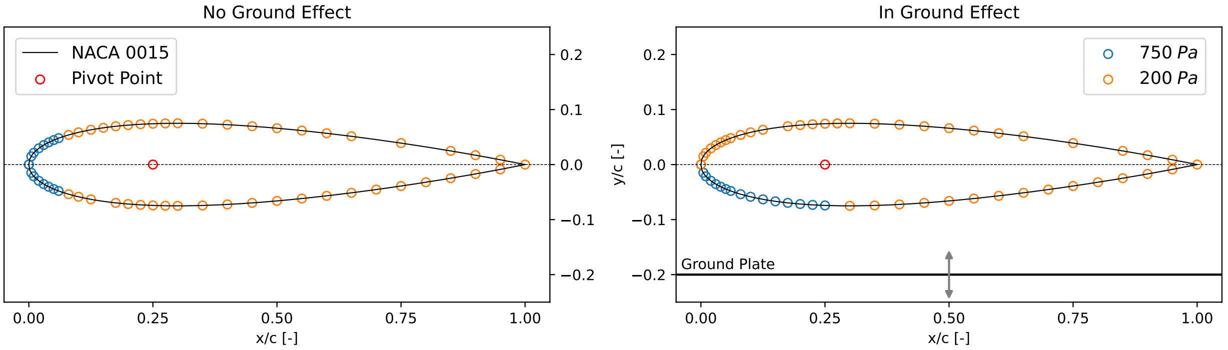

Figure 4.4: Location of the Pressure Taps.

The airfoil was $3D$-printed in the faculty workshop and equipped with surface pressure taps for both static and unsteady pressure measurements. The model was mounted between two rigid end-plates of dimensions $1000\,mm \times 600\,mm \times 10\,mm$, featuring a wedged leading edge to minimise flow separation and interference.

Two iterations of the ground plate were designed and tested. The initial configuration employed an acrylic plate of dimensions $1000\,mm \times 960\,mm \times 4\,mm$. To enhance rigidity while preserving optical transparency for the camera antennas, scrap L- and U-brackets reinforced the plate. However, during

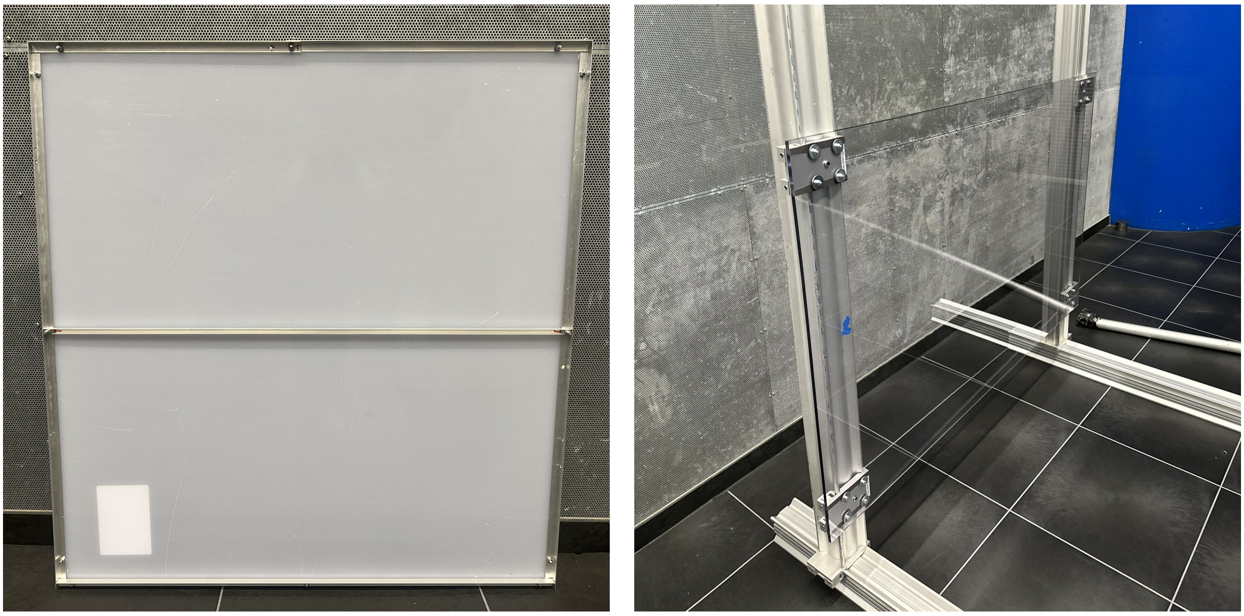

(a) (b)

Figure 4.5: Ground Plate Iterations.

preliminary tests, the acrylic plate exhibited structural instability under aerodynamic loading. Consequently, a second iteration used a polycarbonate plate of dimensions $1500\,mm \times 1000\,mm \times 10\,mm$. Several X-95 beams bolted to the wind tunnel floor supported this plate, significantly reducing aerodynamic coupling, though minor motion was still observed. Figure 4.5 shows the two versions of the ground plate.

4.2. Pitching Mechanism

The pitch axis of the airfoil is at the quarter-chord ($c/4$) with the oscillations driven by an electric motor in sinusoidal motion. A Zaber X-RSB120AT-E08 actuated the pitching mechanism. This rotary stage motor integrates a stepper motor, controller, and encoder within a single compact unit, providing high positional accuracy and ease of control. The device features a direct-drive rotary platform with a $120\,mm$ diameter and an integrated optical encoder offering 1000 counts per revolution and a polling rate of $2000\,Hz$, enabling fine angular resolution and repeatable motion. The maximum continuous speed of the actuator is $240°/s$, with a bidirectional repeatability of $\pm 0.03°$ and a maximum torque output of $3\,Nm$.

Communication and motion control were handled through Zaber's integrated controller via USB and serial interface, allowing straightforward integration with the existing Pitching Airfoil Control and Acquisition programme in LabVIEW using the manufacturer's command libraries. The motor supports both relative and absolute positioning modes, enabling precise sinusoidal pitching motion of the airfoil.

4.3. Pressure Measurements

Surface pressure taps are among the most widely used flow diagnostic techniques in wind tunnel testing. They provide local static pressure measurements along the airfoil surface, from which the pressure coefficient distribution can be determined. These distributions offer valuable insights into the aerodynamic loading and surface flow behaviour. By numerically integrating the pressure coefficient data over the chord, the overall lift and pitching moment coefficients can be derived, enabling direct comparison with theoretical predictions and unsteady force measurements obtained from other experimental methods.

The surface pressure distribution on the airfoil was measured using an array of pressure taps integrated along both the suction and pressure sides. The model contained sixty-four taps concentrated around the leading edge and mid-chord region to capture rapid pressure variations during unsteady pitching motion. Each tap was connected through short, flexible polyurethane tubing to one of four electronic pressure scanners, each featuring sixteen channels and a sampling rate of $2\,kHz$ per channel. The scanner was mounted on the top end-plate to minimise tubing length and signal lag.

All pressure signals were acquired through a National Instruments DAQ. Data acquisition and synchronisation with the pitching motion were handled manually for the IGE cases by locating the stagnation point at the initial angle of attack and observing the derivative of the de-noised signal. However, for the OGE cases, an external trigger mechanism that read the encoder from the electric motor handled the synchronisation for parallel data capture and motor control. Equation 3.2 gives the instantaneous pressure coefficients.

4.4. Particle Tomographic Velocimetry

Sufficient illumination around the airfoil is imperative for obtaining good PTV measurements. Ideally, one would want light sources on both sides of the airfoil, but that is difficult to implement in practice. Therefore, four sets of water-cooled LEDs were used over the top end-plate to achieve the required illumination.

4.4.1. Seeder

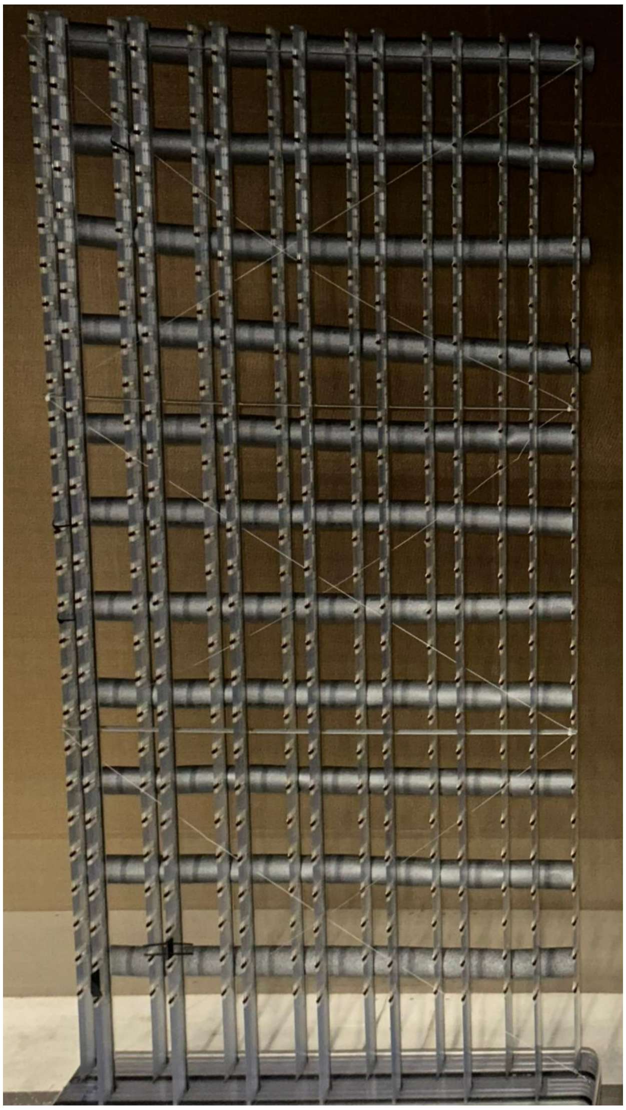

Figure 4.6: Helium-filled soap bubble generator with vortex generators to improve seeding density.

Uniform particle seeding is essential for reliable PTV measurements, as strong spatial variations in seeding density degrade correlation quality and increase measurement uncertainty. In the current setup, the helium-filled soap bubble generator exhibited partial blockage at several nozzle locations, leading to a markedly non-uniform particle distribution across the measurement volume. To mitigate this issue, additional mixing upstream of the contraction was required.

A practical solution was implemented by positioning foam cylinders downstream of the seeder. These elements generated von Kármán vortex streets, promoting large-scale turbulent mixing of the seeded flow while introducing only moderate turbulence levels. As the flow subsequently passed through the contraction, the induced turbulence intensity decayed, yielding a more homogeneous particle distribution in the test section.

4.4.2. Phase-Averaged Measurements

In unsteady, periodically forced flows, such as those encountered in oscillating airfoil experiments, the choice of averaging procedure directly influences the physical interpretation of the measured velocity fields. Two commonly employed approaches are time averaging and phase averaging, each serving a distinct purpose.

Time-averaged PTV measurements yield the mean flow field by averaging over many statistically independent realisations, thereby suppressing unsteady and turbulent fluctuations. This approach is appropriate for stationary flows but results in the loss of information associated with coherent unsteadiness. In contrast, phase-averaged measurements condition the averaging process on a reference phase of a periodic phenomenon, allowing the reconstruction of phase-resolved flow fields while retaining periodic dynamics. The principal limitations are that this approach requires a larger number of samples per phase and it inherently filters out non-periodic fluctuations [48].

4.5. Operating Conditions and Test Cases

This section outlines the experimental test matrix and the specific flow domains investigated to quantify the aerodynamic response of the NACA0015 airfoil. By systematically varying kinematic parameters and ground clearances, the test matrix isolates the coupling between unsteady motion and geometric confinement. The following subsections detail the operational boundaries for both steady and unsteady investigations, providing a structured overview of the pressure and velocimetry measurements used to characterise the transition from attached flow to the complex separation dynamics of dynamic stall.

Table 4.1: Important Parameters of the Test Matrix.

Variable	Symbol	Value	Remarks
Freestream Velocity	U_∞	$15\,m/s$	
Reynolds Number	$Re = \rho U_\infty c/\mu$	$\simeq 2 \times 10^5$	
Angle of Attack	α	-20° to 20°	Limited by the height from the ground in several cases
Mean Angle of Attack	α_o	0° $-10^\circ, -6^\circ, 6^\circ$	Attached Flow Dynamic Stall
Pitch Amplitude	$\Delta\alpha$	$5^\circ, 10^\circ$	± from mean α_o
Height to chord ratio	$H = h/c$	0.1 to ∞	Measured from hinge point ($c/4$)
Reduced Frequency	$k = \omega c/2U_\infty$	0 to 0.2	

4.5.1. Steady

Two domains of steady flow are of primary relevance to the present investigation, defined under variation of angle of attack. The first corresponds to fully attached flow at low to moderate incidence, where the lift coefficient varies approximately linearly with angle of attack and viscous effects are confined to thin boundary layers or small laminar separation bubbles. The flow is time-independent, and the aerodynamic loads are in equilibrium.

The second domain is steady stall, which occurs once the static stall angle is exceeded. In this domain, large-scale separation develops over the suction surface, leading to a reduced lift slope and increased drag. An important asymmetry arises between positive and negative stall in the presence of ground. The proximity of the ground modifies the pressure recovery and boundary-layer development on the side facing it. For negative angles of attack, this often leads to a later or more gradual stall compared with the positive angles of attack case.

Table 4.2: Matrix of Steady Test cases.

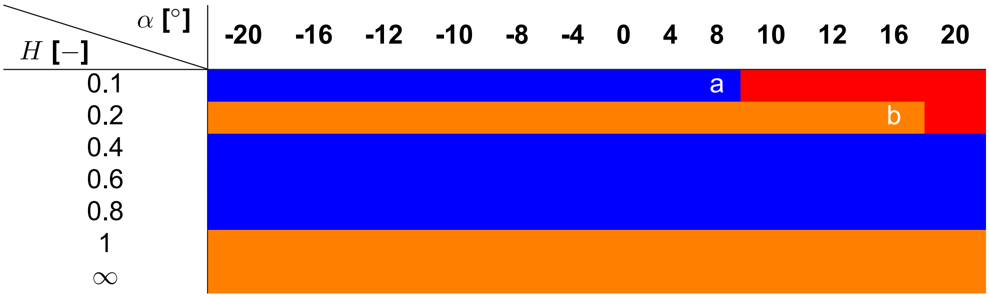

H [−] \ α [°]	-20	-16	-12	-10	-8	-4	0	4	8	10	12	16	20
0.1	🟦	🟦	🟦	🟦	🟦	🟦	🟦	🟦	🟦 a	🟥	🟥	🟥	🟥
0.2	🟧	🟧	🟧	🟧	🟧	🟧	🟧	🟧	🟧	🟧	🟧	🟧 b	🟥
0.4	🟦	🟦	🟦	🟦	🟦	🟦	🟦	🟦	🟦	🟦	🟦	🟦	🟦
0.6	🟦	🟦	🟦	🟦	🟦	🟦	🟦	🟦	🟦	🟦	🟦	🟦	🟦
0.8	🟦	🟦	🟦	🟦	🟦	🟦	🟦	🟦	🟦	🟦	🟦	🟦	🟦
1	🟧	🟧	🟧	🟧	🟧	🟧	🟧	🟧	🟧	🟧	🟧	🟧	🟧
∞	🟧	🟧	🟧	🟧	🟧	🟧	🟧	🟧	🟧	🟧	🟧	🟧	🟧

Legend: 🟦 Pressure 🟧 Pressure and PTV 🟥 No measurement

[a] $7°$ due to physical limitations

[b] $15°$ due to physical limitations

4.5.2. Unsteady

Two domains of unsteady flow are of primary interest. The first corresponds to the attached-flow region, bounded by the static stall angles on both sides of the $C_\ell - \alpha$ curve. Within this range, lift and moment vary approximately sinusoidally with instantaneous incidence, and flow separation is limited to small laminar bubbles or trailing-edge vortices. The second domain is that of dynamic stall, which occurs when the airfoil is rapidly pitched beyond the static stall angle, leading to the formation and convection of a leading-edge vortex. This process results in a delayed but abrupt loss of lift and a pronounced hysteresis loop in the $C_\ell - \alpha$ relationship. These two domains define the operational boundaries of the present experiments, with the focus on characterising unsteady aerodynamic effects within the attached-flow domain prior to dynamic stall.

Table 4.3: Matrix of Unsteady Test Cases.

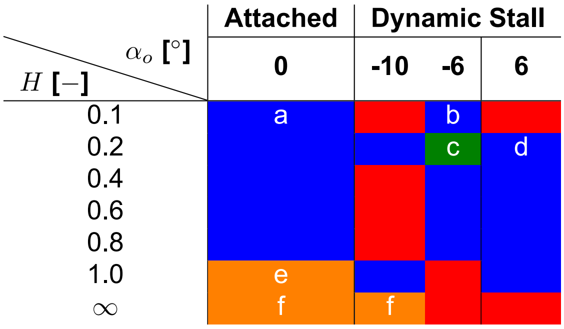

	Attached	Dynamic Stall		
H [−] \ α_o [°]	0	-10	-6	6
0.1	🟦 a	🟥	🟦 b	🟥
0.2	🟦	🟦	🟩 c	🟦 d
0.4	🟦	🟥	🟦	🟦
0.6	🟦	🟥	🟦	🟦
0.8	🟦	🟥	🟦	🟦
1.0	🟧 e	🟦	🟥	🟦
∞	🟧 f	🟧 f	🟥	🟥

Legend: 🟦 Pressure[g] 🟧 Pressure and PTV 🟩 PTV 🟥 No measurement

[a] $\Delta\alpha = 6°$ due to physical limitations (All other cases $\Delta\alpha = 10°$).

[b] $\alpha_o = -4°$ due to physical limitations.

[c] PTV performed at this condition only for $k = 0.2$.

[d] $\alpha_o = 5°$ due to physical limitations.

[e] PTV performed at this condition only for $k = [0.05, 0.20]$.

[f] PTV performed at this condition only for $k = 0.1$.

[g] $k = [0.05, 0.10, 0.15, 0.20]$ for all pressure cases.

Saved

5

Data Processing

This chapter details the methodology employed to transform raw experimental data into a format suitable for aerodynamic analysis. The study utilised two distinct measurement techniques; consequently, the chapter divides into two primary sections. The first section addresses the processing of surface pressure data, and the second section discusses the post-processing of the PTV measurements.

5.1. Pressure

This section documents the assumptions and pragmatic corrections implemented within the analysis scripts used to derive sectional force coefficients from the pressure-tap measurements on the NACA0015 airfoil, both out of ground effect (OGE) and in ground effect (IGE).

5.1.1. Corrections

Raw pressure time-series data are first de-biased by subtracting tare measurements acquired at zero freestream velocity ($U_\infty = 0$). This procedure eliminates static offsets inherent in the scanners and the tubing manifold before calculating non-dimensional coefficients. The dynamic pressure used for normalisation is reconstructed from a pitot-static tube located within the test section, determined as the ensemble mean of the raw data, rather than relying on the wind tunnel's nominal set-point.

To ensure agreement with numerical predictions from XFOIL at $H \to \infty$, several scanner-specific calibrations were applied. A gain of 1.03 and a static offset of $+15\,Pa$ were assigned to channels associated with scanner 1. Additional offsets of $+20\,Pa$ and $-15\,Pa$ were applied to scanner 2 and scanner 3, respectively. Furthermore, for all negative angles of attack tested at $H \to \infty$, the effective angle α was increased by $0.8°$. This adjustment accounts for a mechanical misalignment identified in a post-campaign inspection and ensures consistency with the steady-state aerodynamic theory presented in section 2.1.

For cases involving finite ground clearance ($H \ll \infty$), as illustrated in Figure 5.2, the processing routine enforces inter-dataset consistency by borrowing a reference C_P distribution from a corresponding $H \to \infty$ case when $\alpha > 4°$. Specifically, the corrected $OGE\ C_P$ distribution is aligned to the current case via a scalar offset ΔC_P, calculated at a reference tap (index 15 on the upper surface). This operation replaces the first 15 suction-surface taps of the IGE dataset with the reference-aligned $H \to \infty$ values. This correction was necessitated by the saturation of the leading edge suction-side taps, which reached their measurement saturation limit of approximately $200\,Pa$.

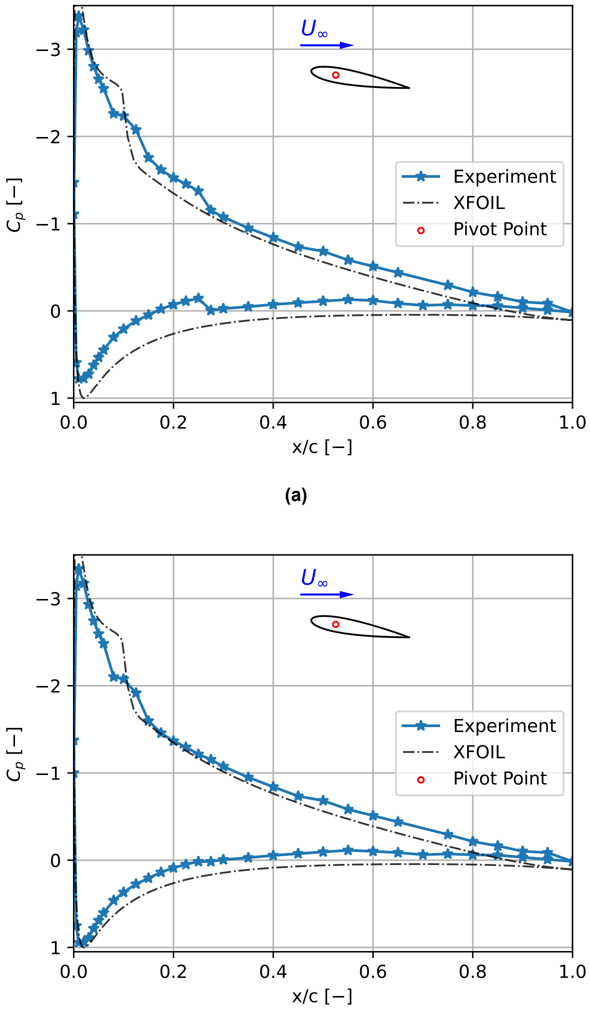

(a)

(b)

Figure 5.1: Coefficient of Pressure at $H \to \infty$ (a) before corrections; (b) after corrections.

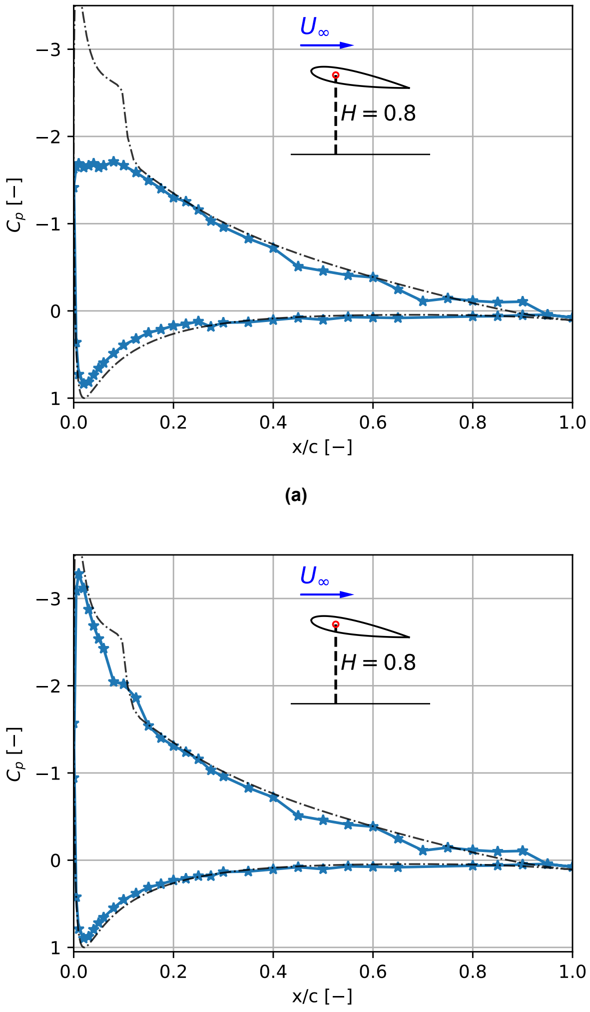

(a)

(b)

Figure 5.2: Coefficient of Pressure at $\alpha = 10^\circ$ and $H = 0.8$ (a) before corrections; (b) after corrections.

5.1.2. Blocked Taps

A subset of pressure taps was flagged as blocked or unreliable during the post-manufacturing quality check. As detailed in Appendix A, these specific ports were repurposed to monitor total pressure (P_0), freestream static pressure (P_∞), and a reference static pressure (P_{ref}) external to the wind tunnel flow. The C_P values at these airfoil locations are either reconstructed via linear interpolation of the immediate neighbouring taps or have been masked to avoid erroneous values.

5.1.3. Force Calculation using Surface Pressure Integrations

The NACA0015 profile coordinates are modelled using two cubic splines for the upper and lower surfaces. The geometric slope, dy/dx, at each tap location is evaluated analytically from the spline derivatives. This method provides a smooth estimate of the surface inclination necessary for axial-force projection.

Integrating the pressure distributions over the chord using Equation 5.1 and Equation 5.2 yields the sectional force coefficients (normal, C_n, and axial, C_a).

$$C_n = \int_0^1 \left(C_{P_\ell} - C_{P_u}\right) dx \tag{5.1}$$

$$C_a = \int_0^1 \left(C_{P_u}\frac{dy_u}{dx} - C_{P_\ell}\frac{dy_\ell}{dx}\right) dx \tag{5.2}$$

These coefficients can be resolved vectorially into lift and drag components as

$$C_\ell = C_n \cos\alpha - C_a \sin\alpha \tag{5.3}$$

$$C_d = C_n \sin\alpha + C_a \cos\alpha \tag{5.4}$$

Note that at low Reynolds numbers, skin friction contributes significantly to the total drag. Since Equation 5.4 only accounts for the pressure-drag component, certain configurations may yield a negative C_d.

5.2. Three-Dimensional Particle Tracking Velocimetry

This section describes the image processing pipeline and the algorithmic framework used to derive a volumetric velocity field from the $3D - PTV$ snapshots captured on the NACA0015.

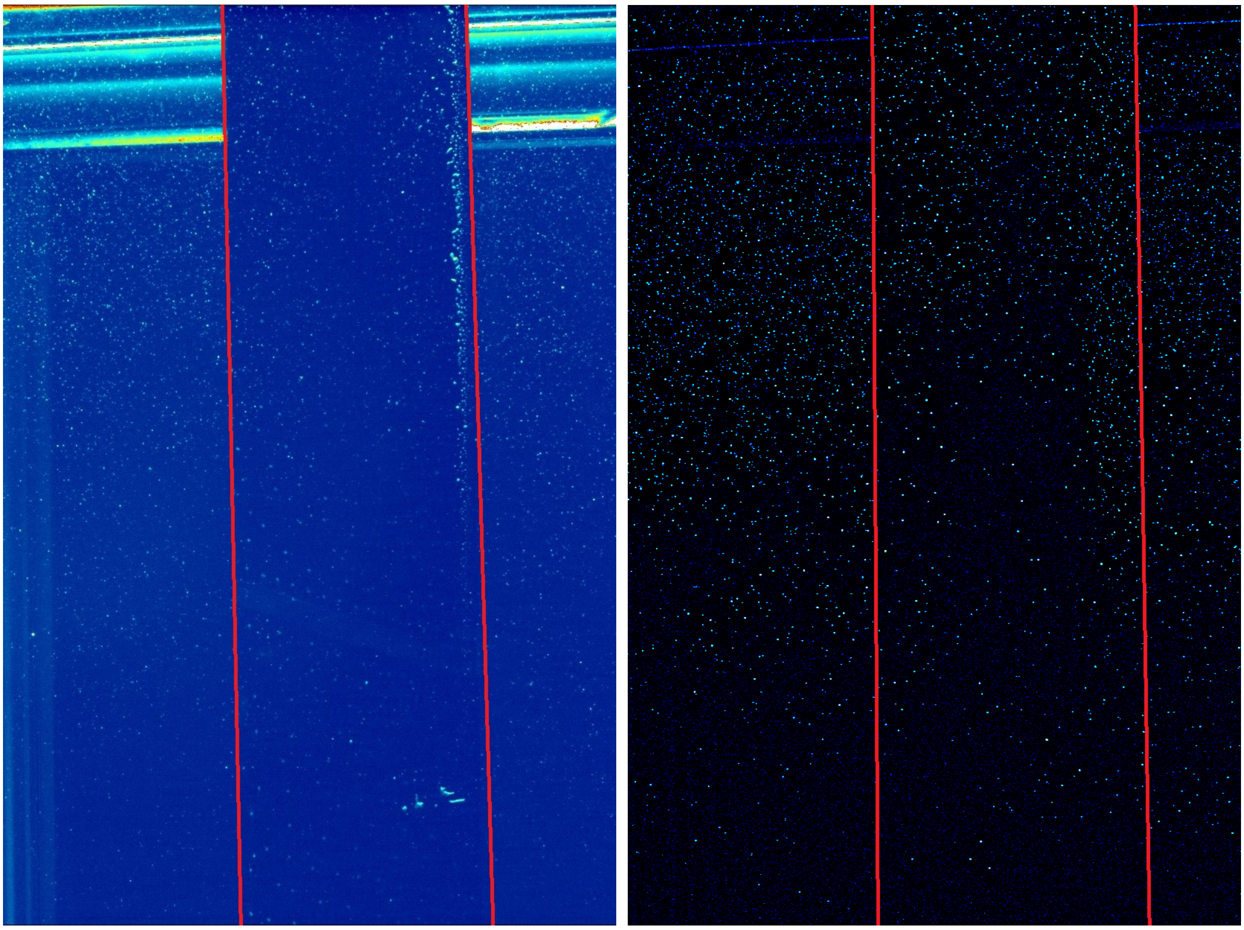

Figure 5.3: Raw (Left) and Processed (Right) Images from Camera 1. The airfoil is located between the red lines.

The left pane of Figure 5.3 displays a raw image representing a sub-section of the flow field. To isolate the seeding particles from the background, several image enhancement algorithms are applied. First, a temporal minimum subtraction (with a filter length of 11 frames) eliminates stationary, high-intensity artefacts, such as reflections from the airfoil surface. Subsequently, a sliding minimum subtraction and local average normalisation (using a kernel of eleven pixels) are employed to enhance the particle-to-background contrast.

To compensate for fluctuations in LED intensity, all frames are normalised against the initial image in the sequence. The resulting pre-processed images, as shown in the right pane of Figure 5.3, contain isolated particle signatures suitable for the Shake-The-Box (STB) Lagrangian particle tracking algorithm (refer to section 3.3). The resulting $3D$ velocity fields are subsequently span-averaged in the region away from the endplates to generate a representative $2D$ flow field for the airfoil section.

6

Results

This chapter presents the experimental results obtained from the steady and unsteady pitching tests of a NACA0015 airfoil in ground effect. Surface pressure taps measured the aerodynamic loads, while $3D$ particle tracking velocimetry ($3D-PTV$) characterised the near-wake and wall-bounded flow structures. The results are presented in terms of time-averaged and phase-averaged aerodynamic coefficients, unsteady lift hysteresis, and near-wall vortex dynamics.

6.1. Data Validation

Before interpreting the experimental results, the study validated the pressure-based aerodynamic coefficients against theoretical and numerical reference solutions. The objective of this comparison is twofold: first, to verify the integrity of the measurements in free-air conditions, and second, to assess how non-dimensionalised height ($H = h/c$) modifies the lift characteristics relative to inviscid and semi-empirical predictions. For the out of ground effect (OGE, $H \to \infty$) case, the measured lift curve $C_\ell - \alpha$ was compared to thin–airfoil theory (TAT) and to steady solutions from XFOIL and JavaFoil. For the in ground effect (IGE, $H \ll \infty$) case, the lift behaviour is compared with Equation 2.3 and solutions from JavaFoil [18, 54, 55].

The XFOIL and JavaFoil computations used the same NACA0015 geometry and Reynolds number as in the experiments. Both tools are based on inviscid, potential-flow formulations (panel or vortex methods) coupled with integral boundary-layer solvers, rather than on a direct solution of the Navier–Stokes equations. Viscous effects are accounted for using boundary-layer theory and semi-empirical closure models, including linear stability analysis for transition prediction and simplified criteria for laminar separation bubbles and incipient separation. As a result, these methods do not fully resolve viscous flow fields. However, they can provide reasonably accurate predictions of sectional lift and drag in attached-flow domains at low to moderate angles of attack.

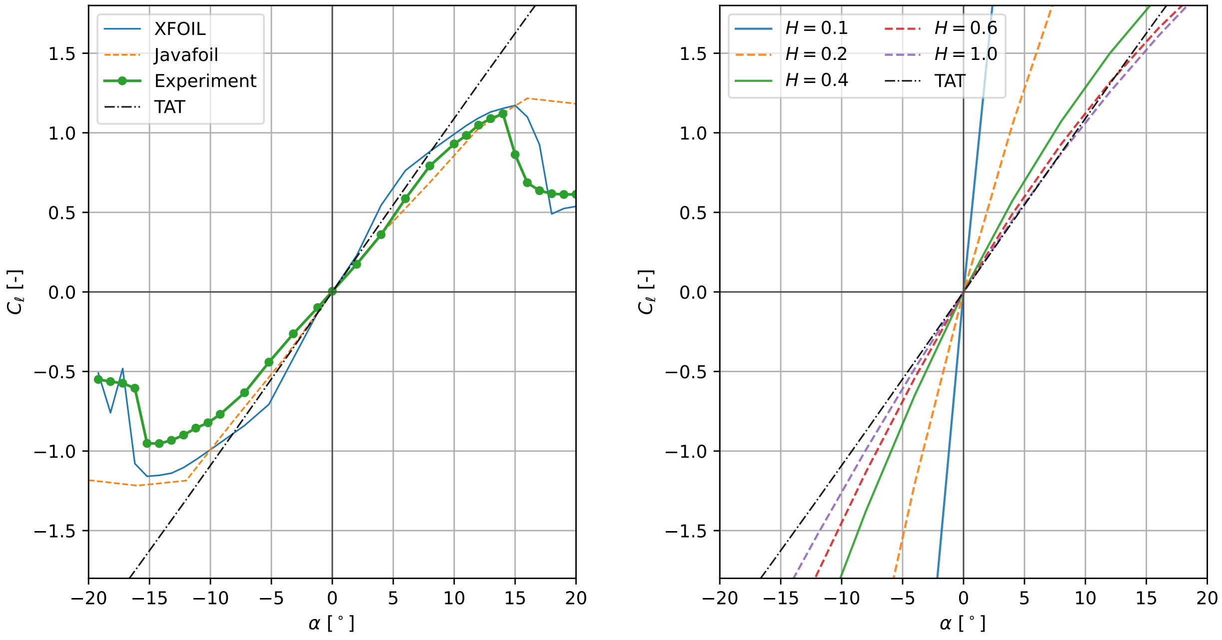

(a) OGE Comparison

(b) Potential Flow (Equation 2.3) [17]

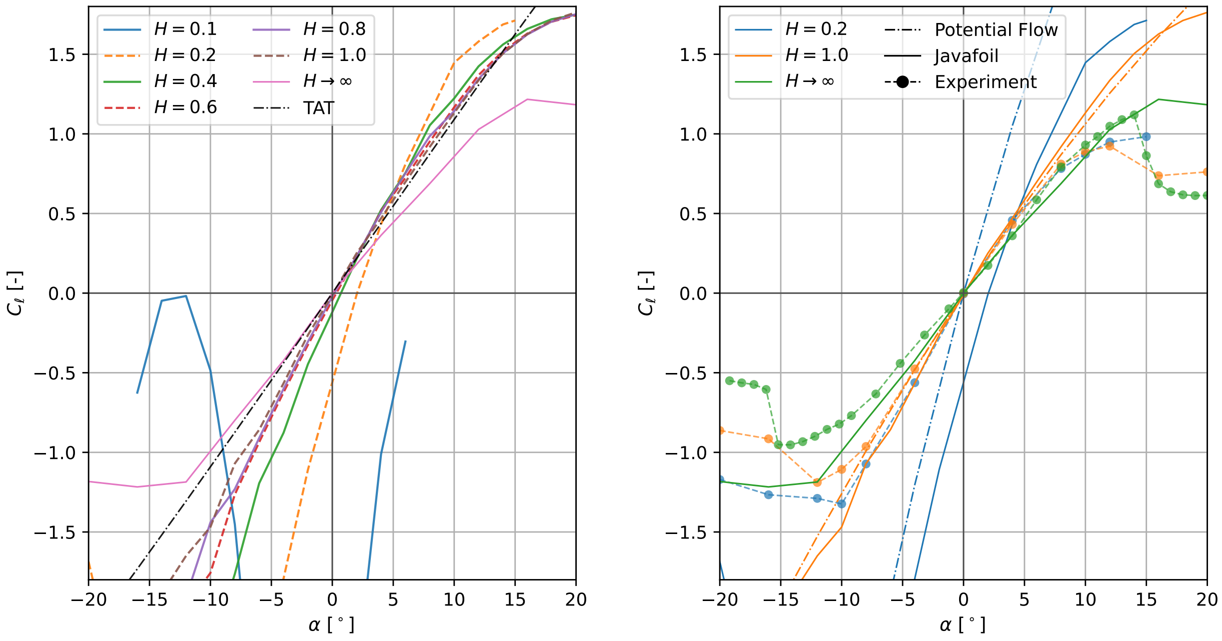

(c) JavaFoil

(d) IGE Comparison

Figure 6.1: Validation of sectional lift coefficients (C_ℓ) against analytical and numerical models.

Figure 6.1a compares OGE results from XFOIL, JavaFoil and results obtained during this project. In the linear domain, all methods collapse closely onto each other. TAT remains linear by construction. JavaFoil and XFOIL predict stall; however, the onset is gradual for JavaFoil. The experimental data follow the same overall trend but exhibit earlier lift reduction, attributable to finite-span effects and residual three-dimensionality in the wind tunnel configuration. The agreement in slope and zero-lift angle confirms that the measurement chain reliably reproduces canonical free-air behaviour.

Having established the free-air baseline, ground-effect amplification is examined through analytical and numerical models, in Figure 6.1b, the lift coefficient predicted from the analytical potential-flow ground-effect formulation (Equation 2.3) is shown for $H = 0.1$ to 1.0, together with TAT being the limit as $H \to \infty$. As expected, decreasing ground clearance increases the lift-curve slope. The $H = 0.1$ case exhibits an extremely steep gradient. This behaviour arises from the image-vortex formulation inherent in potential-flow theory (see section 2.1), which reduces induced downwash and increases the effective angle of attack as the wall is approached. Because viscous effects and separation are absent in this framework, there is no mechanism to limit circulation growth. Consequently, the model predicts no stall and yields $C_\ell \to \infty$ as $H \to 0$. As H increases, the curves approach the TAT line asymptotically.

Figure 6.1c shows the corresponding JavaFoil predictions. For moderate heights ($H \geq 0.4$), the lift curves remain approximately linear up to $|\alpha| \leq 10°$, with slopes closely aligned with TAT. At $H = 0.1$, the solver predicts an unrealistic $C_{\ell,min} = -3.383$ at $\alpha = 0°$ and $C_{\ell,max} = 0$ at $\alpha = -12°$.

This deviation suggests that the boundary-layer model becomes unreliable at very small heights, where strong pressure gradients and confinement effects challenge the semi-empirical closure assumptions. Compared with Figure 6.1b, JavaFoil predicts a more gradual slope amplification and finite stall at higher $|\alpha|$, reflecting the inclusion of viscous effects in the model. It is also observed that negative angles of attack exhibit stronger lift modulation as H decreases, indicating asymmetric pressure redistribution as the pressure side approaches the wall.

Figure 6.1d focuses on selected finite heights ($H \simeq 0.2$, 1.0 and ∞), directly comparing Potential Flow, JavaFoil and experimental data. At $H = 1.0$, the behaviour closely resembles the OGE results. At $H \simeq 0.2$, the lift-curve slope increases substantially. The experimental curve displays earlier stall and lower peak lift than JavaFoil, suggesting enhanced viscous, $3D$ or confinement effects.

Table 6.1: $dC_\ell/d\alpha$ for a few selected heights.

H	Method	$dC_\ell/d\alpha$	$C_{\ell,max}$	$C_{\ell,min}$
0.2	Potential	16.135	3.285	-7.737
	JavaFoil	15.771	1.712	-4.144
	Experiment	7.294	0.966	-1.340
0.6	Potential	7.373	1.953	-3.178
	JavaFoil	7.907	1.745	-2.360
	Experiment	6.323	0.863	-1.292
1.0	Potential	6.672	1.932	-2.666
	JavaFoil	7.363	1.763	-2.132
	Experiment	6.494	0.906	-1.204
∞	TAT	6.283	2.149	-2.149
	XFOIL	7.651	1.172	-1.159
	JavaFoil	5.629	1.217	-1.217
	Experiment	4.959	1.119	-0.953

The quantification of lift-curve slope amplification across various modelling approaches, as detailed in Table 6.1, reveals that potential-flow predictions exhibit the strongest sensitivity to dimensionless height H, predicting an asymptotic growth in lift as $H \to 0$. While JavaFoil moderates this amplification by introducing viscous corrections and finite stall behaviour, it still tends to over-predict experimental trends at small heights. In contrast, the experimental slopes remain consistently lower and bounded; this discrepancy, illustrated in Figure 6.1, highlights the influence of finite-span effects, viscous diffusion, and the complex interaction between the airfoil and ground-plane boundary layers—factors which fundamentally limit circulation growth and are not fully captured by idealised or two-dimensional numerical models.

6.2. Steady Aerodynamics

This section presents the steady aerodynamic characteristics of the NACA0015 airfoil in and out of ground effect, based on time-averaged surface-pressure distributions obtained from surface taps. From these pressure distributions, the sectional lift coefficient C_ℓ is obtained by integrating the pressure difference between suction and pressure sides along the chord using Equation 5.1-Equation 5.4. The analysis proceeds from representative OGE cases, which serve as the reference condition, to selected IGE conditions that exhibit strong pressure-side blockage at high angles. Subsequently, the lift coefficient is examined as a function of both angle of attack and non-dimensional ground clearance, culminating in a two-parameter contour map of $C_\ell\,(\alpha,\,H)$ that summarises the steady ground-effect behaviour.

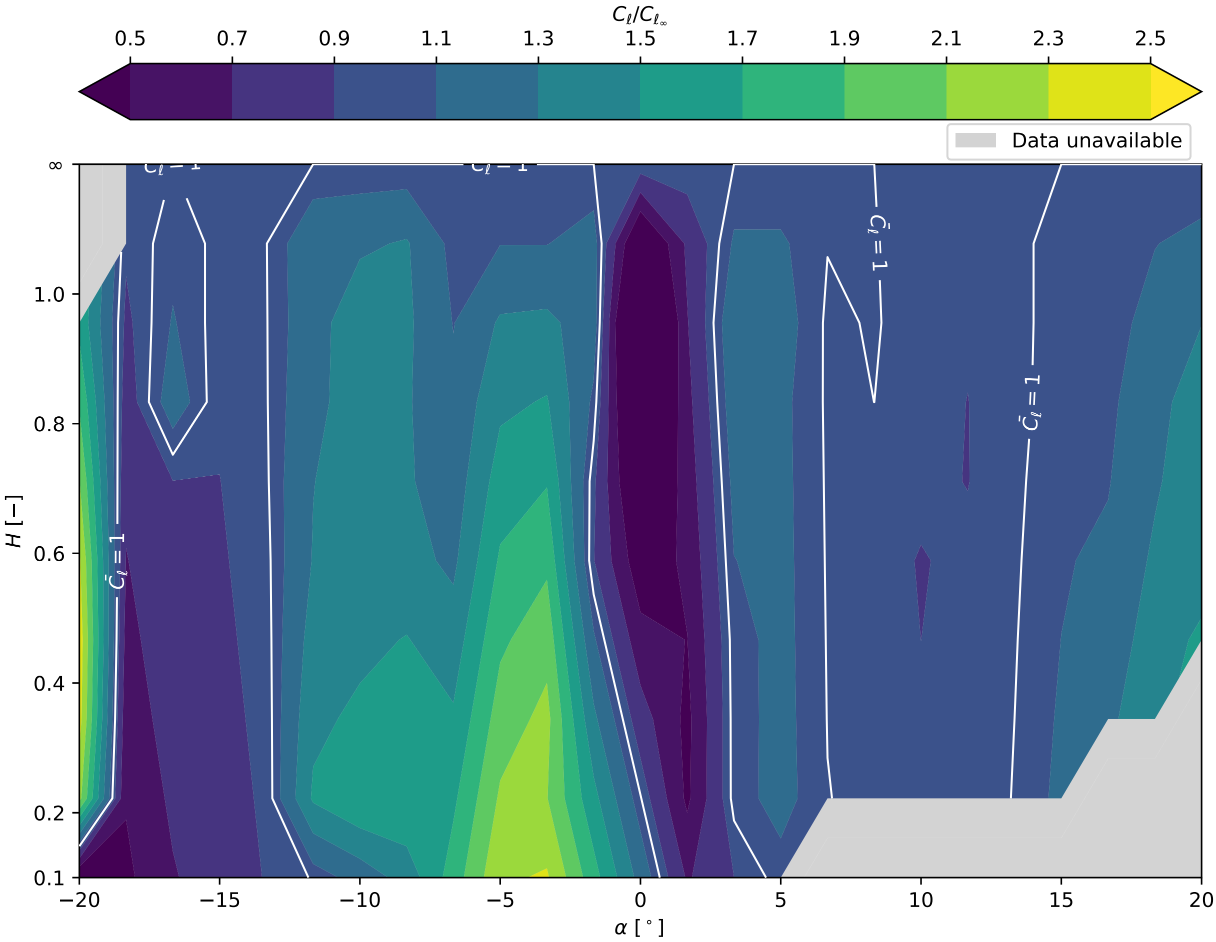

Figure 6.2: Contour map of the steady normalised lift coefficient ($\bar{C}_\ell = C_\ell/C_{\ell,H\to\infty}$) as a function of α and H. The white contour lines indicate where $\bar{C}_\ell = 1$, while grey areas denote combinations where data is unavailable.

Figure 6.2 provides an overview of how the normalised lift coefficient $\bar{C}_\ell = C_\ell/C_{\ell_\infty}$ varies across the $\alpha - H$ plane. Regions where $\bar{C}_\ell > 1$ correspond to configurations in which ground-effect enhances lift relative to the OGE case, whereas $\bar{C}_\ell < 1$ denotes a reduction. It is immediately evident that $\bar{C}_\ell$ does not increase monotonically as the airfoil approaches the ground. Instead, there exist bands at pre-stall positive angles of attack where $\bar{C}_\ell < 1$, even though an increase in lift would be expected from classical ground-effect arguments discussed in section 2.2.

This counter-intuitive behaviour is a consequence of limitations in the pressure transducers on the suction side, which saturate at a maximum measurable pressure difference of approximately $200\,Pa$ at higher positive angles. Saturation occurs for all IGE cases, as discussed in section 5.1 and Figure 5.2. As a result, the most negative suction peaks are clipped, leading to an underestimation of the suction-side contribution to C_ℓ and, hence, an artificially low $\bar{C}_\ell$. To mitigate this bias, the suction-side pressure for the first eight affected channels was replaced by the corresponding OGE data at $H \to \infty$, as illustrated in Figure 5.2b and marked with an ellipse. This correction partially restores the expected trend, as shown in Figure 6.3. Nevertheless, some measurement deficit remains. Most $\bar{C}_\ell < 1$ regions in Figure 6.2 are likely higher in reality and should be interpreted as conservative values.

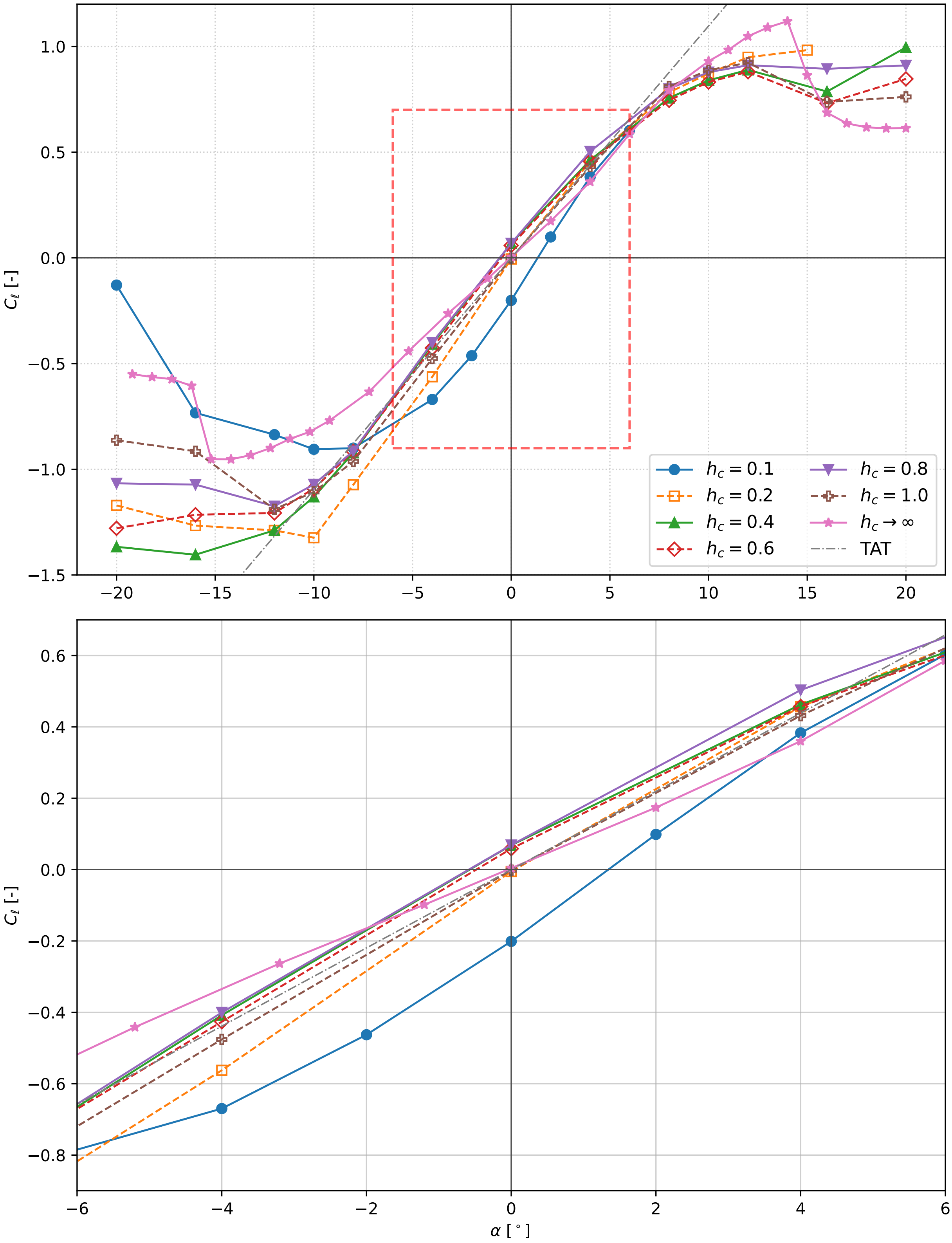

Figure 6.3: C_ℓ vs α for all tested ground heights: (top) full range of α; (bottom) Magnified view of the highlighted region, $-6 \leq \alpha \leq 6$.

To support the findings of Figure 6.2, a more detailed quantitative comparison is provided via Figure 6.3–Figure 6.15 below. The flow physics at these critical angles are examined in detail in section 6.3.

Figure 6.3 shows the variation of C_ℓ with α for all non-dimensional heights tested. The measured lift curves show close agreement with TAT and the $H = 1$ case within the linear lift region, with the OGE case having a lower slope due to viscous and $3D$ effects. For all IGE cases, the lift-curve slope is consistently higher in the linear domain when compared with OGE, reflecting the classical ground-effect mechanism whereby the presence of the ground reduces downwash and increases circulation.

At positive angles of attack beyond approximately $10°$, the expected increase in C_ℓ for decreasing H is not fully captured, primarily because pressure transducer saturation limits the measurable suction peaks on the airfoil surface. Despite this limitation, the finite-height cases in positive stall still exhibit higher lift coefficients than OGE, indicating that the ground continues to augment lift even when the flow is largely separated. At moderate angles, each H yields a nearly linear lift curve with a slope close to the free-air value, but with a systematic shift in C_ℓ as the airfoil approaches the ground. At small positive α, the lowest heights produce negative lift, consistent with the downforce-generating Venturi behaviour discussed earlier. As α increases further, intermediate heights $(0.1 < H \leq 0.4)$ show more rapid lift growth than OGE, reflecting the beneficial ground-effect contribution before blockage becomes dominant. At still higher positive angles, close to stall, the curves for the smallest H flatten or even decrease, indicating that the combined effects of boundary-layer thickening and choking outweigh the idealised inviscid ground-effect gain. At negative angles of attack, stall onset appears to occur at a smaller magnitude of α compared to OGE.

Nevertheless, the absolute value of C_ℓ remains higher for the finite H cases, and the post-stall reduction in lift is generally less pronounced. An exception occurs at $H = 0.1$, where a sharper drop in C_ℓ is observed; the more gradual lift decay at other heights is likely associated with flow choking and strong confinement effects in the gap between the airfoil and the ground, which limit the mass flow. The zoomed-in view in Figure 6.3 highlights the subtle differences in slope and values between the various heights.

Overall, decreasing ground clearance results in a clear increase in lift magnitude within the linear domain, consistent with ground-effect theory. In contrast, in the post-stall regions, the aerodynamic behaviour is increasingly governed by viscous effects, flow separation, and blockage within the airfoil–ground gap, rather than by classical circulation-based lift augmentation alone.

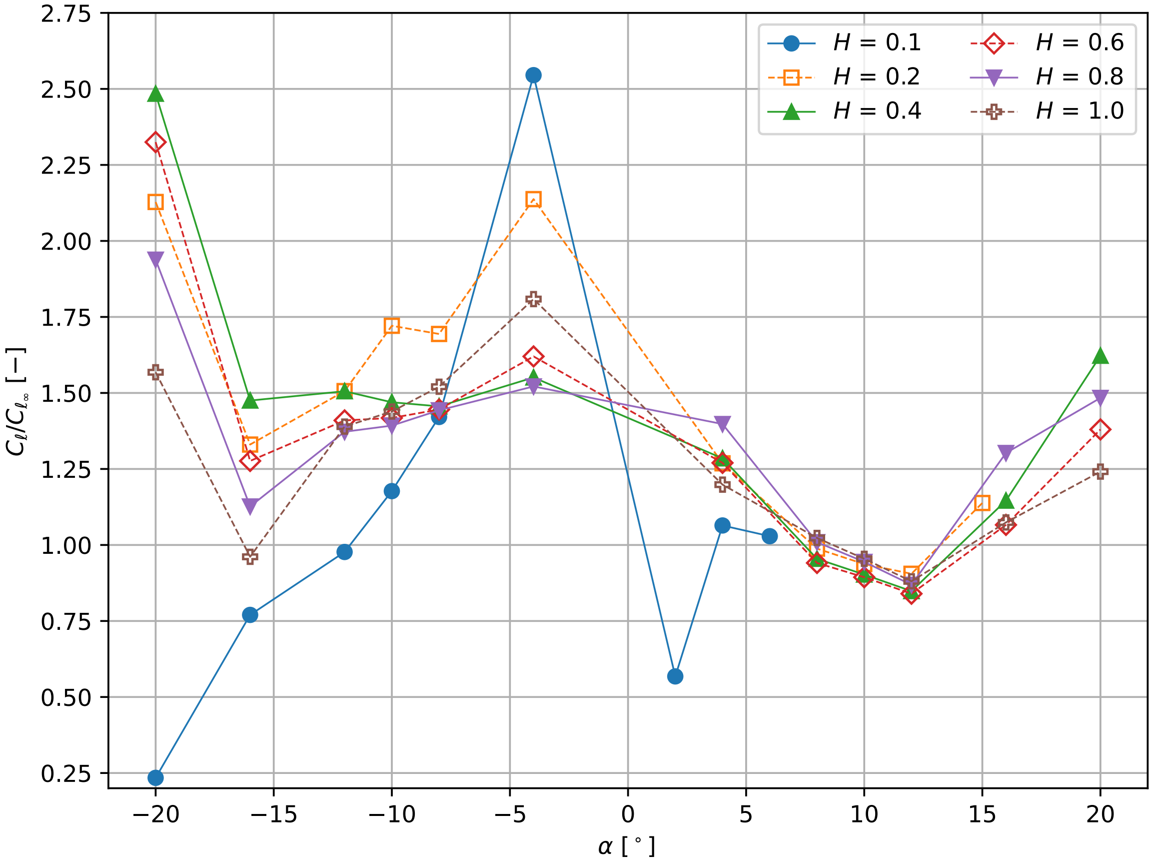

Figure 6.4: $\bar{C}_\ell = C_\ell/C_{\ell_\infty}$ vs α for various H.

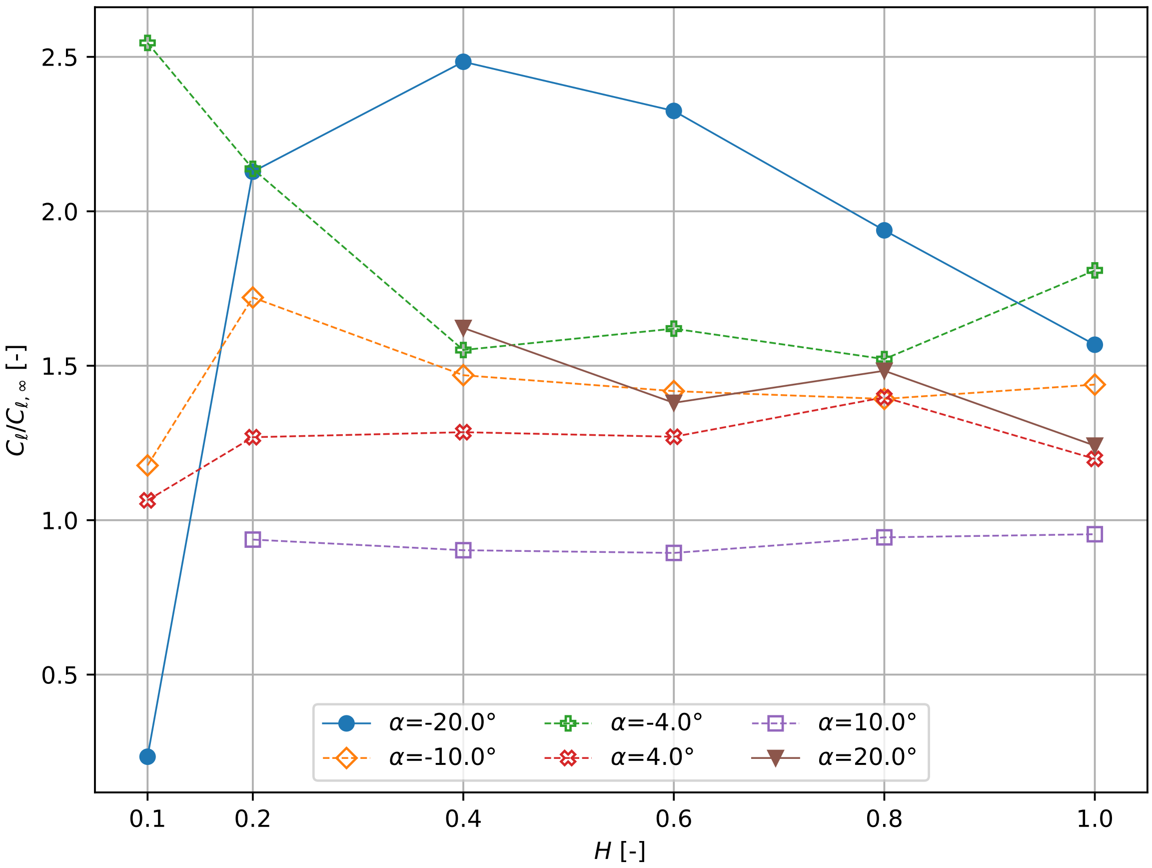

Figure 6.5: $\bar{C}_\ell = C_\ell/C_{\ell_\infty}$ vs H for selected α.

Figure 6.4 and Figure 6.5 provide complementary perspectives of the normalised lift, $\bar{C}_\ell = C_\ell/C_{\ell,H\to\infty}$, as a function of α and H. It is evident that the relative lift enhancement at a fixed H is highly dependent on the angle of attack; this sensitivity is most pronounced near the onset of stall, where the flow field is particularly susceptible to modifications in the pressure gradient and separation point. For the majority of the angles tested, C_ℓ exhibits a distinct peak at an intermediate height, typically within the range $0.2 < H \leq 0.4$. Beyond this critical proximity, the absolute lift begins to diminish as the airfoil is brought closer to the ground. While this trend is consistent with the experimental observations in Figure 6.2, it deviates from the monotonic increase predicted by the inviscid theory in Figure 2.3 due to the presence of real-world viscous effects. The normalised curves in Figure 6.5 further emphasise that ground-effect serves to amplify lift relative to the OGE condition until this critical height is reached. Below this threshold, the simultaneous growth of the boundary layers on the airfoil pressure side and the ground plane significantly constricts the effective flow area. These associated viscous losses and the resulting flow blockage eventually offset the benefits of ground-induced pressure redistribution, leading to the observed reduction in performance. By $H = 1$, the flow field effectively tends to OGE conditions; beyond this threshold, the aerodynamic behaviour is assumed to asymptotically approach the $H \to \infty$ limit, with negligible further influence from the ground plane.

6.3. Steady Flow Physics

One can interpret these pressure-based trends by examining the corresponding steady velocity and vorticity fields obtained from the $3D - PTV$ measurements. In the section below, the surface-pressure distributions and the PTV fields are discussed together at matching angles of attack, so that changes in suction/pressure loading can be linked directly to separation, boundary-layer growth, and wake development observed in the flow field. The discussion is organised by flow domain, progressing from negative stall through to positive stall.

6.3.1. Negative Stall

In negative stall, the C_P overlays quantify how suction-side separation and pressure recovery vary with H. At the same time, the PTV fields reveal the spatial distribution of low-momentum regions, vorticity concentrations, and wake thickening. The interpretation below focuses on $\alpha = -20°$ as a representative case.

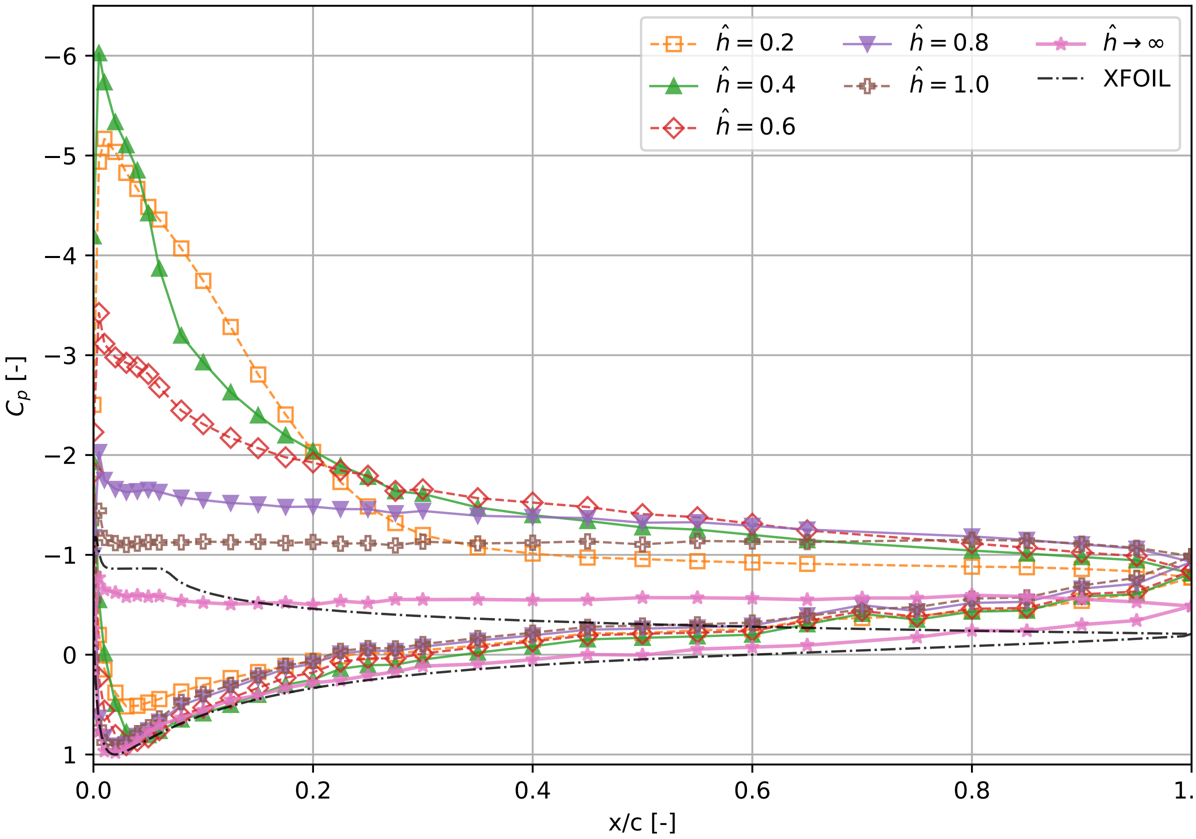

Figure 6.6: C_P at α = $-20°$ at all H tested.

In Figure 6.6, the OGE condition is characterised by extensive suction-side separation and a significant reduction in lift. Introducing the ground partially recovers lift relative to OGE. This recovery arises primarily from a reduction and downstream displacement of the suction-side separated region, driven by streamline confinement and pressure redistribution within the gap. The pressure side remains comparatively insensitive to H. Thus, even in a negative stall, ground proximity can either enhance or degrade performance depending on the degree of confinement. Notably, $C_P \neq 1 \ \forall \ x/c$, the flow never reaches stagnation, which indicates the interaction of the boundary layers from the airfoil and the ground.

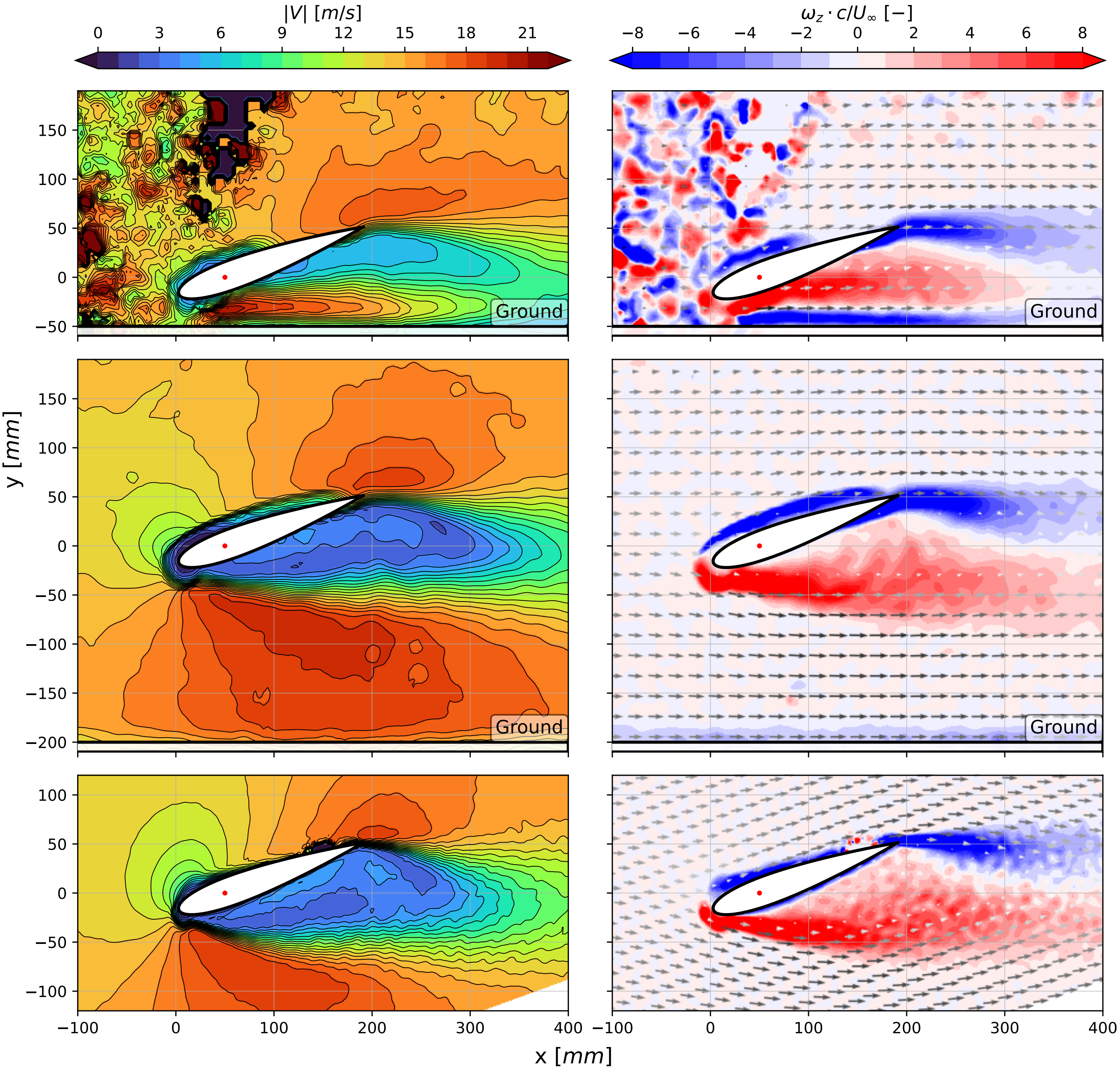

Figure 6.7: (left) Absolute velocity magnitude $|V|$. (right) Non-dimensional vorticity $\omega_z c/U_\infty$ ($\omega_z = dv/dx - du/dy$). For $\alpha = -20°$. Panels: (top) $H \simeq 0.2$; (mid) 1.0; (bot) ∞.

The velocity and vorticity fields at $\alpha = -20°$ in Figure 6.7 clarify the role of H in negative stall. At $H \simeq 0.2$, the suction-side separated region is compressed and displaced downstream, and the wake is correspondingly thinner and shorter. Relative to $H = 1$ and $H \to \infty$, the flow remains attached over a larger fraction of the chord before separating, indicating a delayed separation point and a reduced loss of suction-side loading. The strong interaction between the airfoil and ground boundary layers is also evident in the top-right frame of Figure 6.7, where near-wall vorticity intensifies after the restricted gap. This boundary-layer interaction modifies the near-field pressure environment by weakening the effective adverse pressure gradient on the suction side, thereby sustaining a higher mean circulation around the section.

At $H = 1$, the flow more closely resembles classical stall: separation initiates near the leading edge, the separated shear layer expands, and the wake broadens with weak pressure recovery. Importantly, even at the smallest H, the flow does not reattach; rather, the vorticity field indicates that ground proximity constrains the separated region and limits its growth. This confinement-induced compression of the separated zone maintains higher mean circulation than in the OGE case and provides the physical basis for the partial recovery of lift measured at low H.

The $\alpha = -20°$ case demonstrates that the primary influence of the ground in negative stall is the suppression, displacement, and confinement of the suction-side separated region present in OGE. The resulting reduction in the extent of the separated wake is consistent with the higher measured force levels at low H. It explains the systematic mitigation of stall in C_ℓ observed across this domain in Figure 6.3 and Figure 6.5.

6.3.2. Attached Flow

At these angles, the flow remains fully attached to both surfaces. This domain highlights the transition from Venturi-effect-driven downforce at low angles to viscous blockage as the effective angle of attack increases.

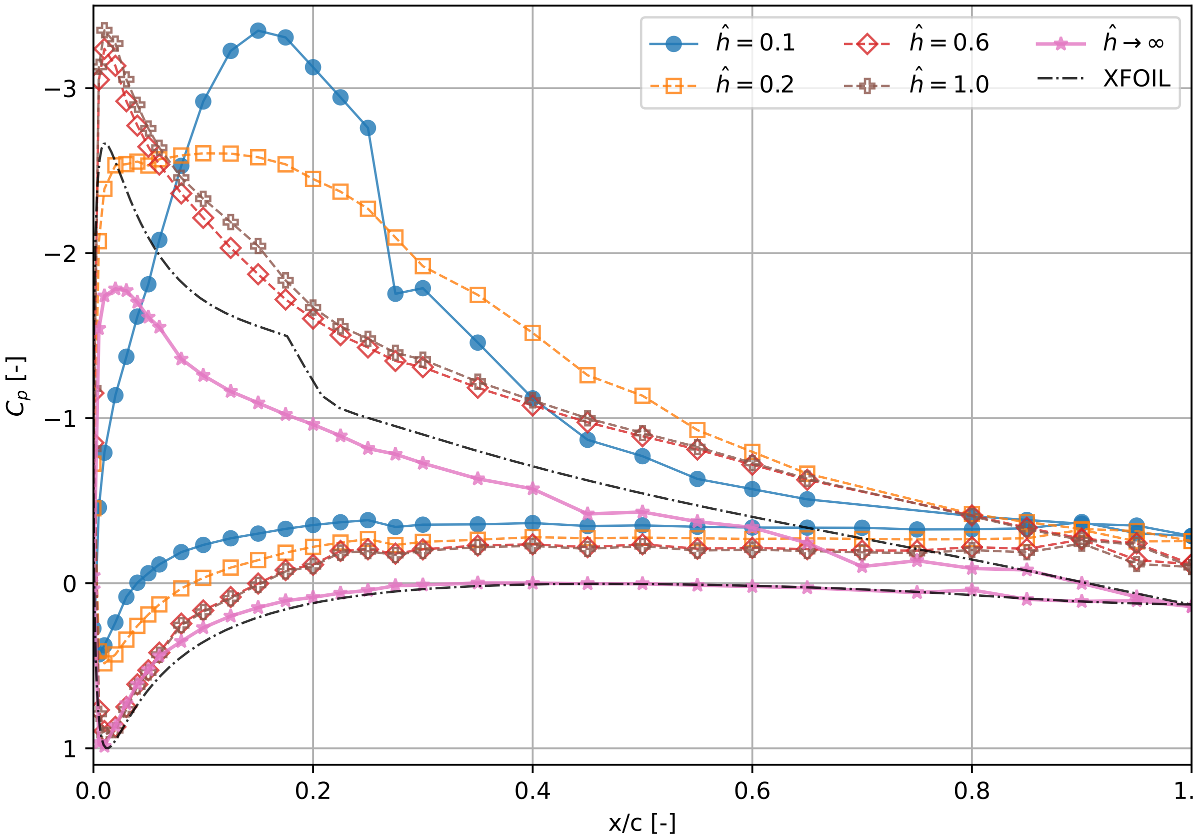

Figure 6.8: C_P at $\alpha = -8°$ at selected H.

In Figure 6.8, the OGE condition at $\alpha = -8°$ is characterised by fully attached flow with moderate suction over the suction side and smooth pressure recovery towards the trailing edge. No leading-edge separation is present, and the wake remains thin. Introducing the ground produces a marked increase in downforce relative to OGE. At $H \simeq 0.2$ and 0.1, the pressure on the ground-facing surface decreases significantly over much of the chord. This behaviour is consistent with gap acceleration driven by the Venturi effect, in which geometric confinement increases the local streamwise velocity beneath the airfoil and reduces static pressure. The pressure side remains comparatively insensitive to H, except at $H = 0.1$, where the abrupt rise in C_P is attributed to pressure-transducer saturation rather than flow separation. As in the negative stall domain, $C_P \neq 1 \; \forall \; x/c$ at $H = 0.1$ and 0.2, indicating that a classical stagnation point is not established. This reflects the interaction of the airfoil and ground boundary layers within the narrow gap, which modifies the near-wall pressure distribution.

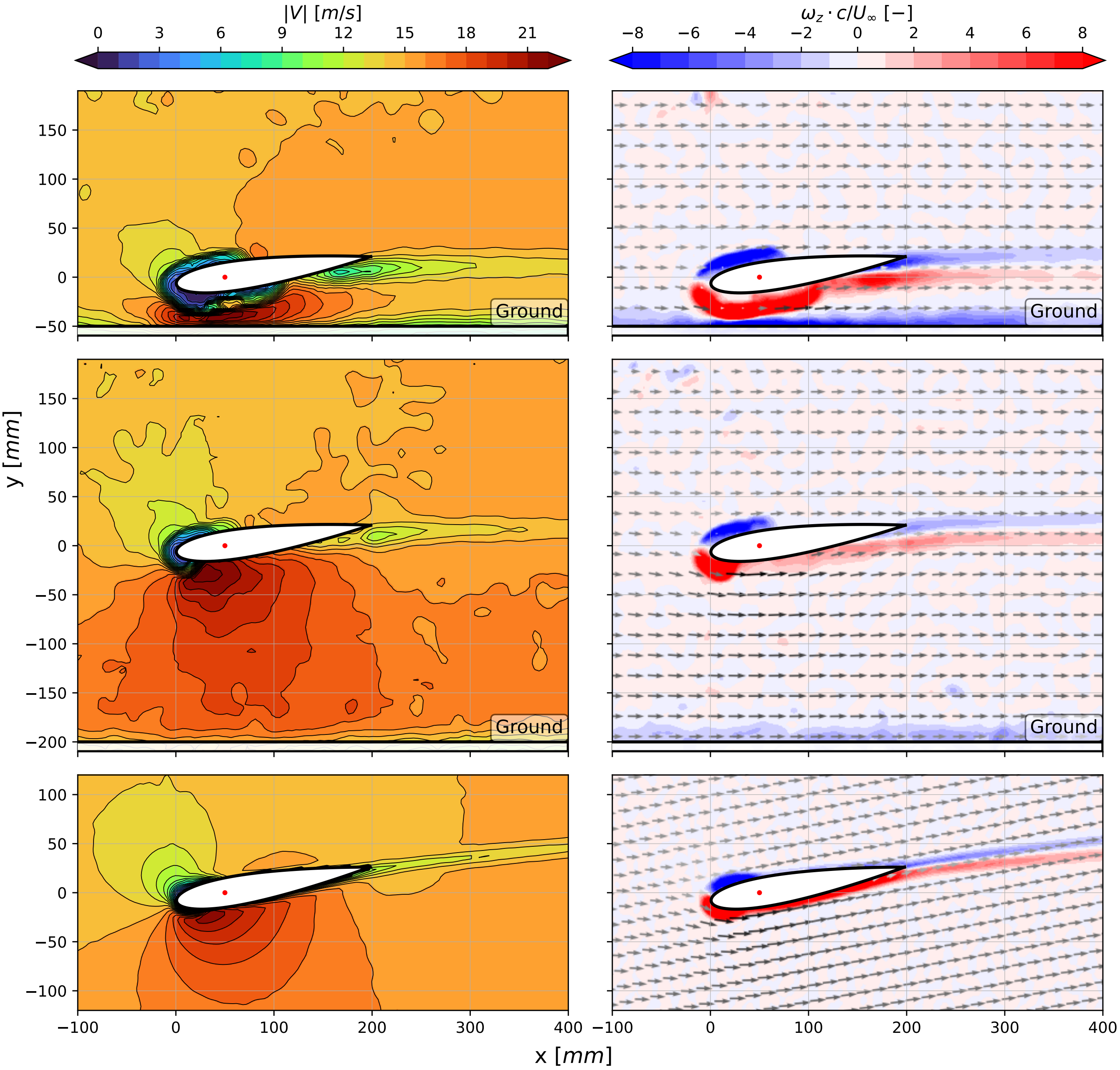

Figure 6.9: (left) Absolute velocity magnitude $|V|$. (right) Non-dimensional vorticity $\omega_z c/U_\infty$ ($\omega_z = dv/dx - du/dy$). For $\alpha = -8^\circ$. Panels: (top) $H \simeq 0.2$; (mid) 1.0; (bot) ∞.

The velocity and vorticity fields at $\alpha = -8^\circ$ in Figure 6.9 further clarify the clearance dependence. At $H \simeq 0.2$, a pronounced acceleration region develops beneath the airfoil, extending over a large fraction of the chord. The suction-side flow remains attached, although mild trailing-edge separation may occur due to the restricted mass flow through the gap. The wake is narrower than in the OGE case, indicating reduced momentum deficit and limited separation losses. At $H = 1$, the flow remains largely attached and resembles the OGE condition, with only modest enhancement of suction-side velocity. A small trailing-edge separation bubble may be present, but its extent is limited. The corresponding pressure distribution shows stronger leading-edge suction compared to OGE, consistent with the observed increase in downforce.

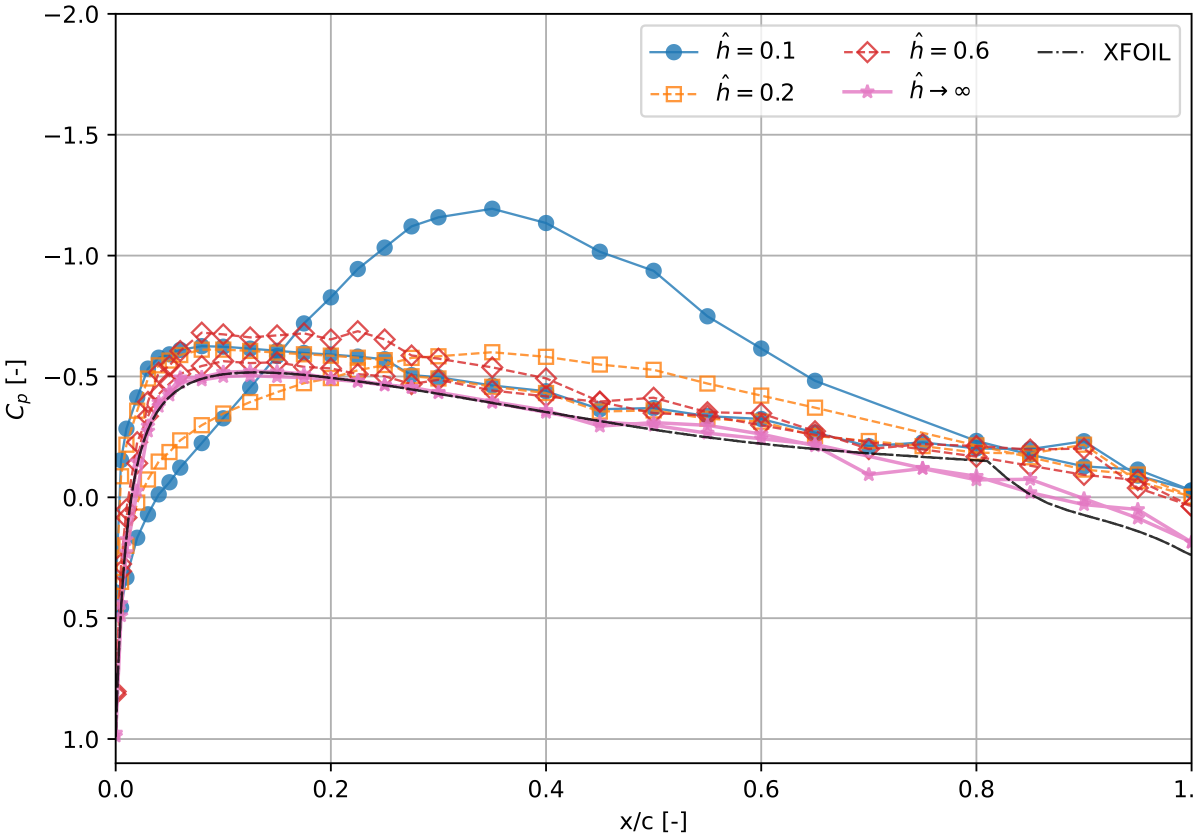

Figure 6.10: C_P at α = $0°$ at selected H.

At small angles of attack, the airfoil begins to generate downforce when operated close to the ground. Figure 6.10 shows that the side facing the ground experiences a significant reduction of C_P due to the Venturi effect, where geometric confinement increases the local streamwise velocity beneath the airfoil, reducing static pressure and generating a net aerodynamic force directed towards the ground. Consequently, the sectional lift coefficient becomes negative. In terms of the normalised coefficient $\bar{C}_\ell$, this manifests as values below unity — not because the magnitude of the aerodynamic force is small, but because its direction is reversed relative to the OGE reference. The onset of downforce at $\alpha = 0°$ therefore represents a transition from circulation-dominated loading to confinement-driven pressure redistribution.

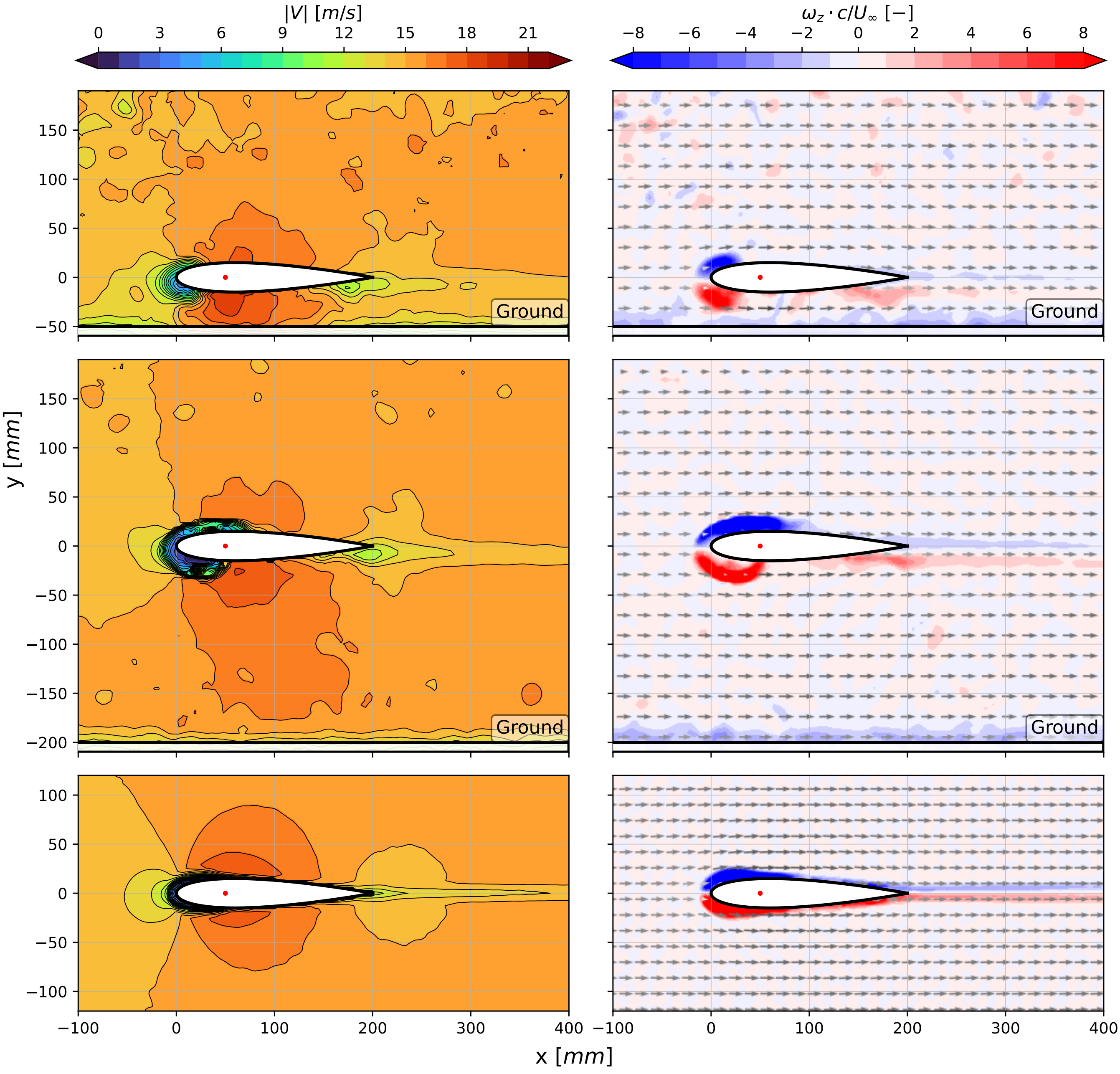

Figure 6.11: (left) Absolute velocity magnitude $|V|$. (right) Non-dimensional vorticity $\omega_z c/U_\infty$ ($\omega_z = dv/dx - du/dy$). For $\alpha = 0°$. Panels: (top) $H \simeq 0.2$; (mid) 1.0; (bot) ∞.

The velocity and vorticity fields at $\alpha = 0°$ in Figure 6.11 support this interpretation. A pronounced band of negative vorticity develops along the ground immediately downstream of the leading edge, indicating strong straining and growth of the ground boundary layer. Peak intensity occurs near $x/c \simeq 0.1$, coinciding with the region of initial gap acceleration. The near-wall vorticity amplification demonstrates that the acceleration process is not inviscid; instead, it arises from interaction between the incoming boundary layer and the constricted passage.

At $H \simeq 0.2$, the streamwise velocity field shows slight deceleration upstream of the leading edge, followed by clear acceleration beneath the airfoil toward mid-chord. This pattern is consistent with a Venturi-effect response in which the effective throat forms downstream of the leading edge. The redistribution of momentum within the gap produces sustained low pressure over a substantial portion of the lower surface. At $H = 1$, the flow approaches classical OGE behaviour. As gap acceleration weakens, the ground boundary layer remains thin, and the wake recovers rapidly. Ground proximity still influences the aerodynamic loading in this case, but confinement-induced pressure redistribution is significantly reduced.

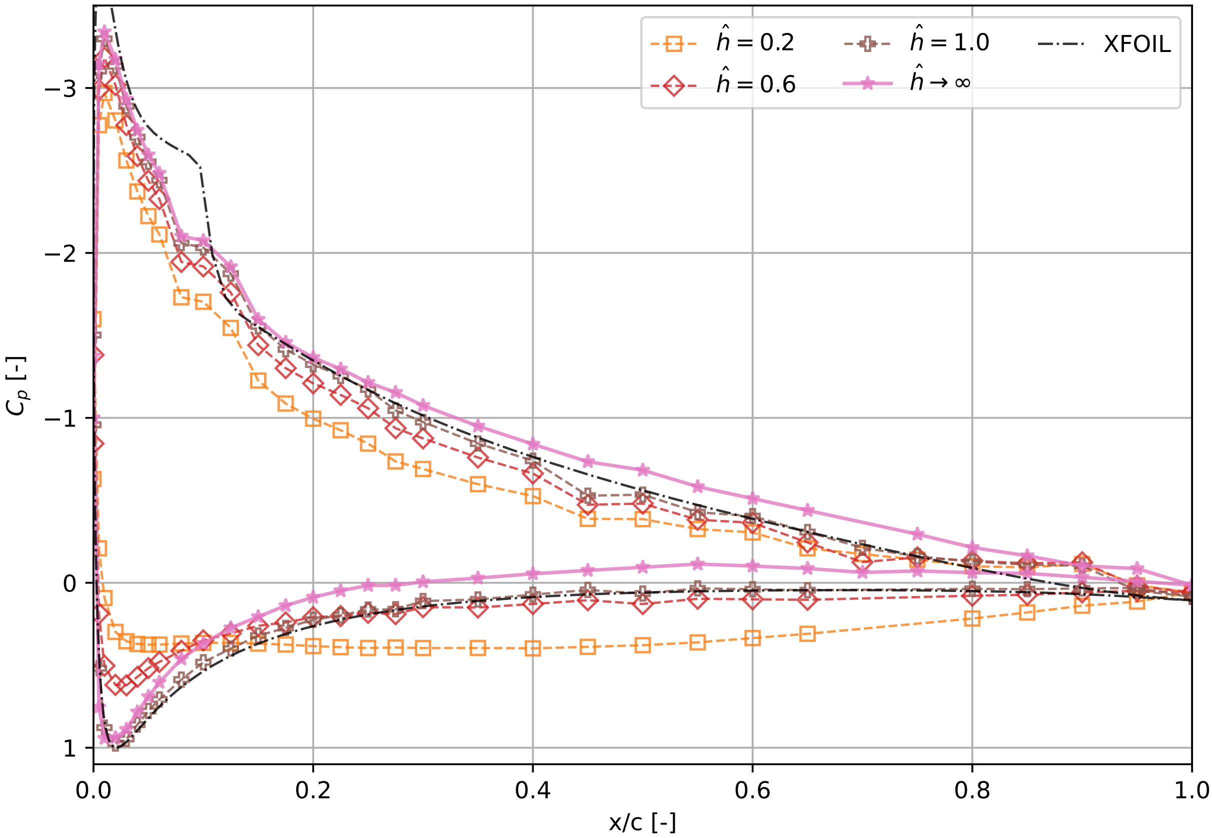

Figure 6.12: C_P at α = $10°$ at selected H.

At $\alpha = 10°$, the influence of ground proximity shifts further towards the pressure side of the airfoil. Unlike in lower angles of attack, suction-side loading is only weakly affected by H, whereas the pressure-side distribution exhibits clear modulation. As shown in Figure 6.12, moderate clearances ($H = 0.6$ and 1) produce only slight deviations from the OGE distribution. At $H \simeq 0.2$, however, the pressure-side C_P is substantially modified, indicating strong confinement effects within the gap.

Notably, a classical stagnation point is not established for $H \simeq 0.2$, and the same tendency is observable at $H = 0.6$. The absence of $C_P = 1$ over the chord suggests that boundary-layer interaction between the airfoil and ground alters the near-wall pressure field sufficiently to prevent the formation of a well-defined stagnation location.

Across the attached-flow domain, the interaction mechanism is consistent: decreasing H enhances confinement of the pressure-side flow. However, at $\alpha = 10°$ the steady fields indicate a transition from acceleration-dominated behaviour (as observed at $\alpha = -8°$ and $0°$) towards viscous blockage. As shown in Figure 6.13, at $H \simeq 0.2$, near-wall confinement limits the attainable streamwise velocity beneath the airfoil, with a maximum value of approximately $0.85 \cdot U_\infty$. This velocity cap indicates that the combined displacement thickness of the interacting boundary layers occupies a substantial fraction of the available gap height. Rather than producing further acceleration, the constricted passage promotes mixing of the boundary layers, resulting in a broad low-speed region beneath and downstream of the airfoil and a thicker, more persistent wake. At $H = 1$, the flow remains largely OGE-like. Suction-side acceleration over the upper surface is well defined, the wake remains narrow, and downstream recovery is rapid. In this case, aerodynamic loading remains dominated by suction-side circulation rather than by pressure-side confinement.

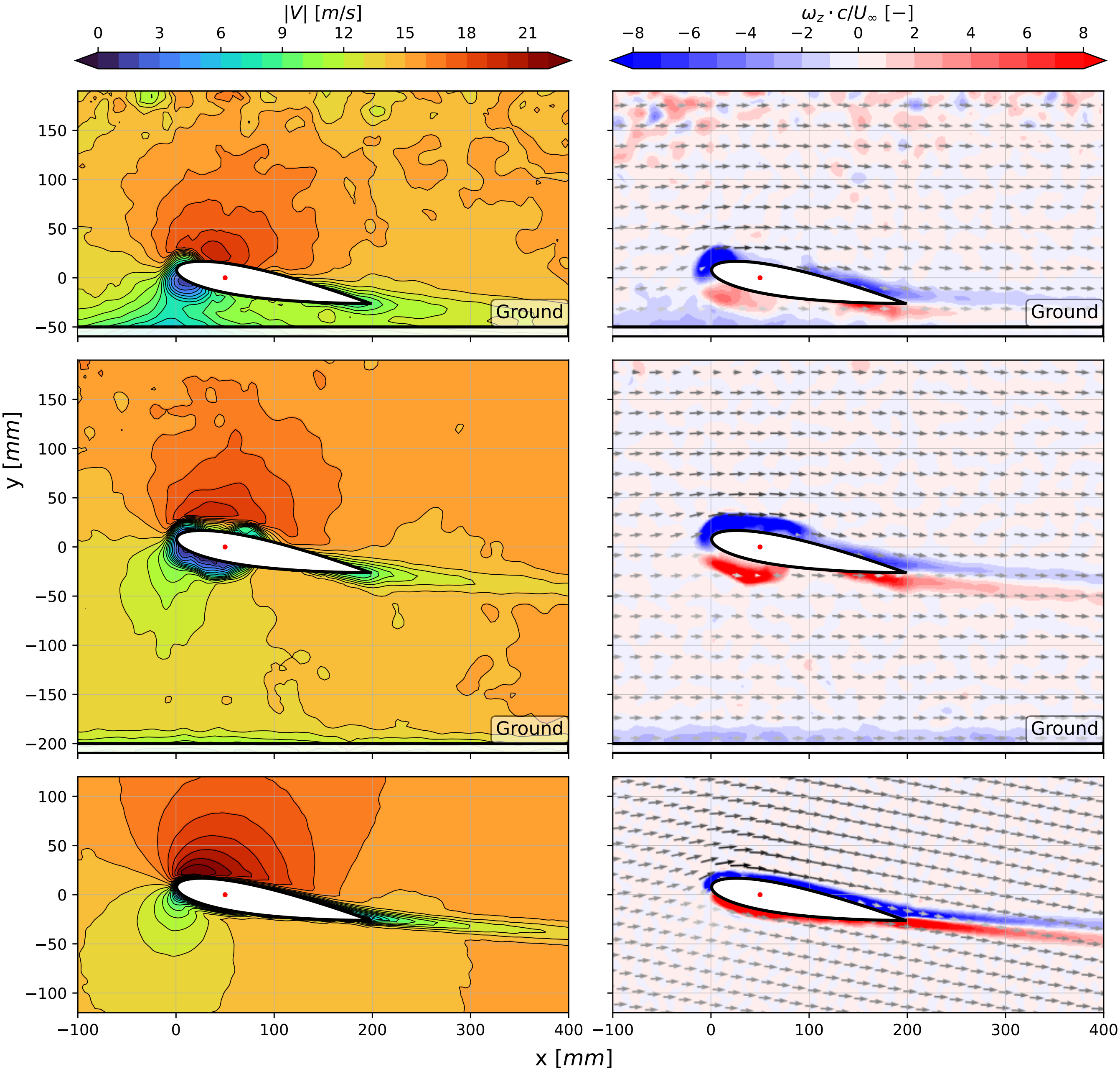

Figure 6.13: (left) Absolute velocity magnitude $|V|$. (right) Non-dimensional vorticity $\omega_z c/U_\infty$ ($\omega_z = dv/dx - du/dy$). For $\alpha = 10^\circ$. Panels: (top) $H \simeq 0.2$; (mid) 1.0; (bot) ∞.

Taken together, the $\alpha = -8^\circ$, 0°, and 10° cases illustrate a progressive shift in the governing ground-effect mechanism within the attached-flow domain. At negative and near-zero incidence, aerodynamic loading is enhanced primarily through acceleration- and confinement-driven reductions in surface pressure on the ground-facing side.

Unlike the negative-stall domain, where the ground primarily suppresses and confines suction-side separation, geometric confinement and boundary-layer interaction govern the attached-flow domain by modifying the ground-side flow. This transition from acceleration-enhanced loading to blockage-limited behaviour provides the physical bridge between low-incidence ground-effect augmentation.

6.3.3. Positive Stall

In the positive stall domain, ground proximity exerts a dual, competing influence: suppression of suction-side leading-edge separation and viscous blockage in the gap. The combined C_P overlays and PTV fields reveal how the relative importance of these mechanisms depends on H and incidence.

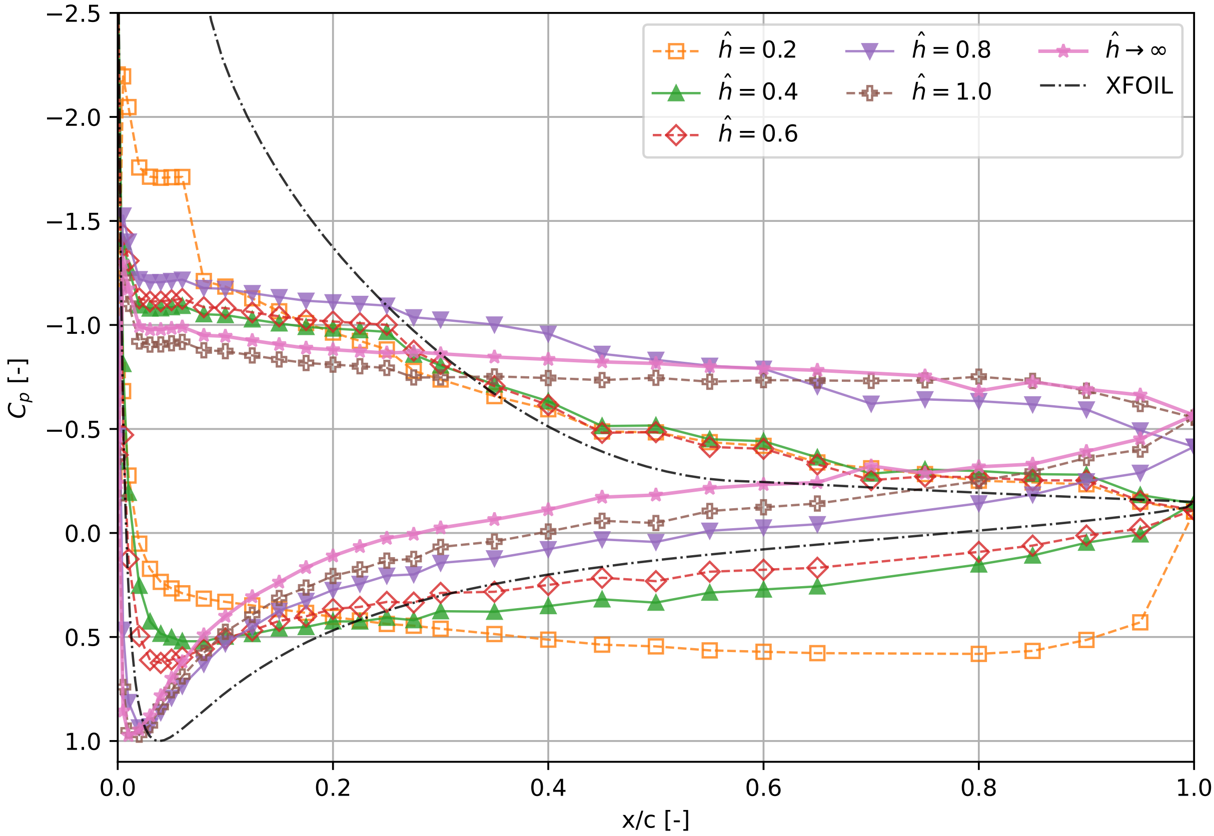

Figure 6.14: C_P at α = $16°$ at all H tested ($\alpha = 15°$ for $H \simeq 0.2$).

At the extreme angle of $\alpha = 16°$, the gap at the trailing edge is effectively 0 for $H \simeq 0.2$, which causes the flow to spill over the airfoil, and nearly no mass flow travels between the airfoil and the ground. The pressure side at other heights remains significantly altered, with it consistently exhibiting a higher C_P, while the suction side shows a lower C_P peak at the leading edge. It is again observed that the leading edge on the pressure side does not reach stagnation.

Under OGE conditions at $\alpha \approx 15°$, separation initiates near the leading edge at approximately $x/c \approx 0.1$, producing an extended separated shear layer and a broad wake. When the airfoil operates at finite clearance, this leading-edge separation is suppressed. For all tested H, large-scale suction-side detachment observed in OGE is no longer present. Instead, the separated region is displaced downstream or eliminated, depending on clearance.

The velocity fields in Figure 6.15 show that streamwise velocities beneath the airfoil remain substantially below U_∞, indicating viscous blockage rather than ideal Venturi acceleration. This blockage modifies the pressure distribution in two ways. First, suppression of leading-edge separation sustains higher suction over the upper surface compared to OGE. Second, the reduced effective throat area beneath the airfoil alters the pressure-side distribution, sometimes producing local recirculation near the trailing edge. In the reconstructed C_P fields, this behaviour appears as extended regions where $C_P \approx 1$, reflecting both choking and limited spatial resolution of the pressure measurements.

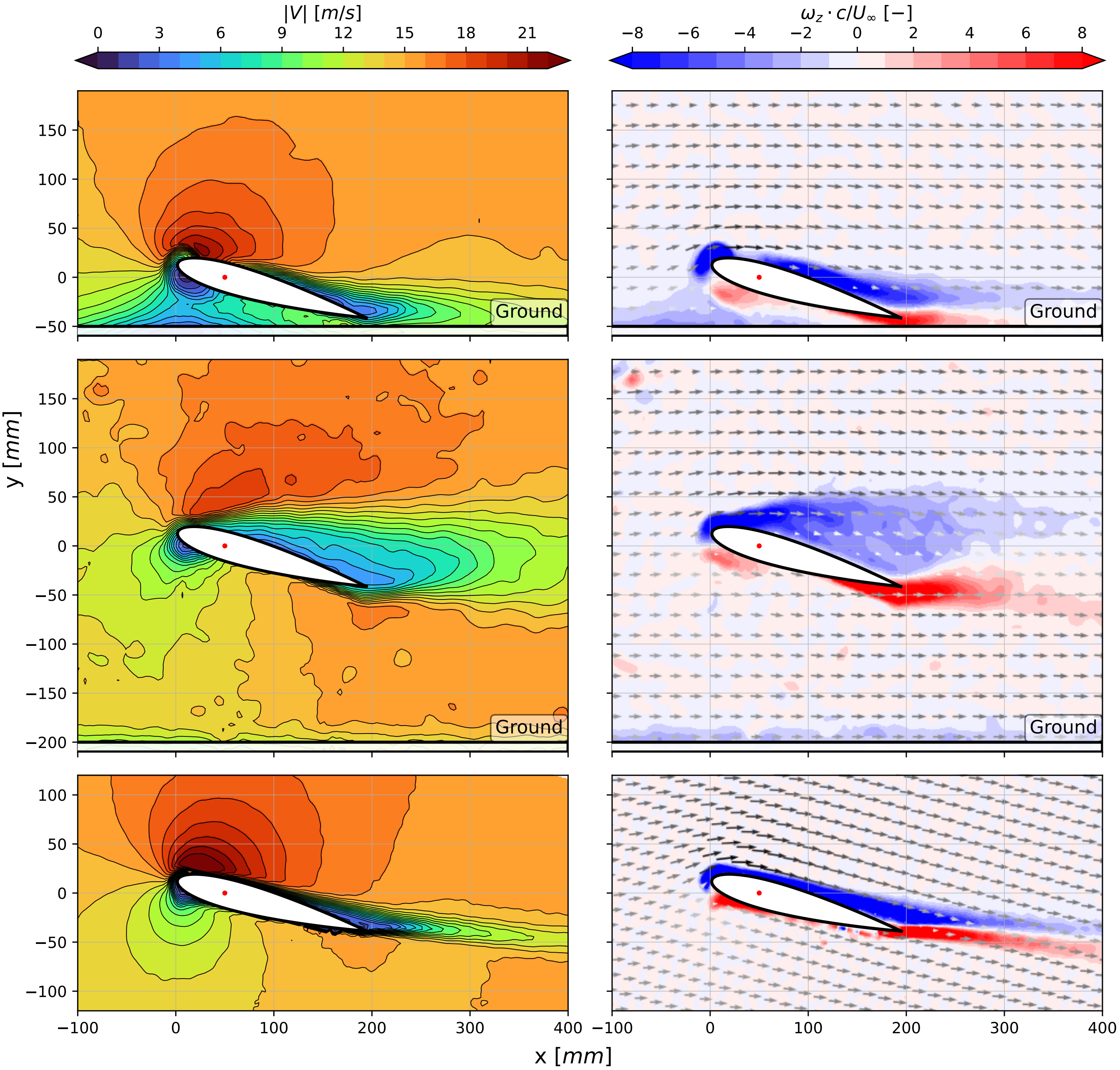

Figure 6.15: (left) Absolute velocity magnitude $|V|$. (right) Non-dimensional vorticity $\omega_z c/U_\infty$ ($\omega_z = dv/dx - du/dy$). For $\alpha = 16^\circ$ ($\alpha = 15^\circ$ for $H \simeq 0.2$). Panels: (top) $H \simeq 0.2$; (mid) 1.0; (bot) ∞.

The positive stall domain demonstrates the dual role of ground proximity. At low clearance, suction-side separation is suppressed, delaying stall relative to OGE, while simultaneous viscous blockage within the gap limits acceleration and modifies the pressure-side flow. At larger clearance, blockage weakens, and classical stall behaviour progressively re-emerges; the balance between separation suppression and confinement thus governs the high-incidence response. Compared with the negative incidences, separation on the suction side at positive incidences occurs earlier and migrates upstream more rapidly as H increases. This asymmetry reflects the reduced ability of the flow to sustain suction-side attachment once the pressure-side confinement weakens.

From Figure 6.2–Figure 6.15, the steady measurements establish a picture of how ground proximity modifies both the aerodynamic coefficients and the underlying flow topology of the NACA0015 airfoil. In the linear lift domain, reducing H increases the lift-curve slope relative to OGE, consistent with classical ground-effect arguments of reduced induced effects and enhanced circulation. At low and moderate incidence, the dominant mechanism is confinement-driven pressure redistribution on the ground-facing side. As the gap contracts, streamwise acceleration beneath the airfoil reduces static pressure and can generate downforce at small α, as evidenced by the C_P overlays and near-wall vorticity development.

As the airfoil is brought closer to the ground, however, the response is not monotonic. Below a critical height, typically within $0.2 < H \leq 0.4$, the beneficial pressure redistribution is increasingly offset by viscous losses. A particularly important threshold is reached when the minimum local clearance satisfies $H < 0.6$, i.e., when any portion of the airfoil approaches the ground sufficiently closely for the boundary layers on the airfoil and ground to interact directly. For these configurations, the onset of strong interaction between the airfoil and the ground boundary layers becomes evident: the effective flow area in the gap is reduced by displacement effects, near-wall velocities are capped, and the gap flow transitions to blockage or choking. This transition is reflected in the steady PTV fields by thickened wakes, sustained regions of low momentum beneath and downstream of the airfoil, and vorticity concentrations associated with intensified near-wall shear.

In stalled conditions, ground effect plays a dual role. Near-wall confinement suppresses or delays suction-side separation relative to OGE, while simultaneously strengthening pressure-side blockage once H becomes sufficiently small. At larger clearances, confinement effects weaken, and the flow progressively returns to the classical free-air behaviour, with upstream migration of separation and wake broadening.

Finally, the pressure-based trends at high positive angles must be interpreted in light of the documented suction-side transducer saturation (See subsection 5.1.1). While this limits the quantitative accuracy of peak suction levels and can depress the measured C_ℓ, the combined pressure and PTV evidence indicates that the main physical trends of acceleration-driven loading at moderate clearance and blockage-dominated behaviour at very low heights remain robust.

Overall, the steady results show that ground effect is governed not solely by geometric proximity but by the competition between inviscid-like pressure redistribution and viscous boundary-layer interaction in the gap. This steady-flow baseline provides the physical context required to interpret the unsteady pitching results presented in the subsequent sections.

6.4. Unsteady Aerodynamics

As mentioned in subsection 4.5.2, the investigation focuses on three distinct flow domains: attached flow, and dynamic stall development in both the negative and positive stall ranges.

6.4.1. Attached Flow

The unsteady aerodynamic response for the attached-flow domain is evaluated through lift-coefficient (C_ℓ) hysteresis loops, phase-averaged surface pressure contours (C_P), and phase-resolved PTV flow fields. To elucidate the coupling between kinematic rate and ground proximity, results are synthesised across a reduced frequency spectrum of $k = [0.05, 0.10, 0.15, 0.20]$ and a few selected non-dimensional heights $H = [0.2, 0.6, 1.0, \infty]$. The prescribed motion is a harmonic pitch about the quarter-chord point defined by $\alpha(t) = 0° + 10° \sin \omega t$.

As demonstrated in Figure 6.16, the evolution of the hysteresis loops is primarily characterised by changes in the phase lag rather than significant shifts in the maximum or minimum lift amplitudes. According to classical unsteady theory, the circulatory lift is governed by Theodorsen's function $C(k)$, which introduces both an attenuation in amplitude and a phase lag relative to the quasi-steady state. In the current results, the phase lag—visualised as the width or thickness of the $C_\ell - \alpha$ loop—emerges as the most sensitive indicator of ground interference.

At the lowest reduced frequency ($k = 0.05$), the lift response remains predominantly quasi-steady, as evidenced by the high degree of symmetry in the loops and the close alignment with the Theodorsen prediction and steady lift curves. For the case ($H \simeq 0.2$ and 0.6), the unsteady lift modulation is negligible, with the phase-averaged data collapsing onto the steady lift curve. However, as the airfoil moves away from the ground, the lift response starts to resemble $H \to \infty$.

As the reduced frequency increases to $k = 0.10$ and $k = 0.15$ (see Figure 6.16), the flow field transitions away from the quasi-steady limit. The hysteresis loops widen significantly at all heights, reflecting the finite time required for the wake vorticity to adjust to changes in circulation. This phase lag, governed by Theodorsen's function $C(k)$, represents the 'memory' of the flow as the trailing-edge vorticity is shed and conducted downstream.

However, the influence of ground proximity on this phase lag is distinctly non-monotonic. At intermediate clearances ($H = 0.6$ and 1.0), the hysteresis loops are observed to be generally narrower than the OGE case. This trend can be explained by the Venturi effect: the physical presence of the ground constricts the flow, accelerating the local velocity beneath the airfoil. This increased wake propagation speed ($U > U_\infty$) reduces the convective time scale required for circulation to equilibrate. Consequently, the lift response remains more tightly coupled to the instantaneous kinematics, resulting in a compression of the hysteresis.

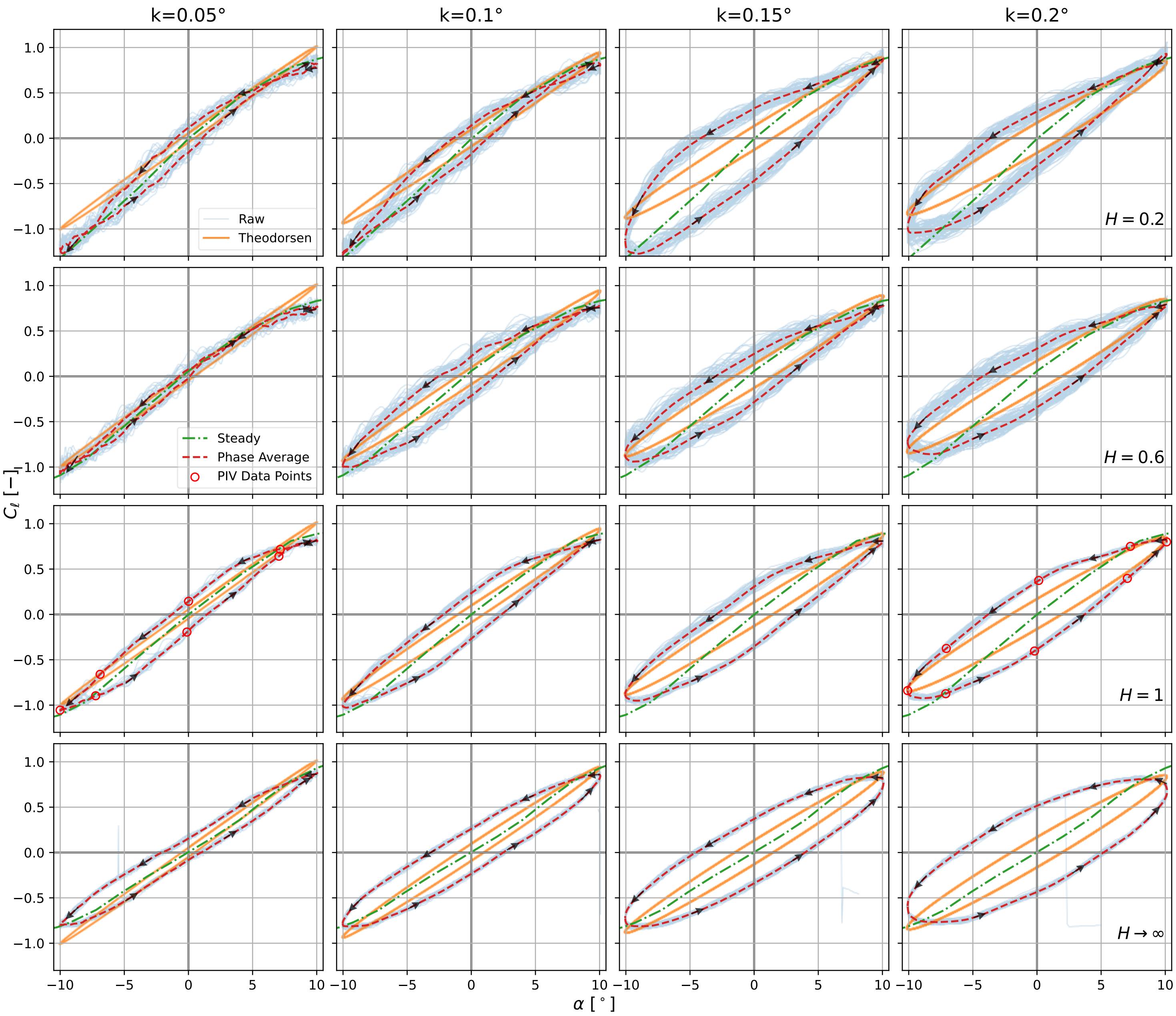

Figure 6.16: C_ℓ vs α for at various heights H (top to bottom): $[0.2, 0.6, 1.0, \infty]$ and reduced frequency k (left to right): $[0.05, 0.10, 0.15, 0.20]$.

At $H = 0.2$, the hysteresis loop expands significantly. In this extreme ground effect, air-column stiffening and physical confinement introduce a blockage effect dominating Venturi acceleration. Wall proximity hinders wake shedding as the airfoil interacts with its aerodynamic 'footprint' trapped in the gap. Resistance to flow re-attaching is exacerbated by viscous interactions, slowing wake propagation and causing a substantial increase in phase lag and wider $C_\ell - \alpha$ loops, departing from the trends observed at higher clearances.

Figure 6.17 provides pressure-field evidence: suction intensifies and broadens chord-wise. At $H = 0.2$, the development of the leading-edge suction peak lags significantly behind the geometric incidence during the downstroke. Conversely, during the upstroke, the pressure on the ground-facing surface rises abruptly as the trailing edge approaches the wall, a result of the high sensitivity of the gap-flow blockage to diminishing clearance. In the highly unsteady domain ($k = 0.20$), unsteadiness becomes the dominant characteristic of the flow; a transition occurs where temporal inertia begins to limit the development of the suction peak magnitude. This attenuation indicates that at high pitching rates, the flow cannot establish the full "ground-effect footprint" before the motion reverses, even as the lift hysteresis continues to grow due to the substantial phase shift.

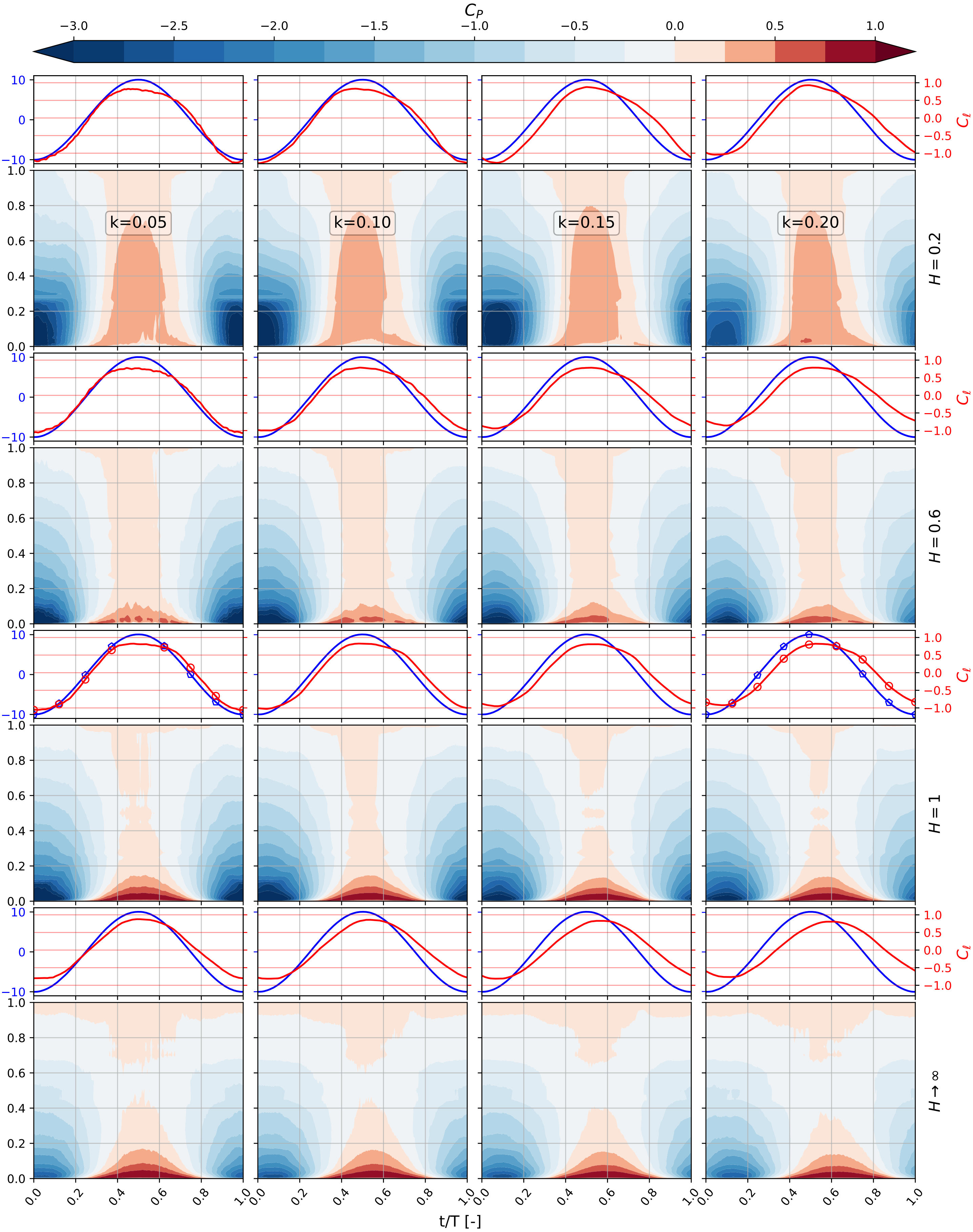

Figure 6.17: α, C_ℓ, and C_P contour over x/c vs t/T map at various heights H (top to bottom): $[0.2, 0.6, 1.0, \infty]$ and reduced frequency k (left to right): $[0.05, 0.10, 0.15, 0.20]$.

A further distinction in the ground-effect domain is the increasing asymmetry of the hysteresis loops relative to the steady-state lift curve. In contrast, the OGE loops remain largely symmetric about the linear lift slope; the paths for finite H exhibit non-uniform deviations. This is particularly evident at low reduced frequencies ($k = 0.05$ and 0.10) for clearances of $H = 0.2$ and 0.6, where the phase-averaged C_ℓ curves display pronounced localised fluctuations. Rather than representing persistent aerodynamic structures, these irregularities point to a significant degree of cycle-to-cycle variability. Such stochastic behaviour suggests that the flow does not repeat identically during each oscillation at very small ground clearances. The proximity of the wall likely promotes boundary-layer interactions also observed in section 6.2, which inhibit convergence towards a smooth phase-averaged response. At higher reduced frequencies, the larger number of oscillations included in the averaging process improves convergence of the phase-averaged response, reducing the variability evident at lower reduced frequencies.

Furthermore, an apparent attenuation of C_ℓ is observed at high incidences ($\alpha > 10°$), for finite H. It must be noted that this reduction in peak lift is an experimental artefact rather than a physical aerodynamic limit; it arises from the saturation of the pressure transducers at high suction magnitudes (see subsection 5.1.1). Despite this localised attenuation, the overall trends regarding loop width and phase lag remain consistent and provide a reliable basis for evaluating the influence of ground proximity.

Despite this weakening of the peak pressure loading, the lift hysteresis continues to grow, driven by the substantial phase shift across the entire chord. Throughout this frequency sweep, the flow remains fully attached, as confirmed by the continuous nature of the C_P distributions in Figure 6.17. The absence of abrupt pressure collapses or discontinuities suggests that the current parameters remain below the threshold for dynamic stall, setting a baseline for the separated flow investigations that follow.

Figure 6.18 to Figure 6.21 present the phase-resolved velocity magnitude $|V|$ and non-dimensional span-wise vorticity $\omega_z c/U_\infty$ fields—where $\omega_z = dv/dx - du/dy$, u is the x-component of the velocity and v is the y-component of the velocity—for the $H = 1$ case with mean incidence of $\alpha = 0°$ and a pitching amplitude of $10°$. These measurements provide direct spatial evidence of the quasi-steady and highly unsteady aerodynamics as the reduced frequency is increased from $k = 0.05$ to $k = 0.20$. These fields confirm that the flow remains fully attached across both the suction and pressure surfaces for the entire range of investigated angles of attack, establishing a baseline for attached-flow behaviour.

At the lower reduced frequency of k=0.05 (Figure 6.18 and Figure 6.19), the flow field maintains a characteristic quasi-steady topology throughout the pitching cycle. The wake is observed to be narrow and recovers its momentum rapidly downstream, indicating a lack of significant geometric confinement or viscous blockage at this clearance. The vorticity is concentrated in thin, well-defined shear layers, which adjust nearly instantaneously to changes in the kinematic state. This absence of significant 'wake memory' correlates with the negligible phase lag and narrow hysteresis observed in the force measurements. Furthermore, the flow features at $k = 0.05$ correspond closely with the steady-state results discussed in section 6.2; notably, higher peak velocities are achieved on the suction surface compared to the $k = 0.20$ case, as the lower oscillation rate allows the flow sufficient time to establish a fully developed suction footprint.

In contrast, at $k = 0.20$ (see Figure 6.20 and Figure 6.21), the flow field enters a firmly unsteady domain where the temporal history of the flow significantly distorts the instantaneous flow state, while the flow remains attached, the wake becomes noticeably thicker, recovers further downstream, and exhibits a pronounced curvature that reflects the trajectory of the airfoil at previous phase angles — a hallmark of convective phase lag. A comparison of the velocity fields at the same geometric incidence (e.g., $\alpha = 0°$ on the upstroke versus the downstroke) reveals a distinct asymmetry in the flow topology. This asymmetry provides a physical explanation for the observed lift hysteresis, as the wake propagation speed and the resulting back-pressure on the trailing edge differ depending on the direction of motion.

The velocity magnitude contours at $k = 0.20$ demonstrate that the high-velocity region on the suction surface is spatially smoother, reduced in magnitude, and less localised than at $k = 0.05$. This supports the 'weakening' of the instantaneous suction response noted in Figure 6.17, which is attributed to the dominance of temporal inertia over the establishment of a quasi-steady pressure footprint. At this higher frequency, the flow is driven progressively further from equilibrium, leading to the increased phase lag and larger hysteresis loop areas seen in Figure 6.16. The PTV data demonstrates that at $H = 1$, the interaction with the ground is still relatively weak compared to the influence of the reduced frequency; however, the ground boundary layer is slightly more perturbed during the downstroke. This suggests the onset of height-dependent trends, where ground proximity begins to modify the wake propagation velocity, that define the more extreme, non-monotonic ground-effect domains discussed in section 6.2.

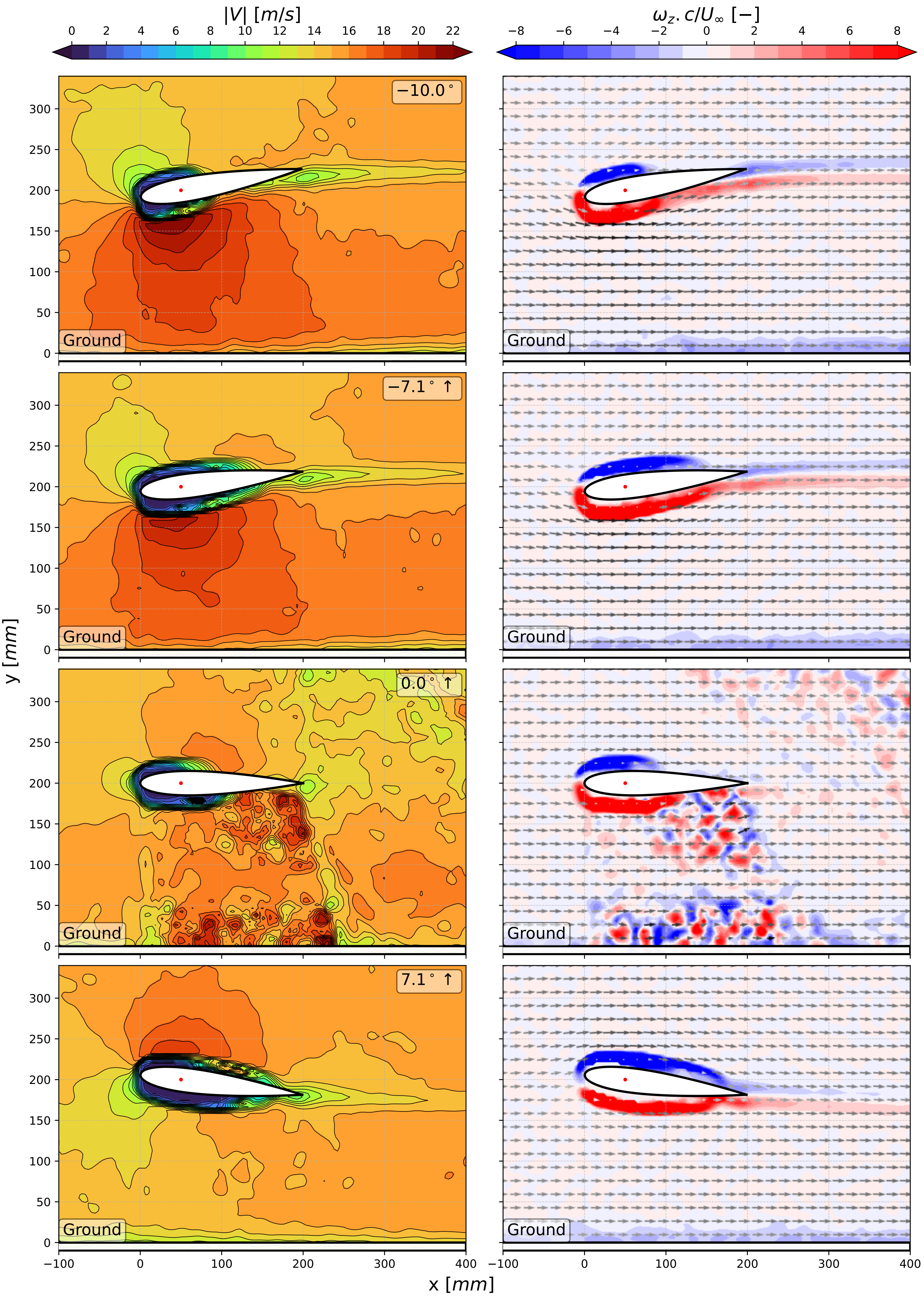

Figure 6.18: Phase-resolved PTV fields for the upstroke cycle of $H = 1$ and $k = 0.05$: (left) Absolute velocity magnitude $|V|$. (right) Non-dimensional vorticity $\omega_z c/U_\infty$ ($\omega_z = dv/dx - du/dy$).

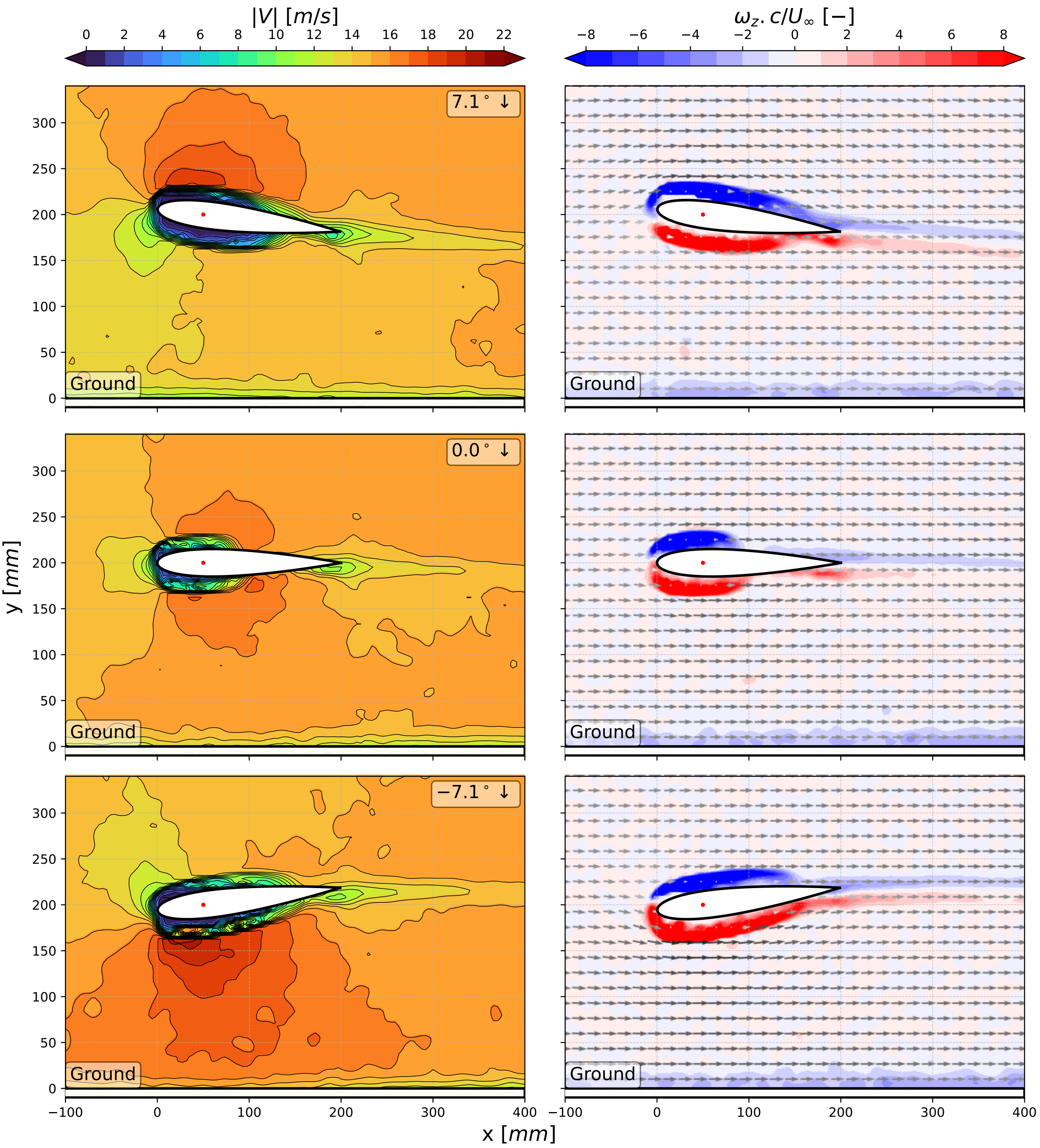

Figure 6.19: Phase-resolved PTV fields for the downstroke cycle of $H = 1$ and $k = 0.05$: (left) Absolute velocity magnitude $|V|$. (right) Non-dimensional vorticity $\omega_z c/U_\infty$ ($\omega_z = dv/dx - du/dy$).

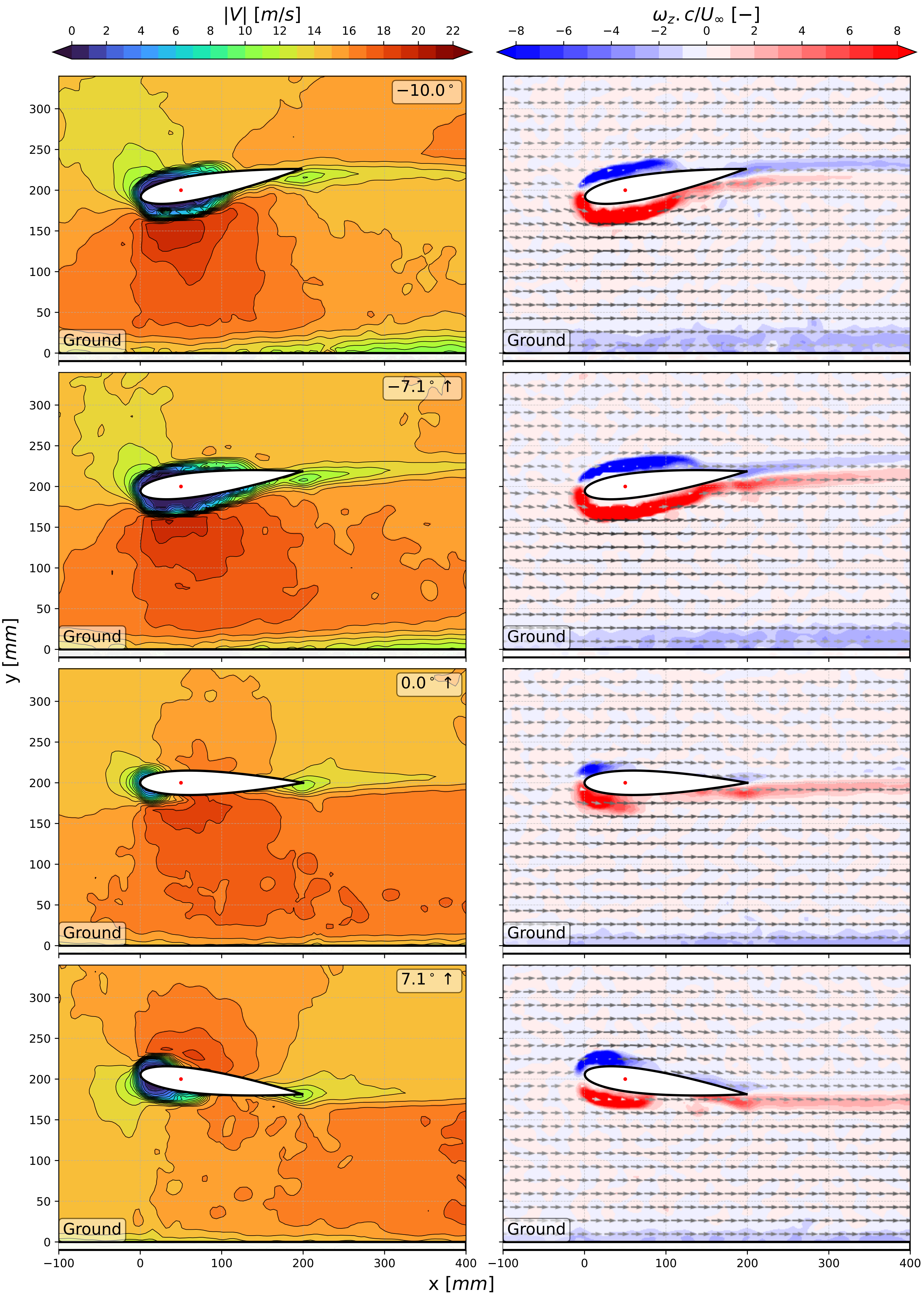

Figure 6.20: Phase-resolved PTV fields for the upstroke cycle of $H = 1$ and $k = 0.20$: (left) Absolute velocity magnitude $|V|$. (right) Non-dimensional vorticity $\omega_z c/U_\infty$ ($\omega_z = dv/dx - du/dy$).

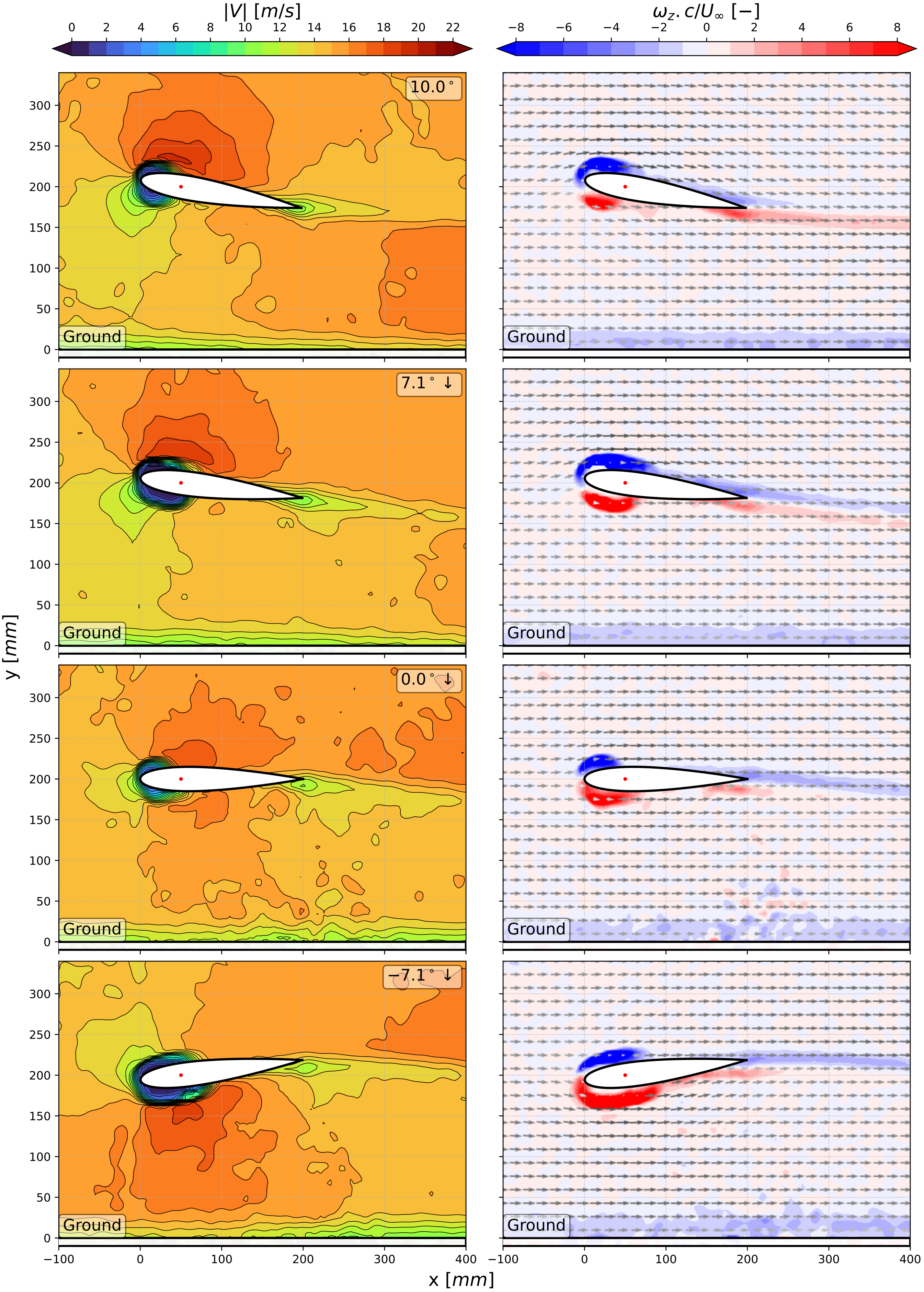

Figure 6.21: Phase-resolved PTV fields for the downstroke cycle of $H = 1$ and $k = 0.20$: (left) Absolute velocity magnitude $|V|$. (right) Non-dimensional vorticity $\omega_z c/U_\infty$ ($\omega_z = dv/dx - du/dy$).

6.4.2. Dynamic Stall

Negative Stall

The unsteady aerodynamic response within the negative dynamic stall domain is evaluated through lift-coefficient (C_ℓ) hysteresis loops, phase-averaged surface pressure maps (C_P), and phase-resolved PTV flow fields. This domain, characterised by the oscillation of the airfoil through its static stall angle at negative incidences $\alpha(t) = -10^\circ + 10^\circ \sin \omega t$, reveals a complex interplay between the formation of the Dynamic Stall Vortex (DSV) and the geometric constraints imposed by ground proximity.

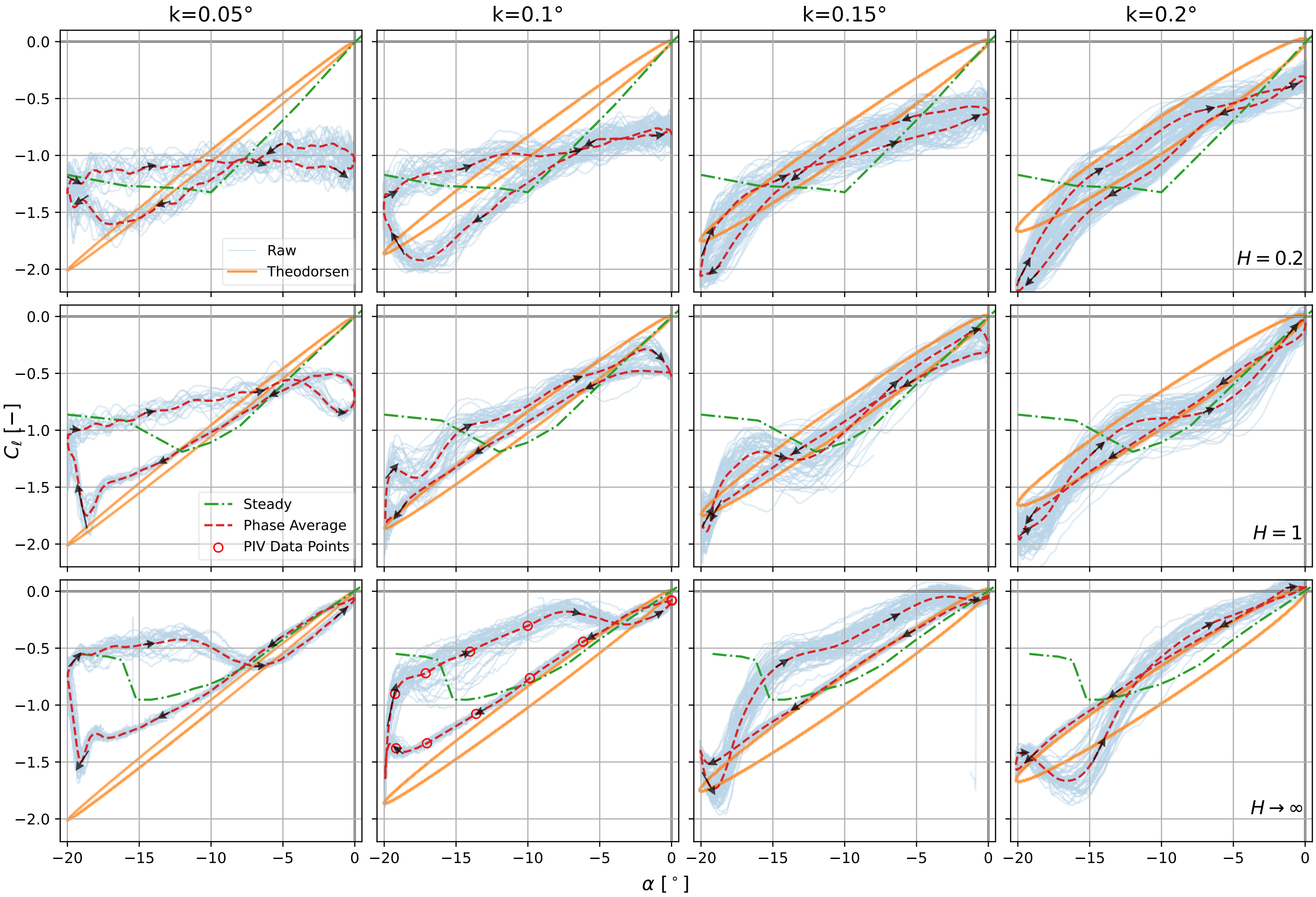

Figure 6.22: C_ℓ vs α for at various heights H (top to bottom): $[0.2, 1.0, \infty]$ and reduced frequency k (left to right): $[0.05, 0.10, 0.15, 0.20]$.

As demonstrated in Figure 6.22, the OGE and $H = 1.0$ cases exhibit hysteresis loops characteristic of classical dynamic stall. This behaviour is marked by a pronounced lift overshoot beyond the steady-state stall angle, followed by a rapid collapse in C_ℓ associated with the shedding of a dynamic stall vortex (DSV). At $k = 0.05$ and 0.10, the $H = 1.0$ configuration still presents clear signatures of DSV-mediated stall; however, the magnitude of the post-stall C_ℓ drop is reduced relative to the OGE condition. Rather than indicating complete stall suppression, this suggests that moderate ground proximity modifies the growth and convection of the leading-edge vortex, smoothing the load collapse and redistributing the aerodynamic response over a broader portion of the oscillation cycle.

A critical observation regarding the stability of the system is the change in aerodynamic damping, represented by the area enclosed within the $C_\ell - \alpha$ loops. In the OGE case, the large, counter-clockwise loops at low k indicate a period of negative damping, where the fluid imparts energy to the structure, potentially triggering stall flutter. At $H = 0.2$, the significant reduction in loop area and the transition toward a more "plateau-like" C_ℓ response suggest a substantial increase in aerodynamic damping. By suppressing the abrupt shedding of the DSV, the ground-effect stabilises the aeroelastic response, reducing the risk of divergent oscillations.

The $H = 1.0$ configuration, therefore, represents an intermediate domain between freestream dynamic stall and strongly ground-constrained flow. As the reduced frequency increases to $k = 0.15$ and $k = 0.20$, the hysteresis loops become progressively rounder and less dominated by sharp collapse events than those observed in the OGE condition. This indicates that ground proximity begins to weaken the coherence of the stall vortex and reduce the abruptness of vortex shedding, even at clearances typically considered outside the strongest ground-effect domain.

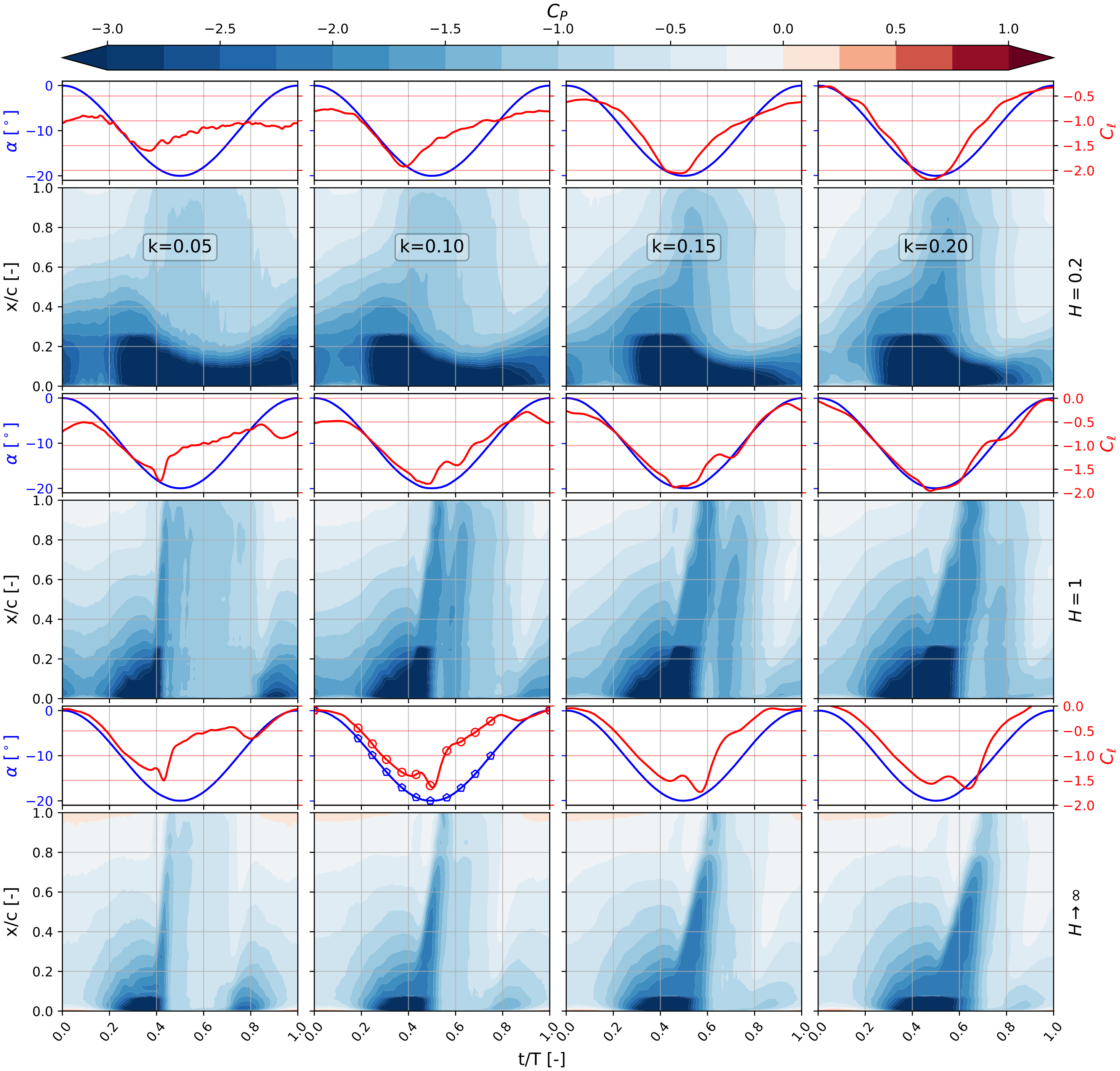

Figure 6.23: α, C_ℓ, and C_P contour over x/c vs t/T map at various heights H (top to bottom): $[0.2, 1.0]$ and reduced frequency k (left to right): $[0.05, 0.10, 0.15, 0.20]$.

In the extreme ground-effect case ($H = 0.2$), the hysteresis topology undergoes a more fundamental change. At $k = 0.05$, the sharp C_ℓ transients associated with discrete DSV shedding largely disappear. This indicates that the aerodynamic loads are governed primarily by confinement of the flow between the airfoil and the ground rather than by the formation and convection of a large coherent stall vortex. At higher reduced frequencies ($k = 0.10$-0.20), however, the loops still retain measurable hysteresis and curvature changes, implying that unsteady separation dynamics persist, albeit in a weakened and more constrained form. In this domain, the flow is therefore better characterised as a clearance-controlled separated flow, where vortex formation and breakdown occur within a confined gap and no longer produce the sharp lift overshoot typical of classical dynamic stall.

The C_P maps in Figure 6.23 elucidate the local mechanisms driving these global force trends. At $H = 1.0$ and low k, a distinct low-pressure region originates at the leading edge ($t/T \approx 0.2$), subsequently convecting chord-wise as a DSV ($0.4 < t/T < 0.5$). The convection speed of this structure is high relative to the oscillation period, leading to a period of massive separation before flow reattachment occurs at $t/T \approx 0.75$. This reattachment event produces a secondary C_ℓ rise, which is prominent at $k = 0.05$ but becomes progressively suppressed at higher frequencies. At $k = 0.20$, the reattachment process is delayed until the airfoil returns to a low effective incidence, rendering the secondary peak negligible.

At the lowest clearance ($H = 0.2$), the C_P contours confirm that the flow is entirely clearance-dominated. The narrow gap suppresses the formation of a discrete, convecting DSV and instead induces a severe acceleration of the flow between the airfoil and the wall. This "diffuser effect" maintains high suction levels and strong pressure recovery, which effectively pins the LEV between the airfoil and the ground and prevents large-scale detachment. The interaction between the airfoil and ground boundary layers likely contributes to this stability, essentially forcing the flow to remain attached through geometric constraint.

Direct spatial evidence of the DSV evolution in OGE is provided by the PTV fields for $k = 0.10$ (Figure 6.24 and Figure 6.25). During the downstroke, a significant time lag is evident: at -$19.2° \downarrow$ and $\alpha = -17.1° \downarrow$, the flow remains largely attached despite exceeding the steady-state stall threshold, supporting the observed lift overshoot. The nascent LEV is captured at $\alpha = -19.2° \downarrow$, originating from the roll-up of the leading-edge shear layer.

On the upstroke (Figure 6.25), the DSV release is manifested at $\alpha = -20°$. This structure presents as a large-scale recirculating region covering the majority of the chord. The downstream convection of the primary DSV accompanies the formation of secondary surface vorticity, which facilitates its release from the airfoil surface. This induced velocity field creates a temporary suction spike before the flow undergoes massive detachment at $\alpha = -17.1° \uparrow$. The subsequent recovery phase is characterised by the gradual re-establishment of attached flow, with the initial stages of reattachment becoming visible at $\alpha = -10° \uparrow$ as a "reattachment tongue" progressing from the leading edge.

The PTV fields for a sinusoidal motion of $\alpha(t) = -6° + 10° \sin \omega t$ at a reduced frequency of $k = 0.20$ in Figure 6.26 and Figure 6.27 demonstrate the apparent lack of DSV development in extreme ground effect $H \simeq 0.2$. In contrast to the OGE case, where a discrete DSV lifts off and convects over the suction surface, the $H = 0.2$ fields reveal a fundamental shift in the separation topology. The presence of the ground plane restricts the vertical development of the LEV. This suppression of the vortex release prevents the massive, large-scale detachment seen in the OGE condition, instead maintaining a clearance-controlled separation zone where the flow remains accelerated through the narrow gap.

Furthermore, at this higher reduced frequency $k = 0.20$, the PTV fields show that the suction is maintained not by a transient vortex passage, but by the diffuser effect resulting from the high-speed flow at the throat. The absence of a sharp DSV shedding event on the upstroke (Figure 6.27) confirms that the ground-effect suppresses the global load collapse. This is the primary physical mechanism behind the increased aerodynamic damping identified in Figure 6.22; by replacing the abrupt, energy-extracting vortex shedding with a geometrically-constrained acceleration, the system becomes significantly more stable. This mechanism essentially forces the flow to remain geometrically attached through the constraint of the ground boundary.

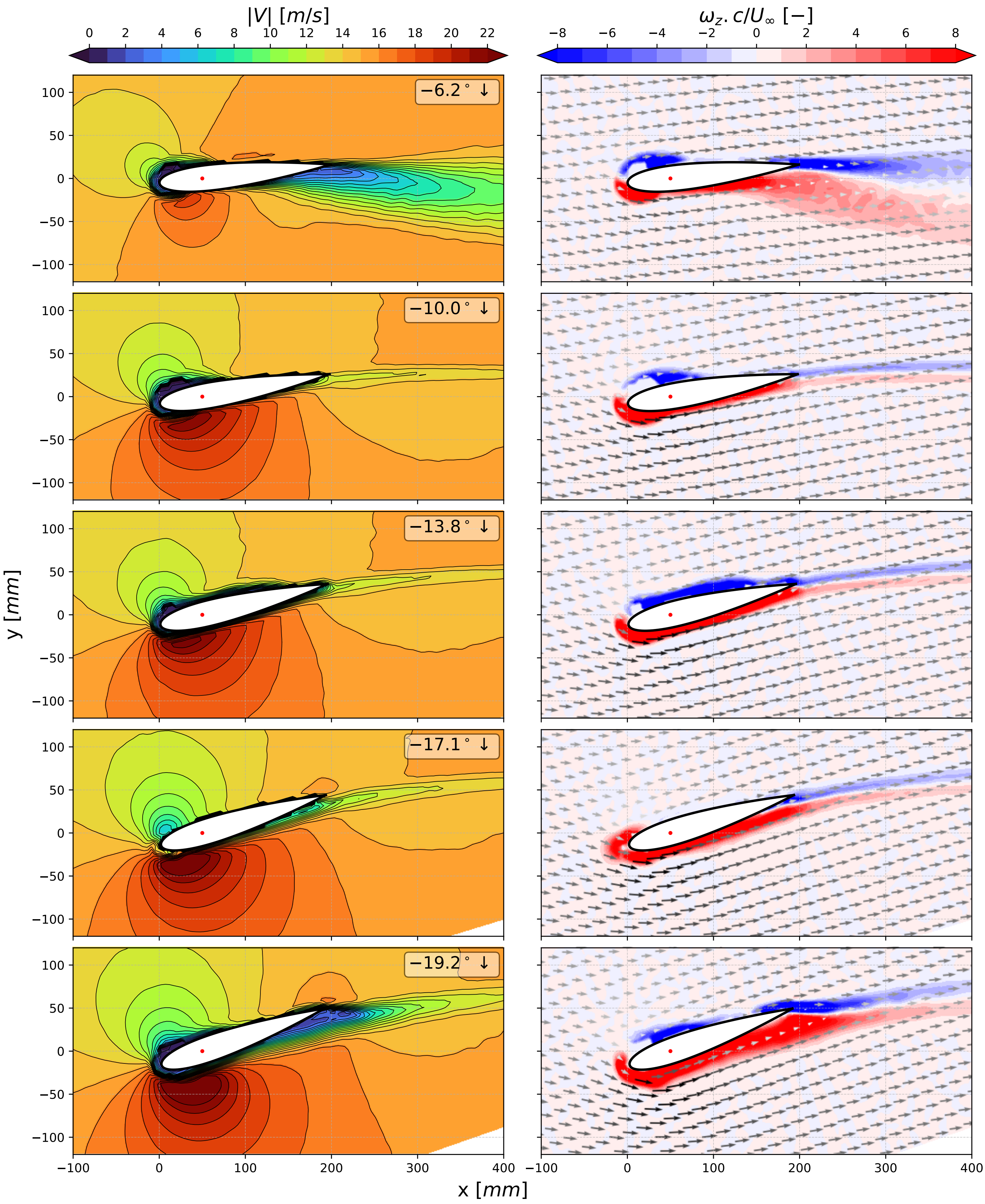

Figure 6.24: Phase-resolved PTV fields for the downstroke cycle of $H \to \infty$ and $k = 0.10$: (left) Absolute velocity magnitude $|V|$. (right) Non-dimensional vorticity $\omega_z c/U_\infty$ ($\omega_z = dv/dx - du/dy$).

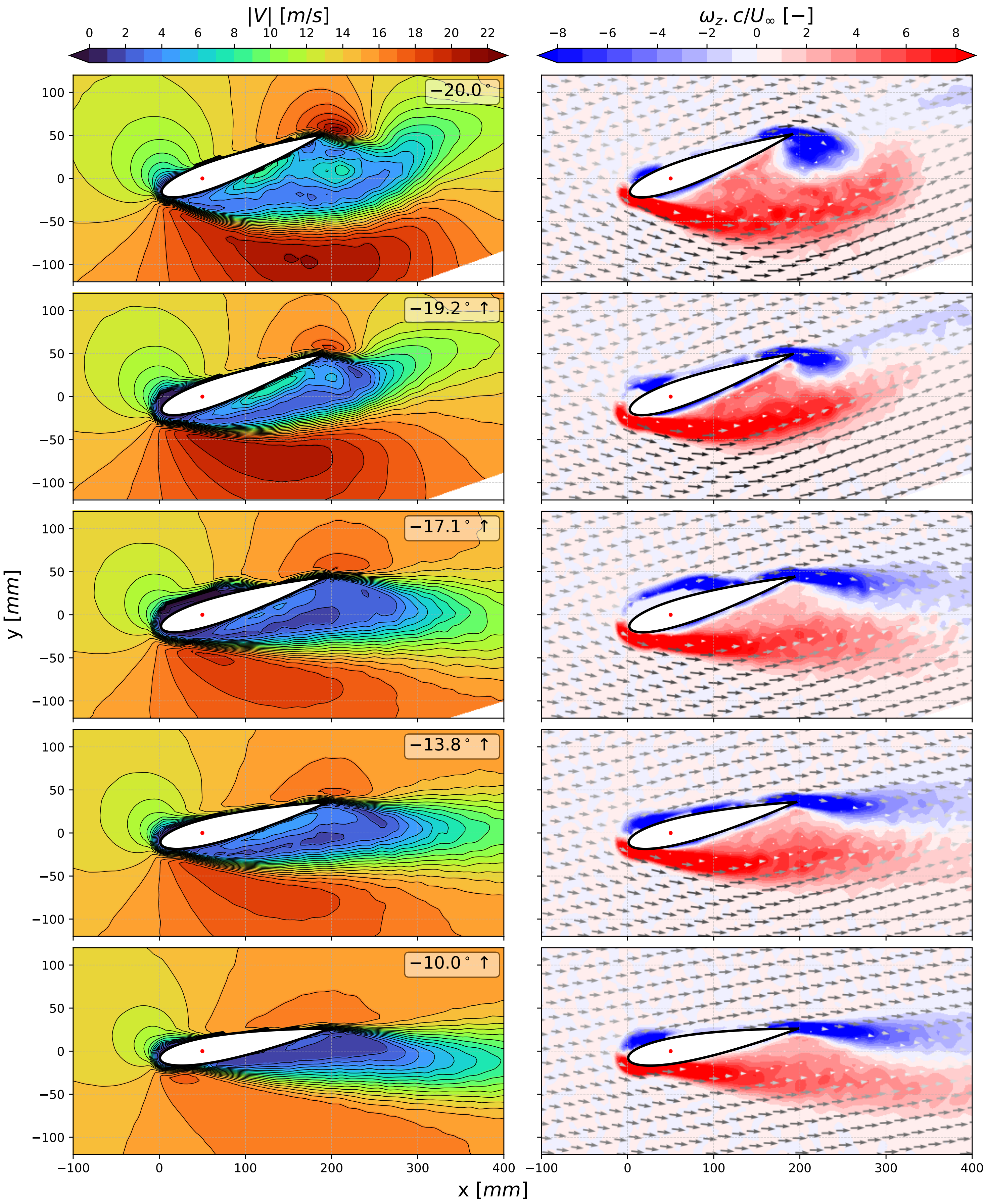

Figure 6.25: Phase-resolved PTV fields for the upstroke cycle of $H \to \infty$ and $k = 0.10$: (left) Absolute velocity magnitude $|V|$. (right) Non-dimensional vorticity $\omega_z c/U_\infty$ ($\omega_z = dv/dx - du/dy$).

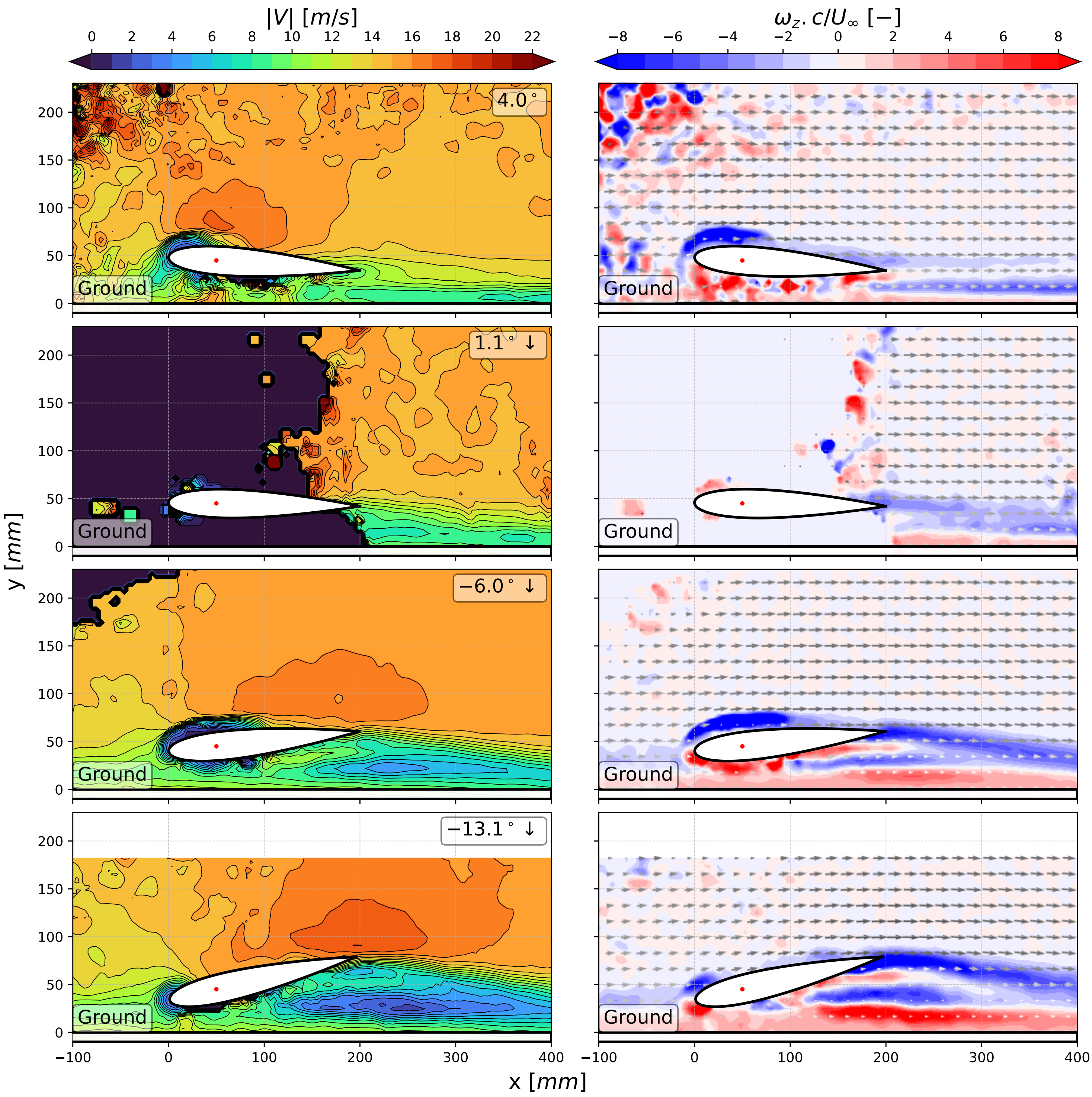

Figure 6.26: Phase-resolved PTV fields for the downstroke cycle of $H = 0.2$ and $k = 0.20$: (left) Absolute velocity magnitude $|V|$. (right) Non-dimensional vorticity $\omega_z c/U_\infty$ ($\omega_z = dv/dx - du/dy$).

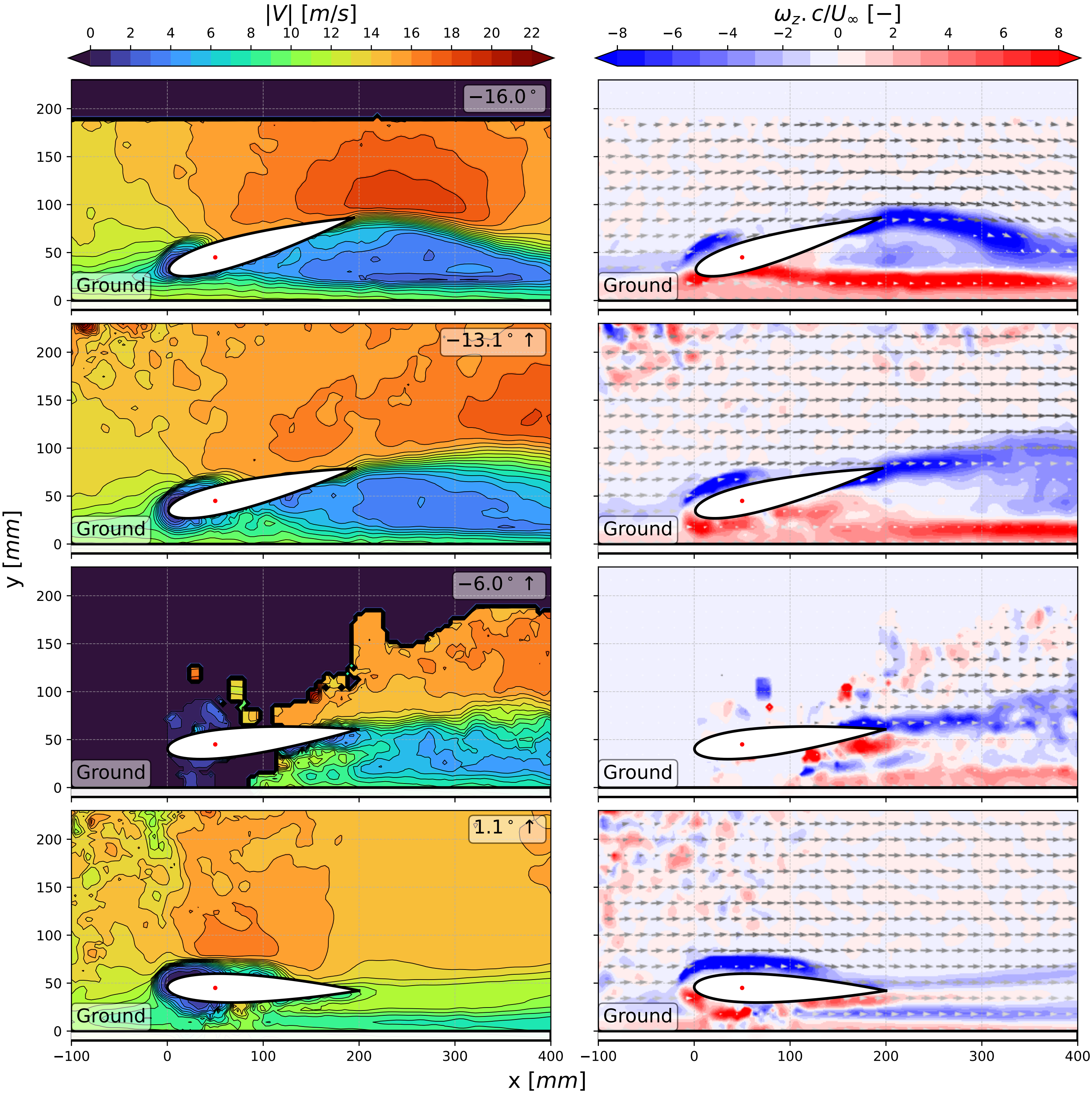

Figure 6.27: Phase-resolved PTV fields for the upstroke cycle of $H = 0.2$ and $k = 0.20$: (left) Absolute velocity magnitude $|V|$. (right) Non-dimensional vorticity $\omega_z c/U_\infty$ ($\omega_z = dv/dx - du/dy$).

Positive Stall

The unsteady aerodynamic response for the positive dynamic stall domain is evaluated through C_ℓ hysteresis loops, phase-averaged surface C_P contours, and phase-resolved PTV flow fields. To elucidate the coupling between kinematic rate and ground proximity, results are synthesised across a spectrum of $k = [0.05, 0.10, 0.15, 0.20]$ and selected clearances $H = [0.4, 0.6, 1.0, \infty]$. The motion is a harmonic pitch about the quarter-chord point defined by $\alpha(t) = 6^\circ + 10^\circ \sin \omega t$ for finite H and $\alpha(t) = 10^\circ + 10^\circ \sin \omega t$ for OGE.

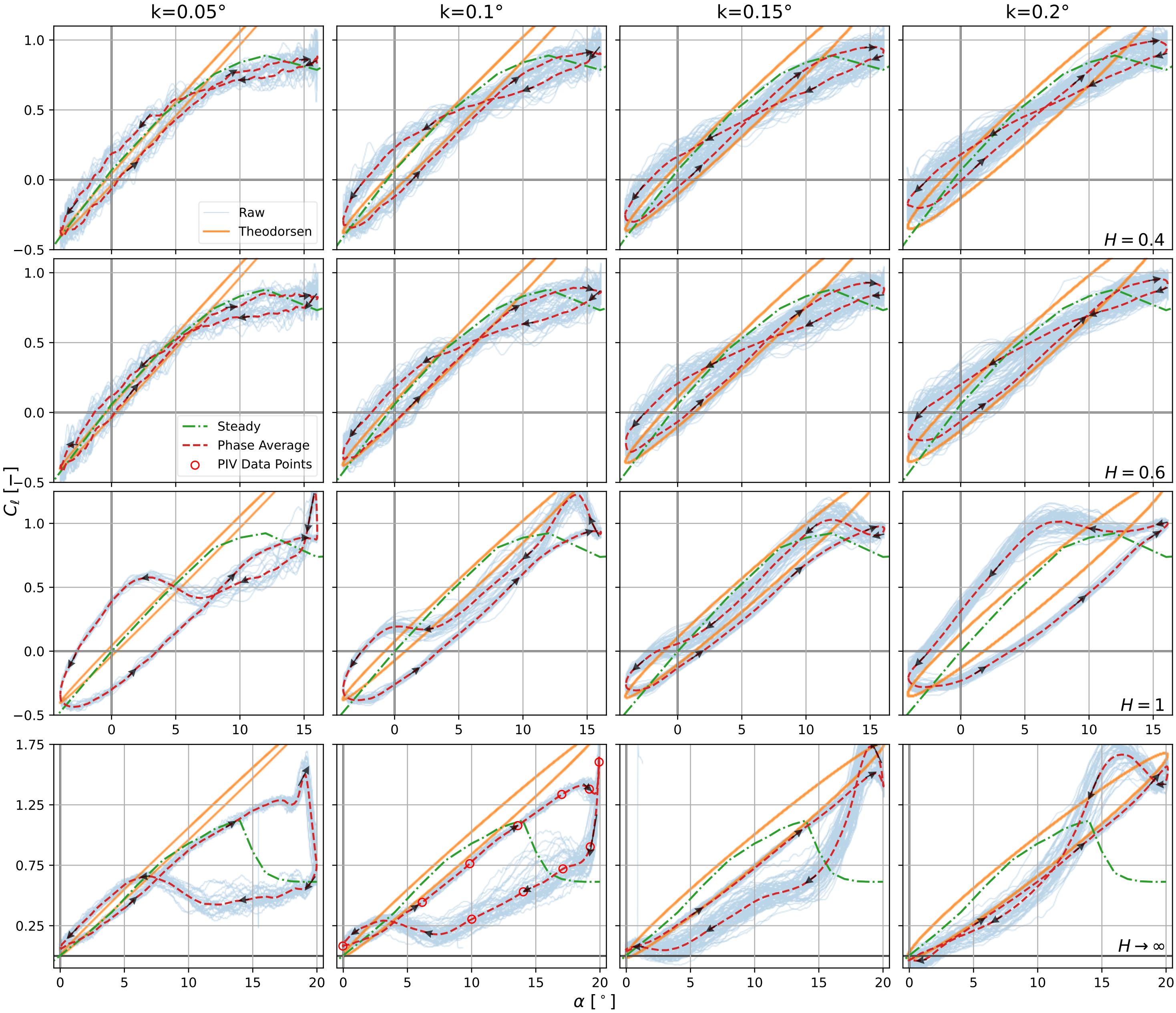

Figure 6.28: C_ℓ vs α for at various heights H (top to bottom): $[0.4, 0.6, 1.0, \infty]$ and reduced frequency k (left to right): $[0.05, 0.10, 0.15, 0.20]$.

The data in Figure 6.28 and Figure 6.29 reveal two dominant trends: a progressive increase in unsteady phase lag with higher k, and a systematic transition in flow topology as H increases. At $H = 0.4$ and 0.6, the C_P maps indicate a near-complete suppression of a propagating LEV. Instead of a concentrated suction core, the maps show a spatially distributed suction field that evolves gradually along the chord. In this domain, C_ℓ reaches its maximum just prior to the maximum AoA, followed immediately by a subtle DSV ejection.

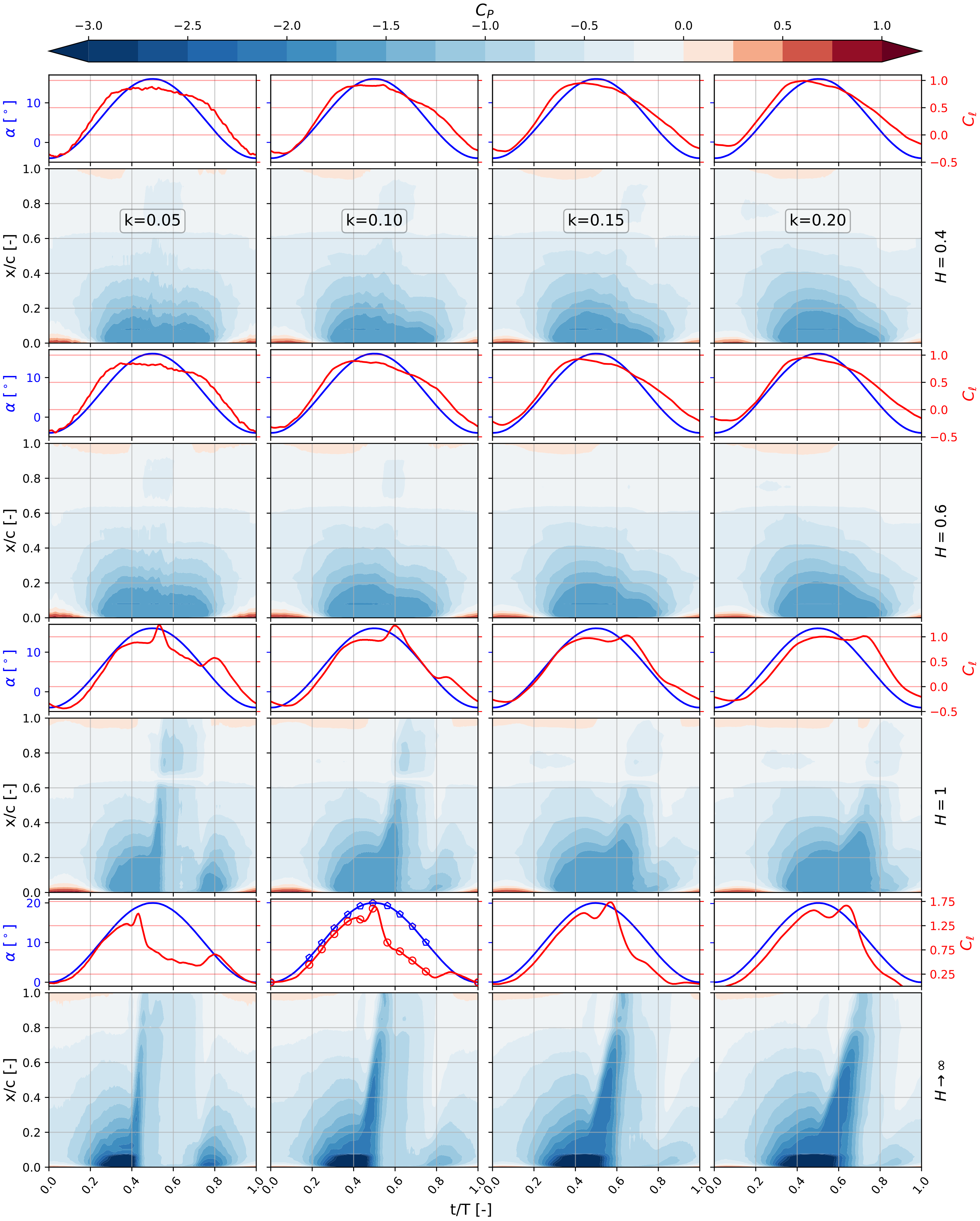

Figure 6.29: α, C_ℓ, and C_P contour over x/c vs t/T map at various heights H (top to bottom): $[0.4, 0.6, 1.0, \infty]$ and reduced frequency k (left to right): $[0.05, 0.10, 0.15, 0.20]$.

Unlike the attached flow cases where C_ℓ continued to rise post-maximum AoA due to non-circulatory effects and the negative stall case where geometric confinement suppresses discrete LEV shedding, the ground effect here forces a lift plateau. Some evidence of a LEV release appears near $x/c \simeq 0.8$ and $t/T \simeq 0.5$, where a localised low-pressure region suggests that ground proximity causes the flow to spill once the AoA threshold is met. This introduces an aerodynamic blockage between the airfoil and the ground, accelerating the wake convective velocity and preventing the leading-edge shear layer from completing a full vortex roll-up—the process where separated vorticity coils into a discrete, high-energy core.

At $H = 1$, the response transitions towards the OGE limit. At $k = 0.05$ and 0.10, a significant lift overshoot develops on the upstroke, followed by a sharp drop in C_ℓ on the downstroke as the DSV sheds. The subsequent small C_ℓ bump indicates flow reattachment as the AoA decreases. At higher k, the DSV propagates faster across the chord, resulting in a more sustained C_ℓ during the upstroke-to-downstroke transition. The C_P maps confirm this by showing a concentrated suction core translating downstream, a classical signature of a convecting DSV along the suction surface.

Increasing the reduced frequency further modifies this behaviour. As k increases, the stall event is progressively delayed relative to the instantaneous AoA. The upstroke branch of the $C_\ell - \alpha$ loops remains closer to the attached-flow trend for longer, indicating that the increasing pitch rate delays the growth and detachment of the LEV. Consequently, the peak lift occurs at a higher instantaneous incidence, and the vortex convection phase occupies a larger portion of the oscillation cycle. The C_P maps illustrate this effect through the downstream shift of the low-pressure core and the later appearance of the strongest suction region within the cycle.

The OGE configuration exhibits the most pronounced dynamic stall features, partly due to the higher peak AoA used in these cases. The hysteresis loops display a highly non-linear upstroke branch followed by a deep, delayed recovery on the downstroke, indicating a sustained period of separated flow after the vortex has convected away from the airfoil. This behaviour corresponds directly to the C_P contours, which show a coherent suction structure originating at the leading edge and travelling aft across the chord before detaching into the wake. The persistence of this structure explains the large lift overshoot observed in the hysteresis loops prior to the collapse in C_ℓ.

Another important difference between the IGE and OGE configurations is the recovery process during the downstroke. In the OGE condition, the lift remains depressed over a larger portion of the cycle, indicating a longer aerodynamic memory associated with the separated wake. In contrast, the IGE configurations recover more gradually once the angle of attack decreases, suggesting that the presence of the wall constrains the separated region and promotes earlier reattachment. This difference further emphasises that ground proximity modifies not only the formation of the stall vortex but also the subsequent reattachment dynamics.

Overall, these results suggest that the ground effect acts as a damping or suppressing mechanism for coherent vortex formation. By altering the convective environment and imposing a rigid boundary, the ground limits the spatial volume required for the leading-edge shear layer to roll up into a DSV. Consequently, the unsteady response in extreme ground effect is dominated by phase lag and convective delay rather than the non-linear lift excursions associated with discrete vortex convection.

7

Conclusion

This thesis has presented an experimental investigation into the steady and unsteady aerodynamics of a two-dimensional NACA0015 airfoil operating in ground effect. By combining surface pressure measurements with phase-resolved $3D$ particle tracking velocimetry ($3D-PTV$), the study has examined how proximity to a rigid ground plane modifies lift generation, flow separation, and dynamic stall behaviour across a range of angles of attack, reduced frequencies, and non-dimensional ground clearances. The central objective has been to clarify the physical mechanisms governing unsteady aerodynamic behaviour near a wall and to assess the applicability of classical unsteady aerodynamic theory under such conditions.

The steady-flow results demonstrate that the influence of ground effect is non-monotonic in nature. While moderate clearances generally enhance lift by suppressing suction-side separation and reducing downwash, close ground proximity ($H < 0.6$) introduces dominant viscous interactions between the airfoil and ground boundary layers. These interactions limit gap acceleration and induce pressure-side blockage, effectively capping circulation growth in a manner that classical inviscid models fail to predict.

In the unsteady domain, the lift response exhibits significant hysteresis and phase lag as the reduced frequency (k) increases. A key finding of this work is that ground proximity serves as a critical modulator of this response:

- **Attached Flow:** At intermediate clearances, the Venturi-driven acceleration beneath the airfoil increases the wake propagation speed, thereby reducing convective time lag and "compressing" the lift hysteresis loops.
- **Dynamic Stall:** Ground effect acts as a stabilising mechanism by suppressing the roll-up and "lift-off" of coherent dynamic stall vortices (DSVs). In extreme ground effect, the DSV is effectively "pinned" to the surface, replacing abrupt load collapses with a clearance-controlled separation that increases aerodynamic damping.
- **Extreme Proximity:** At very low clearances ($H = 0.2$), physical confinement and viscous blockage hinder wake shedding, leading to a substantial increase in phase lag and a subsequent widening of the hysteresis loops.

Ultimately, these findings demonstrate that reduced frequency alone is insufficient to characterise unsteady stall in ground proximity; instead, the non-dimensional height must be considered a primary kinematic parameter. These insights have direct implications for the design of high-performance racing cars—particularly regarding the management of porpoising instabilities and active aerodynamics—and the development of low-altitude unmanned aerial vehicles where wing-ground interactions dominate the operational envelope. Future work should expand these investigations to higher Reynolds numbers to further test the robustness of the observed viscous-confinement thresholds.

7.1. Recommendations for Future Work

1. **High-range pressure instrumentation:** The implementation of higher-range pressure transducers is recommended to accurately capture the full magnitude of suction peaks occurring near the leading edge under conditions of extreme ground effect.
2. **Investigation of Reynolds number sensitivity:** Future studies should perform a Reynolds number sweep to determine whether viscous-confinement thresholds—the transition point from Venturi acceleration to flow blockage—shift as the boundary layer becomes more energetic and resistant to separation.
3. **Implementation of a moving ground plane:** Utilising a rolling-road system would eliminate the ground-plane boundary layer. This would more accurately simulate the operating conditions of a race car or a low-flying aircraft by removing the relative motion between the air and the ground, thereby eliminating the parasitic viscous interaction between the airfoil and a stationary wall boundary layer.
4. **Three-dimensional effects and finite-span dynamics:** An investigation into finite wings with varying aspect ratios in ground effect is proposed. Understanding the interaction between tip vortices and the ground boundary layer would provide more practical insights for real-world aerodynamic surfaces, which are rarely infinite in span.
5. **Multi-element and high-lift configurations:** Further research should investigate multi-element wings consisting of a main plane and flap. In ground proximity, the interaction between these elements and the ground often leads to flow ”choking” within the diffuser-like region; this phenomenon could be further interrogated using $3D - PTV$ to map the complex off-body vorticity.

References

[1] Ray Hennessy. *Low Gliding Brown Pelican*. Accessed: 2026-02-04. Feb. 2020. URL: https://www.rayhennessy.com/blog/2020/2/14/low-gliding-brown-pelican.

[2] T. Lee and G. Lin. “Review of experimental investigations of wings in ground effect at low Reynolds numbers”. In: *Frontiers in Aerospace Engineering* 1 (Nov. 2022). DOI: 10.3389/fpace.2022.975158.

[3] Xinyue Kan et al. “Analysis of ground effect for small-scale uavs in forward flight”. In: *IEEE Robotics and Automation Letters* 4.4 (2019), pp. 3860–3867.

[4] Wigetworks Pte Ltd. *Wigetworks*. 2004. URL: https://wigetworks.com/ (visited on 27/03/2026).

[5] U.S. Department of War. *Department of War Support to the Southern Border (Photo)*. Source: U.S. Department of War, 2026, photo ID 2003059317. 2026. URL: https://www.war.gov/Spotlights/DOW-Support-to-the-Southern-Border/Photos/igphoto/2003059317/ (visited on 27/03/2026).

[6] K Jones et al. “A numerical and experimental investigation of flapping-wing propulsion in ground effect”. In: *40th AIAA Aerospace Sciences Meeting & Exhibit*. 2002, p. 866.

[7] Zhenlong WU et al. “Hovering rotor aerodynamics in extreme ground effect”. In: *Chinese Journal of Aeronautics* 37.7 (July 2024), pp. 204–219. ISSN: 10009361. DOI: 10.1016/j.cja.2024.02.020.

[8] Kirill V Rozhdestvensky. *Aerodynamics of a lifting system in extreme ground effect*. Springer Science & Business Media, 2013.

[9] Yair Moryossef and Yuval Levy. “Effect of oscillations on airfoils in close proximity to the ground”. In: *AIAA journal* 42.9 (2004), pp. 1755–1764.

[10] Juan Molina, Xin Zhang and Antoni Alomar. “Aerodynamics of a pitching and heaving airfoil in ground effect”. In: *AIAA Journal* 54.4 (2016), pp. 1158–1171.

[11] D Clements and K Djidjeli. “Periodic morphing of a NACA6409 aerofoil in ground effect, its wake mechanisms and thrust generation”. In: *The Aeronautical Journal* 128.1330 (2024), pp. 2924–2944.

[12] Formula 1. *The origins of ground effect*. 2022. URL: https://www.formula1.com/en/latest/article/watch-the-origins-of-ground-effect.6i1MZBs5xe6cjO2deb57hV (visited on 29/09/2025).

[13] Fédération Internationale de l’Automobile. *Formula 1 Technical Regulations – 2022 (Issue 11)*. Accessed: 2025-09-29. Apr. 2022. URL: https://api.fia.com/sites/default/files/formula_1_-_technical_regulations_-_2022_-_iss_11_-_2022-04-29.pdf.

[14] Formula One Group. *Screenshots from F1 TV broadcast*. 2024. URL: https://f1tv.formula1.com/ (visited on 27/03/2026).

[15] Fédération Internationale de l’Automobile. *Formula One Technical Regulations – 2026 (Issue 15)*. Accessed: 2026-01-28. Dec. 2025. URL: https://www.fia.com/system/files/documents/fia_2026_f1_regulations_-_section_c_technical_-_iss_15_-_2025-12-10_0.pdf.

[16] J.D. Anderson. *Fundamentals of Aerodynamics*. 6th ed. McGraw-Hill, 2020.

[17] Joseph Katz and Allen Plotkin. *Low-speed aerodynamics*. Vol. 13. Cambridge university press, 2001.

[18] Joseph Katz. *Aerodynamics of race cars*. Annual Reviews, 2006.

[19] Xin Zhang and Jonathan Zerihan. “Off-surface aerodynamic measurements of a wing in ground effect”. In: *Journal of Aircraft* 40.4 (2003), pp. 716–725.

[20] A Komrakova et al. “On the Origin of the Ground Effect”. In: *Okanagan Fluid Dynamics Meeting* (Apr. 2019).

[21] M. R. Ahmed, T. Takasaki and Y. Kohama. “Aerodynamics of a NACA4412 airfoil in ground effect”. In: *AIAA Journal* 45.1 (Jan. 2007), pp. 37–47. ISSN: 00011452. DOI: 10.2514/1.23872.

[22] Jonathan W. Vogt and Tracie J. Barber. “Ground effect phenomena about lift and downforce generating cambered aerofoils”. In: *International Journal of Numerical Methods for Heat and Fluid Flow* 22.2 (2012), pp. 153–174. ISSN: 09615539. DOI: 10.1108/09615531211199809.

[23] Ravindra A. Shirsath and Rinku Mukherjee. “Experimental and computational investigations of aerodynamic characteristics of a finite rectangular wing-in-ground effect”. In: *Proceedings of the Institution of Mechanical Engineers, Part G: Journal of Aerospace Engineering* 237.5 (Apr. 2023), pp. 1007–1024. ISSN: 20413025. DOI: `10.1177/09544100221114700`.

[24] Md Aminul Islam Sobuj et al. *Numerical Investigation of Ground Effect on Airfoil*. English. Tech. rep. Dhaka: Khulna University of Engineering & TEchnology, Dec. 2023. URL: `https://ssrn.com/abstract=4859605`.

[25] Jonathan Vogt, Tracie Barber and Erica Leonardi. *Flow Field Phenomena about Lift and Downforce Generating Cambered Aerofoils in Ground Effect*. Tech. rep. 2007. URL: `https://www.researchgate.net/publication/43472413`.

[26] Ülgen Gülçat. *Fundamentals of modern unsteady aerodynamics*. Vol. 2010. Springer, 2010.

[27] Theodore Theodorsen. *General Theory of Aerodynamic Instability and the Mechanism of Flutter*. NACA Technical Report NACA-TR-496. Document ID 19930090935, Accession Number 93R20225. Langley Field, VA, United States: National Advisory Committee for Aeronautics, Langley Aeronautical Laboratory, 1949. URL: `https://ntrs.nasa.gov/citations/19930090935`.

[28] Herbert Wagner. *Über die Entstehung des dynamischen Auftriebes von Tragflügeln*. ger. Berlin: VDI-Verl., 1925. URL: `http://eudml.org/doc/204029`.

[29] R. Fernandez-Feria and E. Sanmiguel-Rojas. “Comparison of aerodynamic models for two-dimensional pitching foils with experimental data”. In: *Physics of Fluids* 31.5 (May 2019). ISSN: 10897666. DOI: `10.1063/1.5096337`.

[30] Chang-kwon Kang et al. “Fluid dynamics of pitching and plunging airfoils of Reynolds number between 1× 10^ 4 and 6× 10^ 4”. In: *47th AIAA aerospace sciences meeting including the new horizons forum and aerospace exposition*. 2009, p. 536.

[31] William J McCroskey. *The phenomenon of dynamic stall*. Tech. rep. NASA, 1981.

[32] David R. Williams et al. “Dynamic hysteresis control of lift on a pitching wing”. In: *Experiments in Fluids* 56.5 (May 2015). ISSN: 07234864. DOI: `10.1007/s00348-015-1982-y`.

[33] Abbas Daliri, MJ Maghrebi and MR Soltani. “Experimental assessment of Theodorsen’s function for uncoupled pitch–plunge motion”. In: *Physics of Fluids* 35.3 (2023).

[34] T. Lee et al. “Impact of ground proximity on the aerodynamic properties of an unsteady airfoil”. In: *Proceedings of the Institution of Mechanical Engineers, Part G: Journal of Aerospace Engineering* 232.10 (Aug. 2018), pp. 1814–1830. ISSN: 20413025. DOI: `10.1177/0954410017703416`.

[35] Richard CC Chung et al. “Ground-induced suppression of chaos in the self-excited flow behind a plunging airfoil”. In: *Physics of Fluids* 36.3 (2024).

[36] Marvin Alan Jones. *Mechanisms in Wing-In-Ground Effect Aerodynamics*. Tech. rep. University College London, Nov. 1999.

[37] Jose Vanir Valenzuela and Timothy Takahashi. “Wing Design Strategies for Vehicles Designed to Operate in Ground Effect”. In: *AIAA SciTech Forum and Exposition, 2024*. American Institute of Aeronautics and Astronautics Inc, AIAA, 2024. ISBN: 9781624107115. DOI: `10.2514/6.2024-0003`.

[38] M. R. Ahmed and S. D. Sharma. “An investigation on the aerodynamics of a symmetrical airfoil in ground effect”. In: *Experimental Thermal and Fluid Science* 29.6 (July 2005), pp. 633–647. ISSN: 08941777. DOI: `10.1016/j.expthermflusci.2004.09.001`.

[39] Jonathan Zerihan and Xin Zhang. “Aerodynamics of a single element wing in ground effect”. In: *Journal of Aircraft* 37.6 (2000), pp. 1058–1064. ISSN: 00218669. DOI: `10.2514/2.2711`.

[40] Amin Mivehchi, Jason Dahl and Stephen Licht. “Heaving and pitching oscillating foil propulsion in ground effect”. In: *Journal of Fluids and Structures* 63 (2016), pp. 174–187.

[41] Jian-Tao Zhang and Takashi Nakamura. “Propulsive performance of a heaving and pitching foil with large amplitudes in unsteady ground effect”. In: *Fluid Dynamics Research* 56.4 (2024), p. 045503.

[42] Yongcheng Li, Ziying Pan and Nan Zhang. “Numerical analysis on the propulsive performance of oscillating wing in ground effect”. In: *Applied Ocean Research* 114 (2021), p. 102772.

[43] Juan Molina and Xin Zhang. “Aerodynamics of a heaving airfoil in ground effect”. In: *AIAA journal* 49.6 (2011), pp. 1168–1179.

[44] Juan Molina, Xin Zhang and David Angland. “On the unsteady motion and stability of a heaving airfoil in ground effect”. In: *Acta Mechanica Sinica* 27 (2011), pp. 164–178.

[45] M Hadi Doolabi, M Bakhtiarifar and H Sadati. “Experimental Study of Airfoil Aerodynamic Behavior under Oscillating Motion in Ground Effect”. In: *Journal of Applied Fluid Mechanics* 17.11 (2024), pp. 2411–2423.

[46] Fulvio Scarano. “Tomographic PIV: principles and practice”. In: *Measurement Science and Technology* 24.1 (2013), p. 012001.

[47] Klaus D Hinsch. “Three-dimensional particle velocimetry”. In: *Measurement Science and Technology* 6.6 (1995), pp. 742–753.

[48] Markus Raffel et al. *Particle image velocimetry: a practical guide*. springer, 2018.

[49] W Terra, A Sciacchitano and F Scarano. “Aerodynamic drag of a transiting sphere by large-scale tomographic-PIV”. In: *Experiments in Fluids* 58.7 (2017), p. 83.

[50] David Engler Faleiros et al. “Helium-filled soap bubbles tracing fidelity in wall-bounded turbulence”. In: *Experiments in fluids* 59.3 (2018), p. 56.

[51] Matteo Novara and Fulvio Scarano. “A particle-tracking approach for accurate material derivative measurements with tomographic PIV”. In: *Experiments in fluids* 54.8 (2013), p. 1584.

[52] Delft University of Technology. *Open Jet Facility*. 2009. URL: `https://www.tudelft.nl/lr/organisatie/afdelingen/flow-physics-and-technology/facilities/low-speed-wind-tunnels/open-jet-facility` (visited on 27/06/2025).

[53] LEM Lignarolo et al. “Experimental analysis of the wake of a horizontal-axis wind-turbine model”. In: *Renewable Energy* 70 (2014), pp. 31–46.

[54] Mark Drela. “XFOIL: An Analysis and Design System for Low Reynolds Number Airfoils”. In: *Low Reynolds Number Aerodynamics*. Ed. by Thomas J. Mueller. Springer Berlin Heidelberg, 1989, pp. 1–12. DOI: `10.1007/978-3-642-84010-4_1`.

[55] Martin Hepperle. *JavaFoil - Analysis of Airfoils*. Version 2.29. Jan. 2020. URL: `https://www.mh-aerotools.de/airfoils/javafoil.htm`.

[56] Stephen J Kline. “Describing uncertainties in single-sample experiments”. In: *Mech. Eng.* 75 (1963), pp. 3–8.

A

Pressure Tap Locations

Out of Ground					In Ground			
Channel	**SN**	**x [mm]**	**y [mm]**		**Channel**	**SN**	**x [mm]**	**y [mm]**
1	1	0.00	0.00		1	1	0.00	0.00
2	2	1.00	2.99		2	2	1.00	2.99
3	3	2.00	4.28		3	3	2.00	4.28
4	4	4.00	5.91		4	4	4.00	5.91
5	5	6.00	7.10		5	5	6.00	7.10
6	6	8.00	8.07		6	6	8.00	8.07
7	7	10.00	8.89		7	7	10.00	8.89
8	8	12.00	9.59		8	8	12.00	9.59
9	33	0.00	0.00		9	9	16.00	10.77
10	34	1.00	-2.99		10	10	20.00	11.71
11	35	2.00	-4.28		11	11	25.00	12.64
12	36	4.00	-5.91		12	12	30.00	13.36
13	37	6.00	-7.10		13	13	35.00	13.92
14	38	8.00	-8.07		14	14	40.00	14.34
15	39	10.00	-8.89		15	15	45.00	14.65
16	40	12.00	-9.59		16	16	50.00	14.85
17	9	16.00	10.77		17	33	0.00	0.00
18	10	20.00	11.71		18	34	1.00	-2.99
19	11	25.00	12.64		19	35	2.00	-4.28
20	12	30.00	13.36		20	36	4.00	-5.91
21	13	35.00	13.92		21	37	6.00	-7.10
22	14	40.00	14.34		22	38	8.00	-8.07
23	15	45.00	14.65		23	39	10.00	-8.89
24	16	50.00	14.85		24	40	12.00	-9.59
25	41	16.00	-10.77		25	41	16.00	-10.77
26	42	20.00	-11.71		26	42	20.00	-11.71
27	43	25.00	-12.64		27	43	25.00	-12.64
28	44	30.00	-13.36	← P_{ref} →	28	44	30.00	-13.36
29	45	35.00	-13.92		29	45	35.00	-13.92
30	46	40.00	-14.34		30	46	40.00	-14.34
31	47	45.00	-14.65		31	47	45.00	-14.65
32	48	50.00	-14.85		32	48	50.00	-14.85
33	17	55.00	14.97		33	17	55.00	14.97
34	18	60.00	15.00		34	18	60.00	15.00
35	19	70.00	14.87		35	19	70.00	14.87
36	20	80.00	14.50		36	20	80.00	14.50
37	21	90.00	13.94		37	21	90.00	13.94
38	22	100.00	13.22		38	22	100.00	13.22
39	23	110.00	12.35		39	23	110.00	12.35
40	24	120.00	11.37	← null →	40	24	120.00	11.37

Out of Ground					In Ground			
Channel	**SN**	**x [mm]**	**y [mm]**		**Channel**	**SN**	**x [mm]**	**y [mm]**
41	49	55.00	-14.97		41	49	55.00	-14.97
42	50	60.00	-15.00		42	50	60.00	-15.00
43	51	70.00	-14.87		43	51	70.00	-14.87
44	52	80.00	-14.50		44	52	80.00	-14.50
45	53	90.00	-13.94		45	53	90.00	-13.94
46	54	100.00	-13.22		46	54	100.00	-13.22
47	55	110.00	-12.35		47	55	110.00	-12.35
48	56	120.00	-11.37		48	56	120.00	-11.37
49	25	130.00	10.28		49	25	130.00	10.28
50	26	140.00	0.00	$\leftarrow$ P_0 $\rightarrow$	50	26	140.00	0.00
51	27	150.00	7.80	null $\rightarrow$	51	27	150.00	7.80
52	28	160.00	6.43		52	28	160.00	6.43
53	29	170.00	4.97		53	29	170.00	4.97
54	30	180.00	3.41		54	30	180.00	3.41
55	31	190.00	1.76		55	31	190.00	1.76
56	32	200.00	0.00	$\leftarrow$ P_∞ $\rightarrow$	56	32	200.00	0.00
57	57	130.00	-10.28		57	57	130.00	-10.28
58	58	140.00	-9.08		58	58	140.00	-9.08
59	59	150.00	-7.80		59	59	150.00	-7.80
60	60	160.00	-6.43		60	60	160.00	-6.43
61	61	170.00	-4.97		61	61	170.00	-4.97
62	62	180.00	-3.41		62	62	180.00	-3.41
63	63	190.00	-1.76		63	63	190.00	-1.76
64	64	200.00	0.00		64	64	200.00	0.00

B
Uncertainty

B.1. Sources of Experimental Error

The primary sources of uncertainty in the measured and derived quantities are summarized in Table B.1. These values are based on manufacturer specifications and calibration procedures conducted in the OJF at Delft.

Table B.1: Uncertainty budget for the lift coefficient (C_ℓ) at representative flow conditions, accounting for a 0.05% Full Scale instrument accuracy across ± 200 Pa and ± 750 Pa sensor ranges.

	Near Stall ($\alpha = -16°$)		**Attached Flow ($\alpha = 8°$)**		**Near Stall ($\alpha = 16°$)**	
H **[−]**	ω_{C_ℓ} **[−]**	ω_{C_ℓ}/C_ℓ **[%]**	ω_{C_ℓ} **[−]**	ω_{C_ℓ}/C_ℓ **[%]**	ω_{C_ℓ} **[−]**	ω_{C_ℓ}/C_ℓ **[%]**
0.1	0.0142	1.93	0.0017	0.44	N/A	N/A
0.2	0.0227	1.79	0.0026	0.57	N/A	N/A
0.4	0.0254	1.81	0.0029	0.62	0.0080	1.02
0.6	0.0224	1.85	0.0028	0.61	0.0072	0.99
0.8	0.0212	1.98	0.0026	0.52	0.0089	0.99
1.0	0.0178	1.95	0.0021	0.49	0.0071	0.96
∞	0.0243	2.55	0.0139	3.86	0.0214	3.11

**Note: Values are derived from the jitter-analysis of the raw pressure data using the Kline-McClintock method (Root sum squared) [56].*

B.2. Numerical Integration Bias

The use of the trapezoidal rule for pressure integration introduces a systematic numerical bias. This bias arises from the linear approximation between discrete pressure taps, which can under-resolve the high-curvature suction peaks near the leading edge. To quantify this effect, the trapezoidal integration of the normal force coefficient (C_n) was compared against a higher-order cubic spline reconstruction of the pressure distribution. For the most critical case of $\alpha = -20°$ and $16°$, where pressure gradients are maximum, the numerical integration bias was found to be a maximum of $\pm$ **[0.5%]**. This indicates that the current tap density is sufficient to capture the aerodynamic loads with high fidelity, and the resulting error is within the acceptable limits for experimental airfoil studies.

B.3. Volumetric Velocimetry Uncertainty

The uncertainty in the off-body flow fields was evaluated based on the calibration residuals and the Shake-the-Box (STB) tracking fidelity. The average reconstruction deviation across the ten-camera system was **0.362 pixels**. For a typical particle displacement of 10 pixels between successive frames, this reconstruction noise corresponds to an instantaneous velocity uncertainty of approximately **3.62%** of the local velocity. Because the results presented in this thesis are phase-averaged over $N = 100$ cycles, the random error is significantly attenuated. The resulting velocity noise floor is estimated at approximately **0.36%** of the free-stream velocity (U_∞).

C

3D-PTV and Shake-the-Box Parameters

The off-body flow measurements were conducted using a high-speed 3D Particle Tracking Velocimetry (3D-PTV) system. This appendix details the hardware specifications and the numerical parameters used for the Shake-the-Box (STB) Lagrangian particle tracking algorithm.

C.1. Hardware and Optical Setup

The diagnostic system consisted of four high-speed cameras and a high-repetition-rate laser, synchronized via a programmable timing unit. The optical parameters are summarized in Table C.1.

Table C.1: Experimental hardware and optical configuration.

Parameter	**Value/Specification**
Cameras	$2 \times 5\times$ Imager LX
Sensor Resolution	1624 $\times$ 1236 pixels
Pixel Size	$4.4\,\mu m$
Time between the double exposure	$400\,\mu s$
Exposure Time	$300\,\mu s$
Illumination	Double-Pulse LEDs

C.2. Seeding and Volume Configuration

The flow was seeded with Helium-Filled Soap Bubbles ($HFSB$) to ensure neutral buoyancy and high signal-to-noise ratio in the large-scale measurement volume.

- **Particle Type:** HFSB (diameter $\approx 40\,\mu m$).
- **Seeding Density:** $\approx$ 0.006 particles per pixel (ppp).
- **Measurement Volume:** $X \times Y \times Z$ mm ($600 \times 400 \times 300$ mm).
- **Voxel Size:** $0.52\,mm/voxel$.

C.3. Shake-the-Box (STB) Processing

The Lagrangian tracks were reconstructed using the DaVis 11 STB algorithm. The processing parameters used to achieve the final velocity fields are listed in Table C.2.

Table C.2: Shake-the-Box (STB) numerical processing parameters.

Parameter	**Setting/Value**
Algorithm	Shake-the-Box (DaVis 11)
OTF Calculation	Volume Self-Calibration (0.75 px residual)
STB Iterations	4 iterations

D

Tabulated Aerodynamic Coefficients

D.1. Steady-State Coefficients

Table D.1: Steady-state aerodynamic coefficients grouped by angle of attack ($Re \approx 2 \times 10^5$).

α [°]	H [−]	C_ℓ [−]	C_d [−]	C_m [−]
-20	0.1	-0.1288	0.0506	-0.0248
	0.2	-1.1707	0.7193	-0.1092
	0.4	-1.3666	0.8210	-0.1268
	0.6	-1.2791	0.6019	-0.0907
	0.8	-1.0663	0.3887	-0.0678
	1.0	-0.8626	0.2609	-0.0561
	∞	-0.5501	0.2557	-0.0010
-16	0.1	-0.7329	0.2528	-0.0460
	0.2	-1.2663	0.6465	-0.1016
	0.4	-1.4040	0.7702	-0.1263
	0.6	-1.2150	0.5633	-0.0949
	0.8	-1.0724	0.3607	-0.0697
	1.0	-0.9149	0.2424	-0.0577
	∞	-0.9519	0.0094	0.0101
-12	0.1	-0.8361	0.2310	-0.0446
	0.2	-1.2890	0.5121	-0.0844
	0.4	-1.2886	0.5652	-0.0962
	0.6	-1.2064	0.5422	-0.0926
	0.8	-1.1745	0.5250	-0.0880
	1.0	-1.1891	0.5390	-0.0910
	∞	-0.8558	0.0159	-0.0007
-10	0.1	-0.9055	0.2139	-0.0408
	0.2	-1.3237	0.4888	-0.0915
	0.4	-1.1302	0.4186	-0.0764
	0.6	-1.0906	0.4153	-0.0755
	0.8	-1.0712	0.4011	-0.0716
	1.0	-1.1069	0.4234	-0.0755
	∞	-0.7692	0.0263	-0.0052
-8	0.1	-0.8999	0.1639	-0.0355
	0.2	-1.0728	0.2653	-0.0537
	0.4	-0.9220	0.2642	-0.0570
	0.6	-0.9155	0.2673	-0.0572
	0.8	-0.9138	0.2530	-0.0542
	1.0	-0.9629	0.2812	-0.0585
	∞	-0.6333	0.0361	-0.0084
-4	0.1	-0.6697	0.0338	-0.0198
	0.2	-0.5624	0.0397	-0.0237
	0.4	-0.4081	0.0299	-0.0234
	0.6	-0.4263	0.0329	-0.0238
	0.8	-0.4003	0.0182	-0.0203
	1.0	-0.4759	0.0341	-0.0241
	∞	-0.2631	0.0424	-0.0073
0	0.1	-0.2011	-0.0344	-0.0065
	0.2	-0.0054	-0.0239	-0.0055
	0.4	0.0684	-0.0264	-0.0051
	0.6	0.0587	-0.0325	-0.0041
	0.8	0.0689	-0.0388	-0.0019
	1.0	-0.0015	-0.0403	-0.0040
	∞	0.0041	0.0407	-0.0017
4	0.1	0.3832	0.0457	-0.0000
	0.2	0.4567	0.0683	0.0009
	0.4	0.4626	0.0586	0.0011
	0.6	0.4573	0.0447	0.0031
	0.8	0.5032	0.0495	0.0050
	1.0	0.4315	0.0300	0.0038
	∞	0.3600	0.0350	0.0131
8	0.1[a]	0.6029	0.1342	0.0000
	0.2	0.7826	0.2397	-0.0032
	0.4	0.7561	0.2320	-0.0034
	0.6	0.7453	0.2218	-0.0010
	0.8	0.7994	0.2305	0.0005
	1.0	0.8104	0.2246	0.0013
	∞	0.7921	0.0158	0.0395
10	0.2	0.8716	0.3454	-0.0052
	0.4	0.8396	0.3404	-0.0081
	0.6	0.8315	0.3279	-0.0054
	0.8	0.8784	0.3379	-0.0044
	1.0	0.8878	0.3318	-0.0037
	∞	0.9301	0.0018	0.0517
12	0.2	0.9488	0.4554	-0.0069
	0.4	0.8891	0.4467	-0.0132
	0.6	0.8801	0.4300	-0.0097
	0.8	0.9109	0.4401	-0.0102
	1.0	0.9229	0.4349	-0.0095
	∞	1.0480	-0.0123	0.0646
16	0.2[b]	0.9825	0.4628	-0.0010
	0.4	0.7866	0.3622	-0.0147
	0.6	0.7318	0.3361	-0.0137
	0.8	0.8941	0.2800	-0.0053
	1.0	0.7373	0.1714	-0.0024
	∞	0.6864	0.2332	0.0387
20	0.4	0.9951	0.4638	-0.0129
	0.6	0.8464	0.3844	-0.0121
	0.8	0.9101	0.3163	-0.0063
	1.0	0.7614	0.2327	-0.0044
	∞	0.6134	0.2821	0.0369

[a] Data for $H = 0.1$ at $\alpha = 8.0°$ corresponds to measurement at $\alpha = 7.0°$.
[b] Data for $H = 0.2$ at $\alpha = 16.0°$ corresponds to measurement at $\alpha = 15.0°$.

D.2. Unsteady Hysteresis Parameters

The following table details the dynamic response parameters for the pitching airfoil. The aerodynamic damping (Ξ) is calculated as the area enclosed by the $C_\ell - \alpha$ hysteresis loop.

Table D.2: Unsteady aerodynamic parameters grouped by mean angle of attack and clearance ($Re \approx 2 \times 10^5$).

H [−]	α_0 [°]	k [−]	Max C_ℓ [−]	Damping (Ξ)
0.1	-4	0.05	-1.117	-0.0074
		0.10	-1.281	-0.0310
		0.15	-1.421	-0.0407
		0.20	-1.446	-0.0386
	0	0.05	0.713	0.0271
		0.10	0.712	0.0434
		0.15	0.712	0.0827
		0.20	0.699	0.0448
0.2	-10	0.05	-1.604	-0.0414
		0.10	-1.922	-0.0946
		0.15	-2.059	0.0048
		0.20	-2.186	-0.0661
	0	0.05	0.826	0.0399
		0.10	0.830	0.0553
		0.15	0.880	0.2125
		0.20	0.932	0.1580
	5	0.05	1.006	0.0117
		0.10	1.018	0.0911
		0.15	1.043	0.0752
		0.20	1.172	-0.0566
0.4	-6	0.05	-1.493	-0.0458
		0.10	-1.534	0.0338
		0.15	-1.553	-0.0096
		0.20	-1.469	0.0712
	0	0.05	0.769	-0.0762
		0.10	0.787	0.0521
		0.15	0.811	0.0289
		0.20	0.810	-0.0301
	6	0.05	0.882	0.0260
		0.10	0.919	0.0332
		0.15	0.950	0.0061
		0.20	0.994	0.0074
0.6	-6	0.05	-1.387	0.0115
		0.10	-1.469	0.0250
		0.15	-1.479	0.1521
		0.20	-1.428	0.0629
	0	0.05	0.777	0.0127
		0.10	0.789	0.1015
		0.15	0.785	0.1291
		0.20	0.789	0.1686
0.6	6	0.05	0.851	0.0031
		0.10	0.892	0.0120
		0.15	0.929	0.0191
		0.20	0.956	0.0361
0.8	-6	0.05	-1.401	-0.0402
		0.10	-1.415	-0.0038
		0.15	-1.444	-0.0971
		0.20	-1.419	-0.0012
	0	0.05	0.797	0.0294
		0.10	0.809	0.0372
		0.15	0.802	0.0058
		0.20	0.793	-0.0638
	6	0.10	0.946	0.1282
		0.15	0.916	0.0990
		0.20	0.958	-0.0573
1.0	-10	0.05	-1.752	-0.0835
		0.10	-1.809	-0.0608
		0.15	-1.888	-0.0244
		0.20	-1.960	-0.0009
	0	0.05	0.822	0.0762
		0.10	0.827	0.1185
		0.15	0.809	0.1585
		0.20	0.824	0.1830
	6	0.05	1.235	0.0834
		0.10	1.224	0.0828
		0.15	1.029	0.0592
		0.20	1.015	0.1713
∞	-10	0.05	-1.500	-0.1056
		0.10	-1.642	-0.1223
		0.15	-1.733	-0.0730
		0.20	-1.665	0.0291
	0	0.05	0.877	0.0752
		0.10	0.859	0.1395
		0.15	0.831	0.1977
		0.20	0.809	0.2567
	10	0.05	1.500	-0.1056
		0.10	1.642	-0.1223
		0.15	1.733	-0.0730
		0.20	1.665	0.0291

Aerodynamic damping (Ξ) represents the net energy exchange over one cycle ($\Xi = -\oint C_\ell \cdot d\alpha$). A positive value ($\Xi > 0$) indicates a stable, clockwise hysteresis loop where the airfoil dissipates energy into the flow. A negative value ($\Xi < 0$) indicates a counter-clockwise loop where the airfoil extracts energy, potentially leading to aeroelastic instabilities.

E

Supplemental Results

This appendix provides additional pressure coefficient (C_p) data to supplement the discussion in chapter 6. These plots offer a more granular view of the surface pressure evolution across intermediate ground clearances.

E.1. Attached Flow

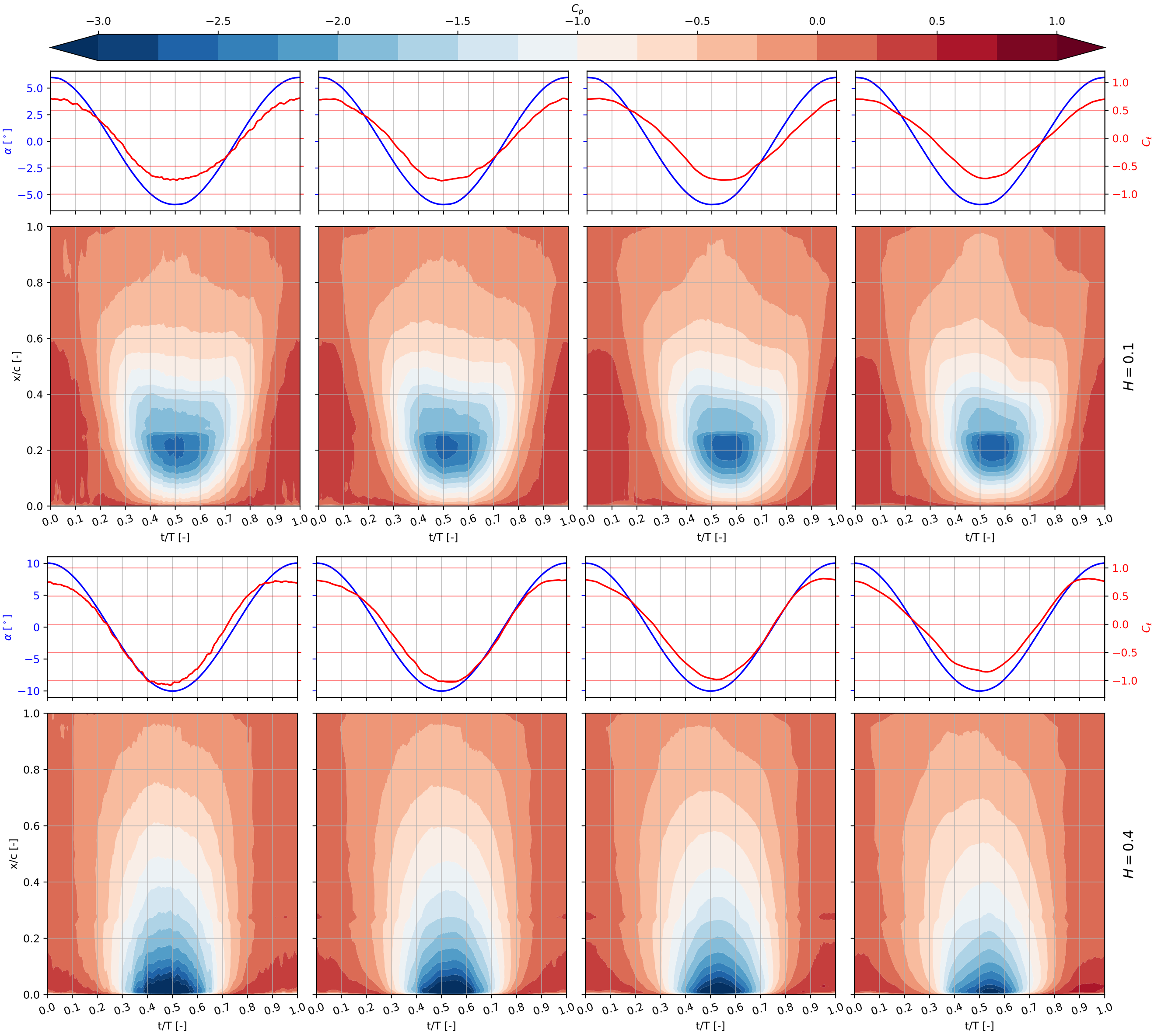

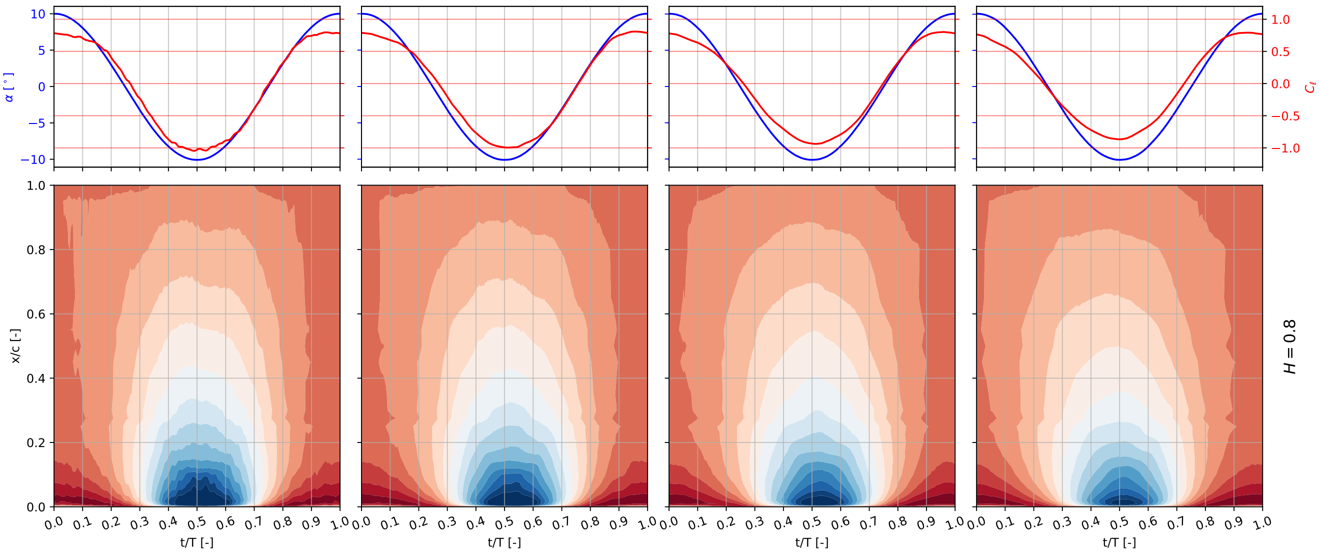

Figure E.1: α, C_ℓ, and C_P contour over x/c vs t/T map at various heights H and reduced frequency k (left to right): $[0.05, 0.10, 0.15, 0.20]$.

E.2. Negative Dynamic Stall

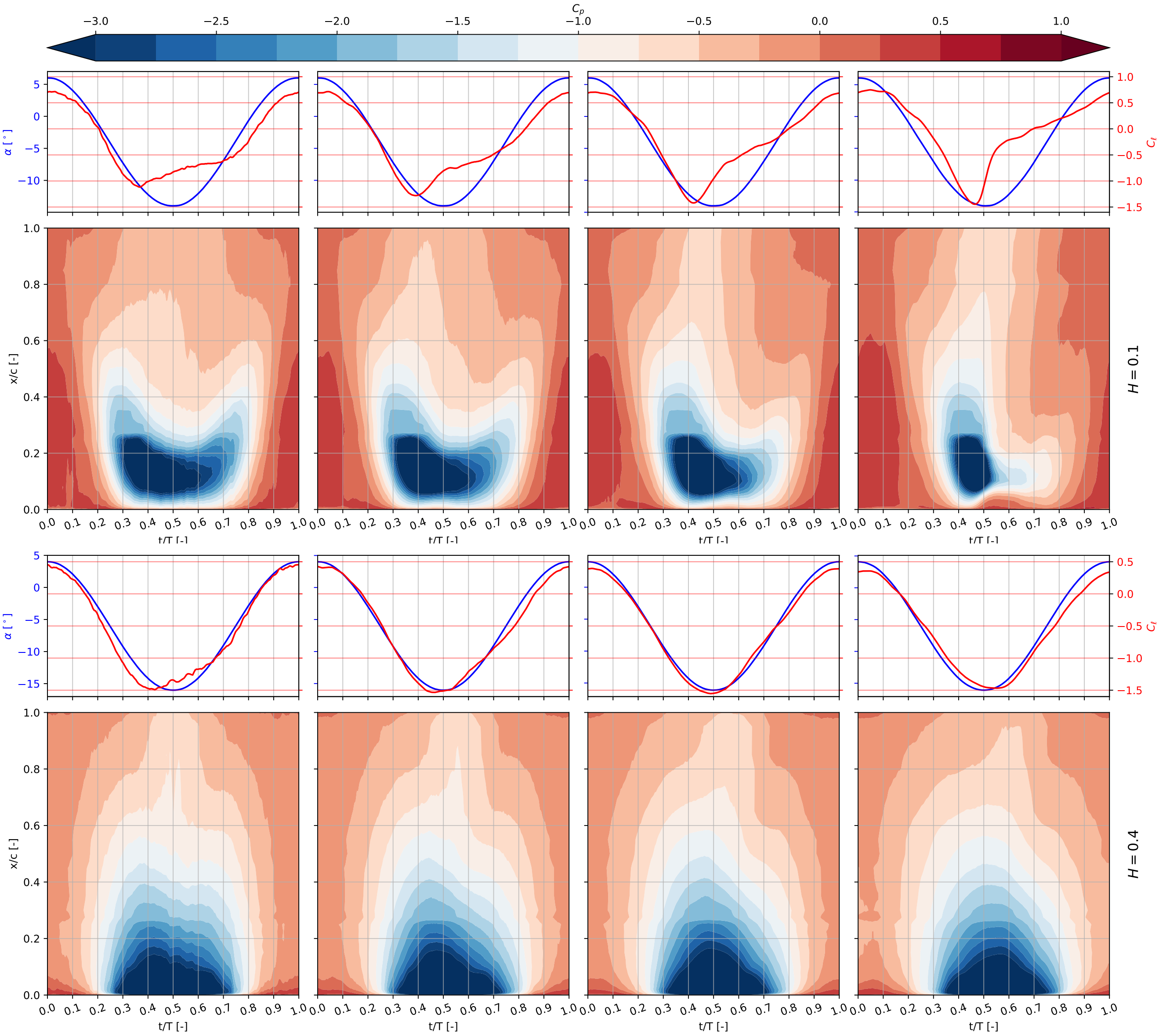

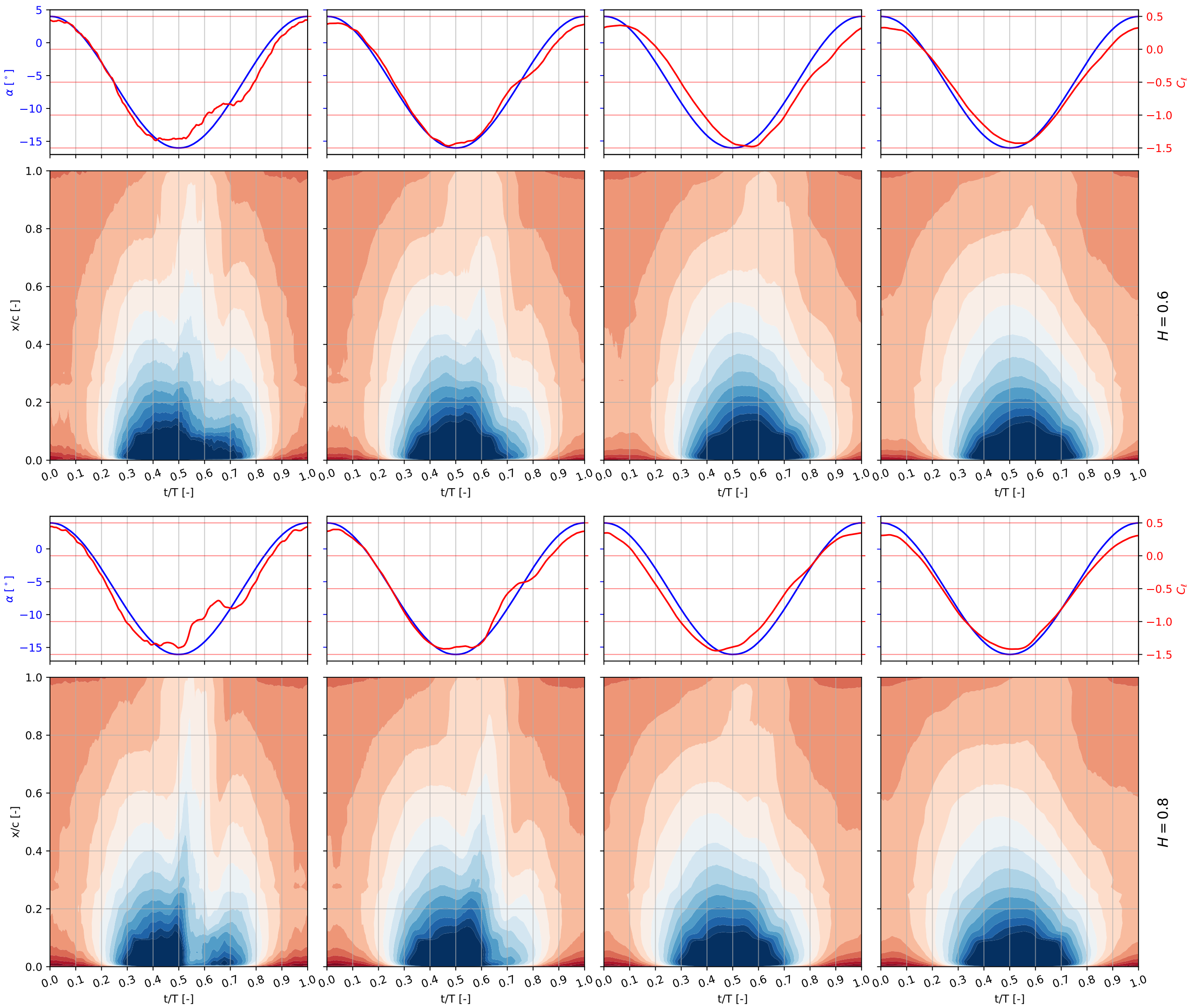

Figure E.2: α, C_ℓ, and C_P contour over x/c vs t/T map at various heights H and reduced frequency k (left to right): $[0.05, 0.10, 0.15, 0.20]$.

E.3. Positive Dynamic Stall

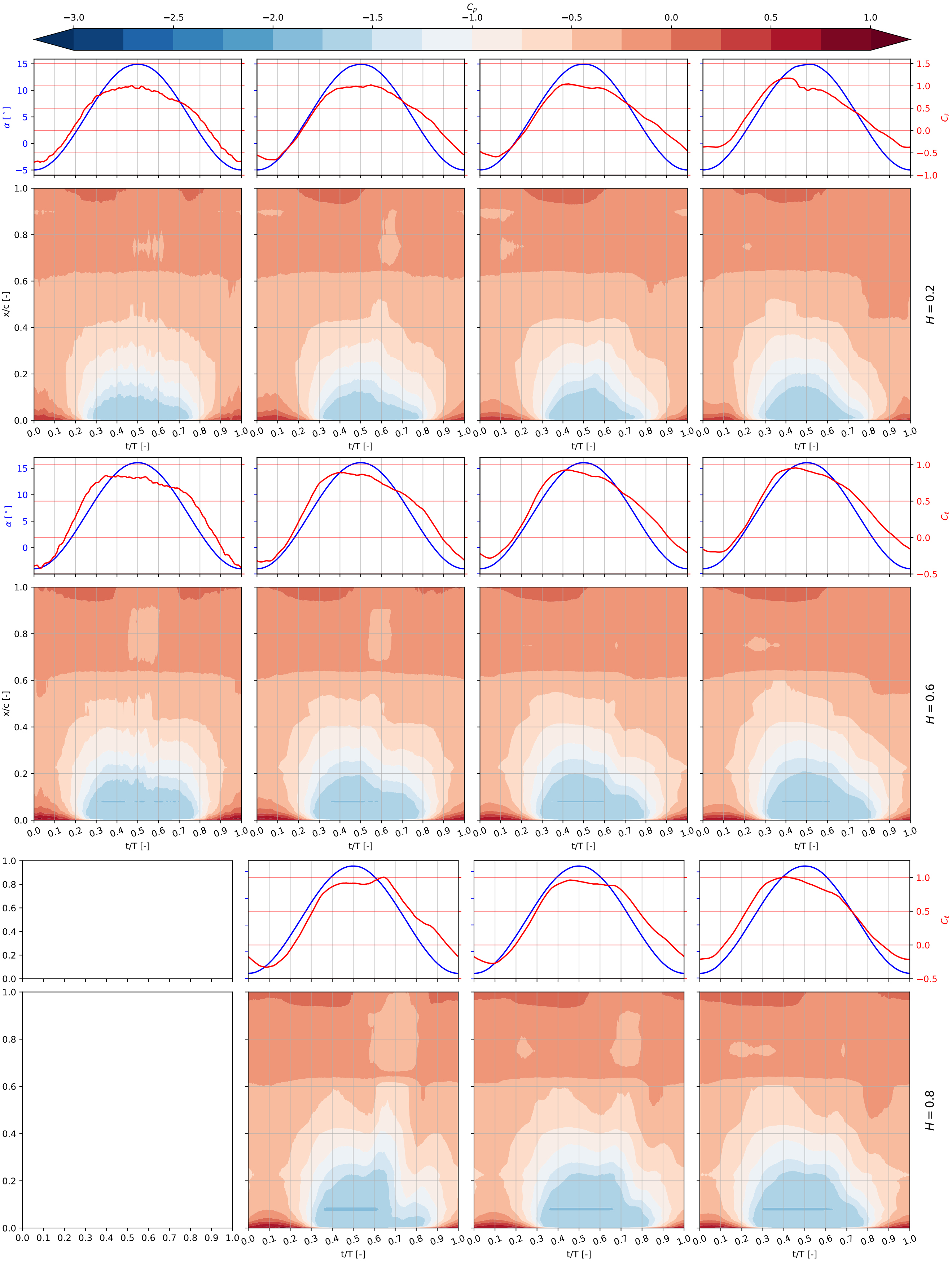

Figure E.3: α, C_ℓ, and C_P contour over x/c vs t/T map at various heights H and reduced frequency k (left to right): $[0.05, 0.10, 0.15, 0.20]$.